SOUNDING ROCKET RESEARCH

Forrest S. Mozer
Principal Investigator

Space Sciences Laboratory
University of California
Berkeley, California 94720

Space Sciences Laboratory Series 22, Issue 15

Final Report for research performed
during the period June 1, 1968 to February 28, 1981
under NASA grant NGR 05-003-239

Report prepared for:

NASA/Goddard Space Flight Center
Greenbelt, Maryland 20771

TECHNICAL REPORT STANDARD TITLE PAGE

1. Report No.	2. Government Accession No.	3. Recipient's Catalog No.

4. Title and Subtitle	5. Report Date
Sounding Rocket Research (Aries/Firewheel)	July, 1981 6. Performing Organization Code
7. Author(s) Forrest S. Mozer, Principal Investigator	8. Performing Organization Report No. Series 22, Issue 15
9. Performing Organization Name and Address Space Sciences Laboratory University of California Berkeley, California 94720	10. Work Unit No. 11. Contract or Grant No. NGR 05-003-239
12. Sponsoring Agency Name and Address NASA/Goddard Space Flight Center Greenbelt, Maryland 20771	13. Type of Report and Period Covered Final Report 6/1/68 - 7/28/81 14. Sponsoring Agency Code

15. Supplementary Notes

N/A

16. Abstract

Rocket experiments flown in seven programs during the past decade are summarized in terms of the scientific results achieved.

17. Key Words (Selected by Author(s))	18. Distribution Statement
Rocket experiments Aurora Spread-F	

19. Security Classif. (of this report)	20. Security Classif. (of this page)	21. No. of Pages	22. Price*
U	U	109	

*For sale by the Clearinghouse for Federal Scientific and Technical Information, Springfield, Virginia 22151.

TABLE OF CONTENTS

BIBLIOGRAPHY OF WORK RESULTING FROM RESEARCH SUPPORTED WHOLLY OR IN PART BY NGR 05-003-239

A. Publications

1. Application of electric field and fast Langmuir probes for the in situ observation of electrostatic waves and irregularities, M. C. Kelley, C. W. Carlson, and F. S. Mozer, in Effect of the Ionosphere on Space Systems and Communications, ed. J. M. Goodman, p. 453, Naval Research Lab, 1975.

2. Evidence that the electrostatic ion cyclotron instability is saturated by ion heating, M. C. Kelley, E. A. Bering and F. S. Mozer, Phys. Fluids, 18, 1590, 1975.

3. Observations of an intense field-aligned thermal ion flow and associated intense narrow band electric field oscillations, E. A. Bering, M. C. Kelley, and F. S. Mozer, J. Geophys. Res., 80, 4612, 1975.

4. Evidence for a Rayleigh-Taylor type instability and upwelling of depleted density regions during equatorial spread-F, M. C. Kelley, G. Haerendel, H. Kappler, A. Valenzuela, B. B. Balsley, David A. Carter, Warner L. Ecklund, B. Hausler, C. W. Carlson, and R. Torbert, Geophys. Res. Lett., 3, 448, 1976.

5. Impulsive ion injection into the polar cusp, R. B. Torbert and C. W. Carlson, in B. M. McCormac (ed.), Magnetospheric Particles and Fields, D. Riedel Publ. Co., Dordrecht Holland, p. 47, 1976.

6. Comparison of simultaneous magnetotail and polar ionosphere electric fields and energetic particles, J. E. McCoy, R. P. Lin, F. S. Mozer, R. E. McGuire, L. M. Chase and K. A. Anderson, J. Geophys. Res., 81, 2410, 1976.

7. Observations of intense velocity shear and associated electrostatic waves near an auroral arc, M. C. Kelley and C. W. Carlson, J. Geophys. Res., 82, 2343, 1977.

8. Observation and interpretation of particle and electric field measurements inside and adjacent to an active auroral arc, C. W. Carlson and M. C. Kelley, J. Geophys. Res., 82, 2349, 1977.

9. Relations between transverse electric fields and field-aligned currents, A. J. Mallinckrodt and C. W. Carlson, J. Geophys. Res., 83, 1978.

10. Evidence for parallel electric field particle acceleration in the dayside auroral oval, R. B. Torbert and C. W. Carlson, J. Geophys. Res., 85, 2009, 1980.

11. Solar wind ion injections in the morning auroral oval, C. W. Carlson and R. B. Torbert, J. Geophys. Res., 85, 2903, 1980.

12. Rocket-borne wave measurements in the dayside auroral oval, M. A. Temerin and M. C. Kelley, J. Geophys. Res., 85, 2915, 1980.

13. Observations of ULF electric field fluctuations in the dayside auroral oval, M. A. Temerin and B. K. Parady, J. Geophys. Res., 85, 2925, 1980.

14. Electric fields in the dayside auroral oval, T. S. Jorgensen, I. S. Mikkelsen, K. Lassen, G. Haerendel, E. Rieger, A. Valenzuela, F. S. Mozer, M. A. Temerin, B. Hojback, and L. Bjorn, J. Geophys. Res., 85, 2891, 1980.

15. Low distortion resistive anodes for two dimensional position-sensitive MCP systems, M. Lampton and C. W. Carlson, Rev. Sci. Instrum., 50 (9), 1979.

16. The effect of microscopic turbulence on magnetosphere-ionosphere coupling, R. Lysak and C. W. Carlson, Geophys. Res. Lett., 8, 269, 1981.

17. On the origin and spacial extent of high latitude F region irregularities, M. C. Kelley, J. F. Vickrey, C. W. Carlson and R. B. Torbert, J. Geophys. Res. (submitted 1981).

B. Talks Presented at Scientific Meetings

1. Three independent measurements of electric fields in an aurora, (Abstract), F. S. Mozer, C. W. Carlson, E. Bering, and M. C. Kelley, Trans. Am. Geophys. Union, 52, 329, 1971.

2. Measurements of auroral electric fields with a differential retarding potential analyzer, (Abstract), C. W. Carlson, Trans. Am. Geophys. Union, 52, 329, 1971.

3. In situ observations of the equatorial spread-F instability, (Abstract), M. C. Kelley and C. W. Carlson, Trans. Am. Geophys. Union, 55, 381, 1974.

4. Measurements of charged particles in equatorial spread-F, (Abstract), R. B. Torbert, C. W. Carlson, and B. Hausler, Trans. Am. Geophys. Union, 55, 381, 1974.

5. Observations of low and medium energy particles in the polar cusp, (Abstract), R. B. Torbert, K. A. Anderson, and C. W. Carlson, Trans. Am. Geophys. Union, 56, 430, 1975.

6. Production and distribution of F region irregularities, M. C. Kelley, C. W. Carlson, and F. S. Mozer, Trans. Am. Geophys. Union, 57, 297, 1976.

7. Ionospheric polarization and field-aligned currents, A. J. Mallinckrodt and C. W. Carlson, Trans. Am. Geophys. Union, 57, 992, 1976.

8. Impulsive plasma injection into the polar cusp, C. W. Carlson, B. Parady, M. Temerin, R. Torbert, and M. C. Kelley, presented at the Second Magnetospheric Cleft Symposium, St. Jovite, Quebec, October 1976.

9. Parallel electric fields in the dayside cusp, M. Temerin, C. W. Carlson, R. Torbert, F. S. Mozer, and G. Haerendel, presented at the Second Magnetospheric Cleft Symposium, St. Jovite, Quebec, October 1976.

10. Rocket-borne wave, particle and irregularity measurements in the polar cusp, M. C. Kelley, C. W. Carlson, and R. Torbert, presented at the Second Magnetospheric Cleft Symposium, St. Jovite, Quebec, October 1976.

11. Observations of beam-generated upper hybrid waves parametrically decaying to whistlers, C. W. Carlson, R. E. Ergun and M. K. Hudson, presented at Am Geophys. Union Meeting, December 1977.

12. Observations of auroral electron fluxes associated with high frequency plasma waves, A. J. Mallinckrodt and C. W. Carlson, presented at Am. Geophys. Union Meeting, December 1977.

13. Changes in auroral electron spectra associated with high frequency plasma wave emissions, A. J. Mallinckrodt, C. W. Carlson, and R. Ergun, Trans. Am. Geophys. Union, 59, 350, 1978.

14. Observations of strong electrostatic waves and parametric decay in the ionosphere, C. W. Carlson, presented at European Geophys. Society Meeting, Budapest, September 1979.

15. On the control of ionospheric electric fields by auroral electron fluxes, R. Ergun, A. J. Mallinckrodt, and C. W. Carlson, Trans. Am. Geophys. Union, 60, 351, 1979.

16. Observations of computer generated aurora, A. J. Mallinckrodt, presented at Am. Geophys. Union Meeting, May 1979.

17. Plasma density and electric field fluctuation measurements in the auroral electrojet, E. Kudeki, R. Pfaff, A. Pedersen and C. W. Carlson, Trans. Am. Geophys. Union, 61, 326, 1980.

18. Auroral wave excitations associated with an ion beam, E. Witt, M. McFadden, and C. W. Carlson, Trans. Am. Geophys. Union, 60, 913, 1979.

19. Auroral particle and electric field measurements in conjunction with active plasma experiments, R. I. Bush, A. J. Mallinckrodt, and C. W. Carlson, Trans. Am. Geophys. Union, 60, 913, 1979.

20. Effects of a xenon ion beam in the ionosphere, R. I. Bush, C. W. Carlson, and D. W. Curtis, Trans. Am. Geophys. Union, 61, 1082, 1980.

C. Ph.D. Theses

Auroral Zone Electric Field Measurements on Sounding Rockets, M. C. Kelley, Ph.D. Thesis, Phy .s Department, University of California, Berkeley. 1970.

Rocket Measurements of Auroral Zone Low Energy Charged Particles, C. W. Carlson, Ph.D. Thesis, Physics Department, University of California, Berkeley, 1974.

Auroral Zone Electric Current Measurements on Sounding Rockets, E. A. Bering, Ph.D. Thesis, Physics Department, University of California, Berkeley, 1974.

Quasi-static Electric Fields, Turbulence and VLF Waves in the Ionosphere and Magnetosphere, M. A. Temerin, Ph.D. Thesis, Physics Department, University of California, Berkeley, 1978.

Low-energy Plasma in the Dayside Auroral Zone, R. B. Torbert, Ph.D. Thesis, Physics Department, University of California, Berkeley, 1979.

Rocket Observations of Natural and Artificially Stimulated Phenomena within an Auroral Arc, A. J. Mallinckrodt, Ph.D. Thesis, Physics Department, University of California, Berkeley, 1980.

I. INTRODUCTION

This grant covered a period of more than twelve years and supported a wide variety of ionospheric particle and field research performed with sounding rockets. This research can be grouped into seven major rocket projects. Each project included the usual phases of experiment design and construction, flight operations, and data analysis. A discussion of the experimental details and scientific results of each project is given in section II.

Several important experimental techniques have been developed under support of this grant. The double-probe electric field technique was perfected during this series of experiments and the mechanical design of the electric field booms is now widely used by other experimenters as well. Other instrumentation developed under this grant includes swept frequency receivers, density fluctuation detectors, ion drift detectors and numerous charged particle detectors and mass spectrometers.

Most of the work done under this grant has been carried out by a succession of graduate students who used the results for Ph.D. theses. The students are M. C. Kelley, C. W. Carlson, E. A. Bering, R. B. Torbert, M. A. Temerin, and A. J. Mallinckrodt.

II. TASKS PERFORMED AND SCIENTIFIC RESULTS

A. Javelin NASA 8.55, 8.56 (Auroral Zone, 1970)

Two Javelin rockets were launched from Fort Churchill, Canada during the spring of 1970 to investigate the electric field and particle precipitation structure of discrete auroral arcs. The instrumentation of these payloads included double probe E-field detectors, an ion drift detector, energetic electron and ion electrostatic analyzers, a split Langmuir current probe and several photometers. Of these instruments, the double probe, the ion drift detector and the split Langmuir probe provided three independent measures of

electric fields. The results verified that these measuring techniques, which were somewhat unproven at the time, gave consistent results (Mozer et al., 1971T). (Note: References with "T" are listed in "Talks Presented at Scientific Meeting...") The operation and results of the ion drift detector are given by Carlson (1971T) and Carlson and Kelley (1977). The scientific results of these flights are discussed by Kelley et al. (1975), Bering et al. (1975), Kelley and Carlson (1977), and Carlson and Kelley (1977); and in the Ph.D. thesis of C. W. Carlson entitled "Rocket measurements of auroral zone low energy charged particles" (University of California, 1974). Results from these flights also motivated the study of electric field and field aligned currents discussed by Mallinckrodt and Carlson (1978).

B. Black Brandt III, NASA 2201, 2202 (Polar Cap, 1971)

Two Black Brandt III rockets were flown from Resolute Bay N.W.T. in 1971 to investigate the mapping of electric fields and charged particles from the earth's deep magnetotail down to the polar cap ionosphere. These experiments were made in conjunction with the lunar orbiting UC subsatellite released from Apollo 15. Results from this experiment are presented by McCoy et al. (1976).

C. Dual Hawk (Equatorial Spread F, 1972)

The Dual Hawk rocket project was a collaboration between UC Berkeley and the Max-Planck-Institut für Extraterrestrische Physik in Garching, West Germany. The objective of this experiment was to trace the development of equatorial Spread F using a combination of optical observations of barium releases and in-situ measurements of plasma density and electric fields. Our role in the experiment was to provide the in-situ instrumentation package. These flights were unsuccessful owing to launch vehicle failures.

D. Javelin NASA 8.62, 8.63 (Equatorial Spread F, 1973)

Two Javelin rockets were launched from Natal, Brazil in 1973 to investigate the origin and evolution of equatorial Spread F. These flights were made

in collaboration with the Max-Planck-Institut and included barium releases in addition to the in-situ measurements. Improved fast Langmuir probes suited to measure electrostatic waves and irregularities were developed for this experiment (Kelley et al., 1975). The scientific results of these flights were evidence for a Rayleigh-Taylor instability during Spread F and the first direct evidence for plasma "bubbles" or buoyant low-density regions appearing during Spread F conditions (Kelley et al., 1976).

E. Polar Cusp Black Brandt IV (Greenland, 1974-75)

The Greenland polar cusp campaign was a collaboration between UC Berkeley, the Max-Planck-Institut für Exterrestrische Physik and the Danish Meteorological Institut. We supplied instrumentation for two rocket payloads which included E-field double probes, a plasma density experiment and an array of ion and electron detectors. The payloads also contained shaped-charge barium experiments supplied by the Max Planck-Institut. The main objectives of this experiment were to investigate the plasma flow pattern near the cusp, study solar wind plasma entry into the cusp, and search for magnetic field aligned electric fields and particle acceleration.

Both flights were very successful in fulfilling these goals. The flights took place inside the dayside auroral region lying just equatorward of the convection reversal boundary (Jorgensen et al., 1980). Although this region is nominally on closed magnetic shells, we found unambiguous evidence of solar wind plasma injected onto these field lines. These injections consist of brief bursts lasting a few seconds and separated by periods of about 100 seconds. This property of the injection allowed us to use time of flight analysis to ascertain the ion mass composition and verify that the injections were of solar wind composition (Torbert and Carlson, 1976; Carlson and Torbert, 1980). These flights also provided evidence for magnetic field aligned acceleration of particles. This evidence came from the barium shaped charge and from the

low energy electron detectors (Torbert and Carlson, 1980). Interesting new measurements of low frequency waves were also obtained (Temerin and Kelley, 1980; Temerin and Parady, 1980).

These flights were thesis projects for two graduate students, M. A. Temerin and R. B. Torbert.

F. Project Porcupine (Auroral Zone, 1977, 1979)

Project Porcupine included four rocket flights over a period of four years. It was organized and managed by the Max-Planck-Institut and included several other European groups in addition to the U.S. collaboration from UC Berkeley. The payloads consisted of a main "mother" payload which included extensive particle and field instrumentation and four ejected subpayloads. For each payload, we supplied two subpayloads which contained E-field probes, Langmuir probes, a magnetometer, and a complement of particle detectors. The other two cannisters contained a barium shaped charge and a xenon plasma gun. These subpayloads were ejected from the main payload during flight and allowed three-point measurements with separation distances up to four kilometers. The launch vehicles were "Aries" rockets. The first launch had a vehicle failure, but the remaining three flights were successful and have returned valuable data.

Preliminary results from these flights have been presented in several scientific meetings (Carlson et al., 1977T; Mallinckrodt and Carlson, 1977T; Mallinckrodt et al., 1978T; Carlson, 1979T; Ergun et al., 1979T; Mallinckrodt, 1979T; Kudeki et al., 1980T; Witt et al., 1979T; Bush et al., 1979T; and Bush et al., 1980T). One of the unique observations on these flights was strong emission of Bernstein waves near the upper hybrid frequency. These waves reached amplitudes of tens of mV/m. In one case the wave amplitude was sufficient to produce parametric decay into other lower frequency modes. The barium release also produced unexpected effects upon the wave propagation, causing trapping of waves inside the enhanced plasma of the barium cloud. The

other unique opportunity afforded by these flights was to study effects of the xenon plasma gun. This analysis is still under way and preliminary results were presented by Bush et al. (1980T). First results of these flights are enclosed in the Appendix and the first three publications are in preparation. One Ph.D. thesis, by A. J. Mallinckrodt, was based upon these experiments, and a second, by R. Bush, is in progress.

G. Project Firewheel (Active Magnetospheric Satellite, 1980)

Project Firewheel was an attempt to inject an artificial plasma cloud into the tenuous magnetotail plasma and study its effects such as magnetic cavity formation, magnetic diffusion, momentum exchange, etc. These objectives are discussed in great detail in the experiment proposal.

The UC participation in Firewheel was to supply a completely instrumented subsatellite to be ejected in orbit and perform in-situ measurements of the natural and artificially produced plasmas. The spacecraft was launched on the second Ariane test vehicle, which unfortunately experienced a first stage motor failure.

APPENDIX

ROCKET OBSERVATIONS OF NATURAL AND ARTIFICIALLY STIMULATED PHENOMENA WITHIN A QUIET AURORAL ARC

Albert John Mallinckrodt III

ABSTRACT

An Aries sounding rocket launched from Kiruna, Sweden measured particle fluxes, DC and AC electric fields, and plasma density within and on the equatorward side of a quiet auroral arc. A striking anticorrelation between the cross-arc component of the electric field and the energy of the secondary peak in the electron differential particle flux was observed. A numerical procedure has been developed to simulate auroral electrodynamics and shows the observed anticorrelation to be consistent with a model in which field-aligned sheet currents are negligible with respect to ionospheric height integrated currents. The electric field is then determined from the divergenceless flow of the ionospheric current system and the transverse conductivities which are in turn controlled by the precipitating electrons. In addition large amplitude high frequency plasma waves were observed within a plasma density enhancement artificially created by a barium shaped charge experiment included on the payload. The waves are associated with the formation of a plateau in the formerly peaked auroral electron distribution function. These observations are explained in terms of the refractive trapping of wave packets within the artificial density enhancement. The resulting prolonged interaction of these waves with the auroral electrons allows the growth of the waves at the expense of the free energy in the electron distribution function.

Table of Contents

I. INTRODUCTION

During the past two decades the space research effort has revealed the large-scale structure of that portion of space which is controlled by the earth's magnetic field - the *magnetosphere*. Prior to the first data returned to earth from artificial satellites, the region of space surrounding the earth was generally envisioned as a listless, cold, and extremely tenuous medium. The discovery of the radiation belts (Van Allen *et al.*, 1958) provided dramatic evidence to the contrary and resulted in an awakened scientific interest in near-earth space phenomena. With the discovery of the *solar wind*, a continuous stream of plasma flowing from the sun, an energy source for the observed high energy particles was found and it was realized that the description of magnetospheric processes involved the interaction of a fully ionized solar wind plasma with the magnetic field of the earth.

Until the early 1970's the bulk of experimental work was directed toward gathering a body of data from which a comprehensive empirical model of the earth's magnetosphere could be established. While there is still some disagreement regarding the interpretation of the data, a reasonable version of the current magnetospheric model is displayed in Figure I.1. The magnetic field of the earth is confined to a comet-like region of space about 40 R_e in diameter and perhaps 1000 R_e in length. The blunt *nose* of the magnetosphere is formed by the dynamic pressure of the solar wind which compresses the magnetic field on the day side of the earth and confines its flanks further downstream. At the furthest downstream points the magnetosphere presumably becomes virtually indistinguishable from the interplanetary medium. To date only a few encounters with the tail have occurred beyond lunar distances. The boundary of the earth's magnetosphere is called the *magnetopause* and is characterized by the transition from a

region of large plasma pressure outside the magnetosphere to a region of large magnetic field strength inside. The discontinuity in the magnetic field requires large sheet currents to flow on the magnetopause.

In discussing the magnetosphere it is helpful to define three distinctly different types of magnetic field lines. *Closed* magnetic field lines are those which pass only through the earth. *Open* magnetic field lines are those which pass both through the earth and the sun. Finally, *interplanetary* field lines are those which do not pass through the earth. The magnetosphere proper consists of closed field lines and the near earth portions of open field lines. Just outside the magnetosphere lies a region called the *magnetosheath*. The magnetosheath consists of solar wind plasma on interplanetary field lines, but which differs from the undisturbed solar wind by virtue of its having passed through the *bow shock*, the shock wave formed by the pile up of solar wind plasma at the nose of the magnetosphere. In this region the plasma is hotter and more dense and the flow is more disordered than in the solar wind particularly at the sub-solar stagnation point on the magnetopause. As we continue tailward the distinction becomes less clear.

Satellites instrumented with particle and field detectors have mapped out the various regions within the magnetosphere and delineated the borders of these regions. Due to the adiabatic motion of the plasma these boundaries can often be defined in terms of the magnetic latitude of the field lines which are coincident with them. In all of the following discussion it is helpful to keep in mind that whenever the component of the electric field parallel to the magnetic field vanishes the frozen-in condition applies. That is, one may think of the field and the plasma moving as a single entity. Due to the collisionless nature of the plasma throughout most of the magnetosphere, the conductivity along magnetic field lines is very high and as a result the frozen-in condition applies. In certain regions however, wave turbulence may result in an *anomalous resistivity* which can produce magnetic field-aligned electric fields and invalidate the frozen-in condition.

At the lowest latitudes and thus close to the earth, the magnetic field lines lie close to their expected dipolar configuration. This region is called the *plasmasphere*. The plasma here tends to be stably trapped for long periods and diffusion of ionospheric plasma along magnetic field lines fills the plasmasphere to high densities. The phenomenon of shell-splitting due to the longitudinally asymmetric distortion of the magnetic field lines complicates this picture and results in the formation of a *quasi-trapped* region in which certain particles, depending on their magnetic latitude and mirror altitude are not able to complete an entire orbit around the earth (Stone, 1963; Anderson *et al.*, 1965; Roederer, 1967; Roederer, 1970). The plasma here corotates with the earth due to the presence of an electric field generated in the ionosphere by the viscous coupling of the ionospheric plasma to the neutral atmosphere. Due to the high conductivity for currents along magnetic field lines, the field lines may be considered equipotentials. Thus the ionospheric electric field is mapped out into the magnetosphere. Were it not for the presence of the solar wind or other outside influences the plasmasphere would extend to arbitrary distances and the only limit on its corotation would be the limited angular momentum of the earth available to be imparted to the plasma. The solar wind however imposes its own, quite different requirements on the motion of the plasma at the boundaries of the magnetosphere and it is this competition which results in the formation of the other regions of the magnetosphere.

At a magnetic latitude of about 65 degrees the corotation stops (Mozer *et al.*, 1980). This *corotation boundary* separates the plasmasphere from the *plasma sheet*. In the plasma sheet the field lines are still closed but highly distorted on the night side into a long tail with field lines running sunward to the north of and anti-sunward to the south of a *neutral sheet* dividing the *magnetotail* into two regions of oppositely directed magnetic field. A *neutral sheet current* flows from dawn to dusk in the neutral sheet as can be seen from the tangential discontinuity in the magnetic field at this boundary. At the inner edge of the neutral sheet the *ring current*, an occasionally intense current, flows. Convection in the plasma sheet is predominantly sunward

owing to the process of magnetic field line reconnection which depletes the magnetic flux on the day side and builds it up on the night side. This sunward convection continues around the dawn and dusk sides of the plasmasphere to the nose of the magnetosphere where it reconnects with the interplanetary field. The competition between the sunward and anti-sunward flow at the corotation boundary on the dusk side yields a simple determination of the corotation boundary position through satellite electric field measurements. On the dawn side the distinction is not so clear since the flows are in the same direction.

The plasma sheet field lines reconnect to interplanetary field lines at the nose in the *entry layer*. On the day side a magnetic *cusp* is formed which allows direct penetration of solar wind plasma to the ionosphere. Further tailward the solar wind plasma, having mirrored in the cusp, is swept back on these now open field lines forming the *plasma mantle* just within the polar magnetopause. Due to the combined effects of equatorward convection and velocity dispersion of the tailward flowing mantle plasma, the equatorward portions of the mantle consist of the lowest energy particles (Paschman, 1979). The field lines convect into the *polar lobes* of the magnetosphere where the primary source of plasma is the *polar wind* due to diffusion of plasma from the polar ionosphere. On a given field line the boundary between the plasma mantle and the polar lobe is indistinct but it will likely progress tailward as we consider field lines lying closer to the equatorial plane.

Along the flanks of the magnetosphere lies the *boundary layer*. In this region solar wind plasma is injected inside the magnetopause and diffuses onto closed field lines creating a viscous transfer of momentum and energy to the magnetosphere and causing anti-sunward convection (Lemaire, 1977; Lemaire and Roth, 1978). On the inside edge of the boundary layer, a similar viscous interaction with the plasma sheet plasma causes a sunward convection closing the circulation pattern.

The picture described in the preceding paragraphs applies to highly idealized, steady-state conditions. Since the primary energy source driving magnetospheric phenomena is the solar

wind, the validity of the model depends predominantly on its parameters. The orientation of the interplanetary magnetic field, the solar wind plasma density, temperature, and bulk flow speed, and the temporal variability and history of all these affect the state of the magnetosphere.

Before the advent of electric field experiments capable of operating in the tenuous plasma environment of the outer magnetosphere, researchers relied on plasma density measurements to define the boundary of the plasmasphere the *plasmapause*. The plasma density in the plasma sheet is reduced by about two orders of magnitude from that within the plasmasphere due to the loss of plasma through reconnection at the nose and the much larger volume of space occupied by plasma sheet field lines. In periods of long solar wind stability this method yields satisfactory results, but during an increase in the dynamic pressure of the solar wind, the magnetosphere is compressed on the day side and the corotation boundary is driven to lower magnetic latitudes. Plasma at the outer boundaries of the plasmasphere, built up by long periods of undisturbed diffusion of ionospheric plasma, is lost. When the corotation boundary moves outward, the field lines refill with ionospheric plasma on a time scale of days. During periods of high variability the plasma density at latitudes near the corotation boundary is a complicated function of the actual position of the corotation boundary over the last few days because of the long time scale for the ionospheric diffusion.

Another effect of quite some importance is the orientation of the interplanetary magnetic field. Depending on this orientation, magnetic field reconnection at the nose and thus plasma sheet convection may be enhanced or inhibited.

Rapid changes in any of the solar wind parameters induce changes in the state of the magnetosphere and often result in the triggering of a *magnetospheric substorm*. The substorm is characterized by the energization of plasma sheet particles at the expense of the stored magnetic energy of the magnetotail. The high latitude portion of the plasma sheet includes the *auroral zone*, those field lines on which electrons are energized and driven into the ionosphere creating

the most dramatic visual manifestation of the solar wind-magnetosphere interaction - the aurora.

The subject of this thesis is confined to those processes occurring on auroral field lines and, more specifically, to observations of natural and artificial phenomena occurring within the ionosphere in the presence of auroral electron precipitation. For many years prior to the advent of artificial satellites, instrumented balloons had monitored high altitude phenomena in the auroral zone. The difficulty with the interpretation of these data was that the measurements at balloon altitudes represented averages of the ionospheric phenomena over large distances. For example electric field measurements at balloon altitudes may be considered to represent an average of the E-region field over a distance of about 100 km. The visual thickness of auroral forms is on the order of kilometers (Maggs and Davis, 1968) and thus much of the expected fine structure is lost. Furthermore the actual particles producing the displays and their energies could only be guessed at from spectroscopic observations of auroral emissions and models of the high altitude atmosphere. In addition, with only the data from ground based magnetometers to work with, the three dimensional current system associated with auroral displays was not well defined.

Satellites have yielded valuable information on large scale structure of the auroral zone and the distribution of field-aligned currents, but due to their high velocity they give essentially no information on the fine structure or temporal variations in auroral displays.

The sounding rocket is uniquely suited to the needs of auroral investigations due to several factors. They can be launched on short notice into auroral conditions of the scientist's choice. They permit relatively long, continuous monitoring of the conditions within a single auroral arc. They have very low costs both in terms of manpower and money compared to satellites.

The data on which this research is based are from the second flight of the Aries-Porcupine

campaigns and, more specifically, from an ejectable sub-payload designed and built as a portion of this thesis research at the U.C. Space Science Laboratory. Two very interesting results were obtained from these data.

First, a very strict anticorrelation between the D.C. electric field and the peak energy of the precipitating electrons was observed. This observation will be discussed in terms of the influence that the energetic electrons exert on the ionospheric conductivity due to the ionization they produce. A numerical simulation of the ionospheric electrodynamics was developed and the results of its application to these data will be presented.

Second, high amplitude plasma waves were observed for a period following apogee during which the payload was enveloped by an artificial plasma density enhancement produced by a barium shaped charge experiment. At the same time a dramatic change in the distribution function of the auroral electron beam was noticed. The distribution, which displayed a prominent peak at an energy of 2-3 keV prior to the barium release and the observation of the waves, was modified to a plateau type distribution afterwards. These observations will be discussed in terms of the trapping of upper hybrid wave packets by the artificial plasma cloud. These trapped wave packets, due to their prolonged interaction with the auroral beam, attain substantially increased growth. As a result they grow to large magnitude and the increased interaction with the auroral electrons depletes the free energy represented by the peak in the distribution function. In addition a parametric decay process appears to have been driven by the high amplitude upper hybrid pump. Possible decay modes and wave vector matching schemes for this process will be discussed.

In all, four Aries-Porcupine payloads were built and launched. The first, launched in March 1976, yielded no scientific data as a result of the failure of the launch vehicle. The second was successfully launched one year later. The final two were launched two years later in March 1979 and will be the subject of other reports.

II. INSTRUMENTATION

The Aries-Porcupine project was an international collaboration involving researchers from several European countries, the U.S., and the Soviet Union. The use of the Aries rocket with its very large payload capacity permitted the construction of one of the most comprehensive instrument packages ever launched on an auroral sounding rocket mission. The main payload included the following experiments:

1 Double probe electric field

   a D.C. channel $\leq$ 80 Hz

   b A.C. channel 50 Hz - 20 kHz

2 Plasma density fluctuations

3 Low energy electrons

4 R.F. probes

   a High frequency .8 - 14.5 MHz for electron density and temperature measurements

   b Middle frequency .1 - 1.5 MHz for field aligned electron current measurements

5 Three-axis fluxgate magnetometer (resolution $\approx$ 1 nT)

6 Search coil magnetometer for magnetic fluctuations 10 Hz - 500 Hz

7 Suprathermal electrons 100 eV - 25 keV

8 Suprathermal protons 1 - 25 keV

9 Energetic particles

a Electrons 15 - 200 keV

b Ions 25 keV - 2 MeV

In addition, four free-flying sub-payloads were included on each flight. These were released early in the flight and were used both for active plasma experiments and as independent and spatially separate probes of local plasma conditions. On the four Porcupine payloads flown during the campaigns, various configurations of these sub-payloads were included. The second flight, which is the subject of this research, was equipped with a barium shaped charge experiment, a cesium ion gun experiment, and two ejectable multiply instrumented probes.

The barium shaped charge experiment created a large artificial plasma cloud near apogee due to the photo-ionization of barium atoms vaporized in the detonation of a mixture of barium and high explosive. Optical transitions in the ionized and neutral components of the barium allow observation of the clouds from the ground and their motions can yield important information about neutral winds and electric fields both transverse and parallel to the ambient magnetic field. In addition the auroral plasma perturbation can artificially stimulate plasma processes in the ionosphere which may then be monitored by the instruments of the main payload and the ejectable probes. Since the barium cloud must be illuminated by the sun and the observation stations must be in moonless dark, the inclusion of a barium shaped charge experiment limits the launch window to a few hours after sunset or before sunrise a couple of weeks a month.

The cesium ion gun was designed to yield an intense current of low energy cesium ions. Once again the effects of this major perturbation on the auroral plasma was to be monitored by the instrumented payloads. Due to the apparent malfunction of this device it will receive no further discussion.

The instrumentation aboard the ejectable probes was designed and built at the University

of California Space Sciences Laboratory. This instrumentation provided a comprehensive set of plasma diagnostics. The experiments may be roughly classified as particle, electric field, plasma, or magnetic field. Table I lists the experiments along with their ranges of operation, sensitivities, and sample times. Figure II.1 is a sketch of an ejectable probe along with detector aspects and payload coordinates.

II.A. Particle experiments

The payload was equipped with two different types of particle experiments which measured low energy electrons and high energy electrons and ions.

Low energy electrons

Retarding potential analyzers (RPA's) were used to monitor electron fluxes at energies from 6 eV to 500 eV. A diagram of this instrument is shown in Figure II.2a. A detailed description of this detector is to be found elsewhere (Carlson, 1974). Briefly the instrument uses a repelling grid held at +12 volts relative to the payload potential to eliminate the large thermal ion fluxes. Then a swept potential barrier is used to deny entrance to all electrons below a certain energy. Electrostatic focussing then allows only electrons of minimal excess energy (about 30 eV) access to the mouth of a channel electron multiplier (CEM). The CEM generates a large charge pulse ($\approx 10^9$ electrons/incident electron) which is amplified and shaped by a charge sensitive amplifier and one-shot circuit. The pulses are routed to the payload counter-board where they are accumulated and periodically read out by the payload telemetry.

Only electron RPA's were used on this flight. Practical considerations, relating mostly to the high voltage supply limitations, dictated the choice of either electron or ion RPA's but not both. Low energy ion measurements are effective in determining plasma flow velocities due to the relatively low ratio of ion thermal speed to typical flow velocities. This amounts to an

independent measurement of the electric field which is related to the drift velocity by $v_p = \frac{E \times B}{B^2} c$ in the essentially collisionless plasma above 110 km. Such double measurements have been used to establish the credibility of double probe measurements (Carlson, 1974). Since the cannister included a pair of double probes, no further flow velocity measurements were required. It was decided that an extension of the electron measurements to lower energies would be preferable.

Three RPA's were included with aspects centered at 0°, 30°, and 180° from the payload spin axis. The geometric factor of each RPA was 5.7×10^{-3} cm^2 ster eV with a conical angular acceptance of half-angle 3° and an energy resolution of about 30 eV. They complete one scan of the electron spectrum from 6 eV to 500 eV in 128 steps each 1.024 seconds. The counts were collected and telemetered once every .004 seconds.

High energy electrons and ions

Hemispherical plate electrostatic analyzers (ESA's) were employed to monitor electron fluxes from 350 eV to 30 keV and ion fluxes from 470 eV to 40 keV. These detectors find wide application in rocket and satellite instrumentation today and no detailed description will be given here. For more information see Chase (1969). Briefly, the ESA consists of two concentric hemispherical conducting plates held at different potentials. Only particles of the proper charge sign and an energy per unit charge in the proper range are allowed to pass between the plates to the exit where they are detected by a CEM.

The geometric factor of a small aperture ($\frac{\Delta r}{r} \leq .2$) hemispherical plate ESA as shown in Figure II.2b may be estimated with fair accuracy from the formula,

$$g(E) = \left(\frac{\Delta r}{r}\right)^2 A \sin\phi_{max} E \qquad \text{(II.1)}$$

where A is the collecting area of the CEM placed at the exit, ϕ_{max} is the collimator acceptance

half angle, and E is the center acceptance energy. Note that the geometric factor increases linearly with the energy of the particles being analyzed. The angular acceptance in the other direction is assumed to be determined by the analyzer plates and is approximately $2\frac{\Delta r}{r}$ at the extremes yielding a weighted average, for geometric factor purposes, of about $\frac{\Delta r}{r}$. The relative energy resolution of the instrument is essentially constant at all energies and is $\frac{\Delta r}{r}$ at the extremes or about half that as a weighted average.

Both ESA's had aspects of 0° with respect to the payload spin axis. The geometric factors of the electron and ion ESA's were 1.8×10^{-3} cm^2 ster (E) and 1.1×10^{-3} cm^2 ster (E) respectively. Both ESA's complete one scan over their respective energy ranges in 128 steps each 1.024 seconds. The counts are collected and telemetered each .004 seconds.

Ion composition experiment

Also included among the instrumentation was an experiment designed to yield information on the composition of the energetic ion fluxes in the auroral plasma. Such composition data can yield valuable information regarding magnetospheric acceleration and storage mechanisms. For instance, multiply charged ions would be expected to have their origins in the solar wind with little or no storage time in the magnetosphere while singly charged ions might be ionospheric or magnetospheric in origin.

The details of the instrument are to be found in Lin (1974). A similar instrument has been flown by Lynch *et al.* (1976) and detected H^+, O^+, and He^{++} ions in post-auroral breakup conditions. The experiment consists of a solid-state surface barrier detector sampling ions which have been previously sorted by a hemispherical ESA. In this case the same ESA used for the energetic ion measurements was used for the ion composition experiment.

It is a well known property of solid-state detectors that the charge pulse created by the

penetration of ions with relatively low energies is a strong function not only of the ion energy but the ion mass as well. Heavy ions create relatively smaller pulses than lighter ions of the same energy (Potter and Campbell, 1978; Campbell and Lin, 1973). This so called "pulse height defect" may be employed in combination with the known E/q of the ions passing through the ESA to yield both the charge state and mass of the ion.

The experiment is complicated by the inherent noise properties of surface barrier detectors, especially when used to detect ions in the under 10 keV range. The intrinsic noise of such detectors is usually on the order of the signal resulting from penetration by a 10 keV ion. There are two methods of dealing with this problem. The ions may be electrostatically preaccelerated to raise their energy above the noise level or the noise level itself may be lowered by cooling the detector. Both of these techniques were employed in the design of this experiment. The detector was lowered to a potential 5 kV below that of the exit aperture of the ESA thus adding an additional 5 keV per charge to each ion. In addition an evaporative cooling device was employed to cool the detector to a temperature of about $-50\,^{\circ}\mathrm{C}$. This device was filled with liquid freon and vented shortly before cannister ejection.

To minimize the likelihood of penetrating radiation producing spurious counts, an anticorrelation detector was placed behind the main detector. The outputs of both detectors were routed to charge sensitive amplifiers and then to an anticoincidence circuit.

A threshhold discriminator was used to eliminate response to detector noise. Those pulses which were ruled invalid by the anticoincidence circuit were counted and telemetered 250 times per second. The remaining pulses were delivered to a 12 bit (4096 bin) pulse height analyzer. The PHA processed and telemetered 2000 events per second. Only the first event in the period following a readout was processed for the next readout. In addition the number of valid and above threshhold counts were telemetered 250 times per second.

II.B. Electric field experiments

Three pairs of probes mounted on self-extending booms were included on the cannister to monitor DC and AC electric fields, plasma density, and temperature.

DC electric field

Two pairs of the probes were designed to measure the three-dimensional electric field. Referring to Figure II.1 the axial booms (5 and 6) constantly monitor the component of the electric field parallel to the payload spin axis while one pair of the radial booms (1 and 2) is able to measure the two components perpendicular to this axis due to payload rotation. The potential difference between the pairs of probes was monitored and included in the telemetry stream.

The radial booms were deployed by a centrifugally assisted feed of wire from an internal drum. The fully deployed length was 3.3 m tip-to-tip, but the rotation of the drum was monitored by the telemetry and less than full deployment could be accounted for. The axial probes deployed purely under the action of the spring loaded boom on which they were mounted, their fully deployed length was 2.0 m tip-to-tip.

AC electric field

In addition to the DC data, the signal from the electric field probes was used to generate three modes of AC field measurements. In the first mode the signal was processed by a bandpass filter to roll off frequencies less than 3 hz for the radial booms and .5 hz for the axial booms and frequencies greater than 128 hz for both pairs. By eliminating the large variations at the payload spin frequency, especially in the radial probes, the output signal could be greatly amplified. This waveform was then monitored with high time resolution (1000 samples per second) yielding high sensitivity to low frequency electric field fluctuations.

In the other two modes the signal was passed to a circuit consisting of a swept voltage controlled oscillator, mixer, and crystal filter forming a swept narrow bandpass filter. The log of the power in the passband was converted to a DC voltage and added to the data stream. Two such spectrum analyzers were included on the payload. The first swept from 0 to 50 khz in 512 steps with a bandpass of 300 hz completing one sweep every 2.048 seconds. The second swept from 0 to 5 Mhz in 512 steps with a bandpass of 30 khz completing one sweep every .512 seconds.

II.C. Plasma experiments

Two of the radial booms (3 and 4) similar to those used for the electric field experiments were employed as Langmuir probes to monitor plasma temperature and density. For a detailed discussion of Langmuir probe operation see Lochte-Holtgreven (1968). Briefly the current-voltage characteristics of the probe when immersed in a plasma are determined primarily by the electron density and energy distribution. By controlling and varying either the voltage of the probe or the current it draws from the plasma, and monitoring the other an experimental characteristic curve may be obtained which yields both the temperature and the density.

The proper operation of a spacecraft mounted Langmuir probe depends on the assumption that the payload itself is well "grounded" with respect to the plasma. In practice this means that the conducting surface area of the payload must be much larger than that of the probe to insure a low impedance return path to the plasma for the current collected by the probe. Failing this the spacecraft itself, which ordinarily develops a sheath potential on the order of the electron thermal energy, may be driven to much larger voltages. For example, if the probe is held at a large positive voltage it collects essentially all of the electrons and none of the protons in its vicinity. This current must be balanced by an equal current of ions to or photoelectrons from the payload surface. Due to the much slower thermal speeds of ions, either a much larger sur-

face area or a very large negative voltage is required of the payload. In fact in the very attempt to drive the probe highly positive, the payload may be driven highly negative while the probe remains near the plasma potential. Spacecraft charging problems cause difficulties with low energy particle detectors which depend on the spacecraft to maintain its potential close to that of the ambient plasma. As will be seen in the next section this appears to have happened during the flight of the probes described here with the result that the RPA's did not function properly at energies above 100 eV.

By applying a positive voltage well in excess of the anticipated electron thermal energy to a Langmuir probe, the current I_0, referred to as the electron saturation current, is collected. For a spherical probe in the ionosphere, where the Debye length is a fraction of a centimeter and sheaths are thus very thin, I_0 is given by

$$I_0 = \frac{1}{4} A n_e e \left(\frac{2KT_e}{m_e} \right)^{1/2} \tag{II.2}$$

where A is the probe area and m_e is the electron mass. In this case the probe was held 6.2 volts positive with respect to the payload. This is well above the thermal energy of the ionospheric electrons which is usually a few tenths of an eV. The current collected by this probe is converted to a voltage and processed by a log amplifier. Both a direct output sampled 1000 times per second and an AC coupled high gain output sampled 2000 times per second are included in the telemetered data.

The current collected by this probe is used to control a constant current source which forces the other probe to collect a small fraction of the electron saturation current, I'. This probe operates in the exponential region of the Langmuir probe characteristic curve. In this region

$$\frac{dI}{dV} = \frac{eI}{KT_e} \tag{II.3}$$

A small sinusoidal variation of amplitude $.1I'$ is added to the bias current at a frequency

$\frac{\omega}{2\pi}$ = 1 kHz. This produces a variation in the voltage of the probe given by

$$\delta V = .1\frac{KT_e}{e}\sin\omega t \qquad \text{(II.4)}$$

This voltage variation is amplified, demodulated, and included in the telemetry data with a sample rate of 250 per second along with an AC coupled high-gain channel of the same data sampled 500 times per second. Using Equation II.2 and Equation II.4 these data determines the electron temperature and density.

II.D. Magnetic field experiment

A two axis flux-gate magnetometer was included on the cannister primarily for attitude analysis. The axes coincided with the x and z axes as shown in Figure II.1 The DC voltage output of each axis was converted by a 12 bit analog to digital converter and telemetered 250 times per second. The instrument had a sensitivity of 10 nT but was limited by the range of the analog to digital converter to a resolution of one bit which corresponded to 28 nT. As such it was potentially useful in detecting the magnetic perturbations due to ionospheric sheet currents which often are several hundred to a thousand nT.

III. LAUNCHES

In February and March of 1976 a campaign was mounted to launch the first two Porcupine payloads from Kiruna, Sweden. Porcupine 1 was launched during this campaign. Unfortunately a malfunction of the Aries launch vehicle resulted in the destruction of the payload about one minute after launch and no useful scientific data were returned. The planned second launch was postponed pending study of the Aries vehicle.

The following year, tests revealed the probable cause of the malfunction - inadequate heat sinking on the motor dome. The problem was corrected and a second campaign was mounted in February and March of 1977 to launch the second payload.

On March 20, 1977 at 19:22 UT (about 22:30 magnetic local time) Porcupine 2 was launched into a quiet arc. The arc diminished in strength in the minutes prior to launch and was too faint to be reliably recorded on all-sky cameras during the flight. Thus no orientation data are available from this source. Poleward of the rocket position, however, a visual form was observed which ran from somewhat south of west to somewhat north of east.

Both UCB instrumented cannisters were ejected properly but for a still undetermined reason data were received from only one of the pair. In addition, boom deployment problems resulted in the re-orientation of this cannister's attitude from its planned configuration.

The cannister was programmed to deploy the four radial booms first to enhance the rotational stability about the intended spin axis with the two axial booms deploying some 20 seconds later. Apparently the radial boom deployment mechanism locked up preventing full extension and possibly causing unsymmetrical extension. When the axial booms were released

the cannister rapidly entered a period of unstable gyration. After about 40 seconds it settled into a very stable flat spin about an axis perpendicular to the axis of symmetry (the z-axis as shown in Figure II.1) and remained in this attitude for the rest of the flight. A good attitude analysis is thus available for times later than TAL (time after launch) = t = 180 seconds. No attitude analysis is available prior to this time.

A second problem was the apparent charging of the payload. As was noted in the previous section, the potential of the spacecraft is determined by the requirements of current balance between its body and the plasma. The usual method of insuring that the spacecraft body remains at ambient plasma potential is to make the area of the spacecraft skin much larger than the ratio of the electron to ion thermal speed times the probe surface area. In the case of the ejectable probes this condition was no more than marginally met. If the current can not be balanced with the spacecraft at plasma potential it will be driven to lower potentials until the reduced electron current to the probe and the enhanced ion current to the spacecraft body satisfy the current balance condition.

As a result of this charging, large fluxes of thermal ions were allowed past the small electrostatic barrier which would otherwise screen thermal ions from entry to the retarding potential analyzers (see Figure II.2a). Once inside the focusing region of the detector, they were drawn to the highly negative walls emitting secondary electrons. These were then drawn to the +1500 Volt entrance of the CEM producing spurious counts. These effects were most noticeable during the high energy end of the RPA sweep because it was at these times that the walls of the focusing region were at the largest negative potentials and thus, that the collisional energies of the ions were the greatest. The result is that low energy electron data were lost at energies above 100 eV.

The trajectory of the cannister is determined from radar data obtained for the main payload. Since the physical separation of the cannisters from the main payload was never more than two km this assumption causes no problems. The payload reached a maximum altitude of

459 km at t = 370 seconds. At t = 373 seconds the barium shaped charge experiment was detonated. Reentry and loss of signal occurred at about t = 660 seconds.

The trajectory is shown in Figure III.1. Note the exaggeration of the horizontal scale. Also included on this figure are lines of constant L or magnetic latitude. Due to the extremely small horizontal range of the flight, the post-apogee portion of the flight provided a magnetic retrace of the pre-apogee portion. This fact was useful in determining the time scale for changes in the observed auroral precipitation.

In Figure III.2 the 110 km altitude magnetic projection of the trajectory is displayed. The dashed line represents the orientation and equatorward edge of the arc encountered during the flight. The orientation is determined from theoretical considerations as explained in the analysis section and corresponds to the approximate orientation of the visual form observed poleward of the rocket position.

IV. DATA

IV.A. Overview

Electron measurements

Figure IV.1 serves as a broad introduction to the important features in the flight data. In all three panels the horizontal coordinate is flight time and runs from t = 120 seconds (shortly after cannister ejection) to t = 660 seconds (re-entry). The top two panels display the electron differential energy flux, Φ, as a function of electron energy and time. The top panel is composed of data from the electron ESA while the middle panel is from one of the RPA's. The RPA data are cut off at 100 eV due to the malfunction referred to in the previous section. The bottom panel displays data from the high frequency electric field spectrum analyzer. Darker regions correspond to greater intensities in all three panels.

The conventional parameter used to report directional particle fluxes is j, the differential particle flux, measured in particles /cm^2 s ster eV. Since $\Phi = Ej(E)$, the differential energy flux tends to make the secondary peak in the electron spectrum stand out more clearly. The auroral fluxes are clearly defined in the ESA data with the spectral peak reaching a maximum of about 4 keV at t = 420 seconds. In fact, except for a brief period from 160 to 230 seconds, the payload was constantly within a region of energetic electron precipitation. The energetic fluxes display a periodic fluctuation in intensity which is due to a beating effect between the energy sweep frequency of the detector itself and the payload rotation frequency. The detector had a view angle of 90° with respect to the final spin axis and the spin axis formed an angle of 30°

with the magnetic field. Thus during the course of one rotation the detector sampled the particle flux at pitch angles from 60° to 120°. As will be shown later in the data presentation, the electron fluxes are greater over the downward pitch angles. This results in apparent temporal fluctuations due to the variations in detector view angle during successive sweeps. The pitch angle distribution of the energetic electrons will be discussed later in this section.

The RPA data essentially follow the ESA data displaying higher intensities in the low energy electrons corresponding to increases in the primary beam energy. This result is expected due to the enhanced production of secondary electrons through collisions with neutral particles in the ionosphere. These secondary electrons are much more isotropic and thus no beating effect as seen in the ESA data occurs.

Between 360 and 420 seconds there are four brief intensifications noticeable in the RPA data. The first of these is an artifact of the barium shaped charge experiment which was detonated at $t = 373$ seconds. The apparent intensification at about 40 eV is merely a result of the fact that the shock front of the expanding barium cloud happened to pass the location of the cannister at a time when the RPA was sampling fluxes at that energy. The other three events, all at an energy of about 25 eV, are real. In the first and last of these events the intensification lasts for no more than the duration of a single energy sweep ($\approx$ one second) and thus we cannot be sure that we are not observing a very brief enhancement that is occurring at all energies. However in the second event the intensification exists to some extent for at least two sweeps. The two other RPA's not shown here show similar enhancements at the same times and over a variety of pitch angles. This evidence and the fact that all the events occur at similar energies seem to imply that the phenomena are similar and do represent a brief enhancement in the electron flux over a limited energy range near 25 eV.

AC Electric field

The bottom panel of Figure IV.1 displays the power in the high frequency electric field fluctuations as observed by the spectrum analyzer. There are several features of this plot which require explanation. The periodic vertical sets of five dark rectangles are frequency calibration markers generated by an onboard oscillator to provide reference frequencies for inflight calibration. The dark bands which run across the top of the panel are short wave radio transmissions. Their momentary disappearance during re-entry is due to the elevated cutoff frequency produced by the enhanced electron density in the lower ionosphere. Also plotted on this panel are the electron plasma frequency as determined from electron density measurements and twice the electron gyrofrequency as determined from the model magnetic field, both at the payload position. These frequencies will be important in the analysis of the spectrum analyzer data. The cyclotron frequency is observed to change slowly as the payload moves in altitude. Likewise the electron plasma frequency decreases as the payload moves to regions of lower electron density at higher altitudes. The major perturbation in the middle of the flight is once again a result of the barium shaped charge experiment. The initial drop in plasma density is a result of electron attachment to the chemical byproducts of the explosion. Within a few seconds photoionization of the neutral barium produces a dramatic enhancement in the plasma density which then decays slowly over the course of the next 40 seconds.

There are several instances of isolated bursts at the plasma frequency and twice the electron gyrofrequency in the early part of the flight. By far the most dramatic event occurs after the barium detonation around $t = 400$ seconds. Large amplitude waves occurred along the $2f_{ce}$ line for about 15 seconds following the decay of the locally elevated plasma frequency to a value below twice the electron cyclotron frequency. These emissions culminated in a brief burst of waves over a wide range of the spectrum. We will return to these data and examine them in much greater detail later.

DC Electric Field

Figure IV.2 displays the southward and westward components of the electric field perpendicular to the magnetic field and the total electric field as a function of time as observed in a geographic (corotating) frame of reference. The observed component of the electric field parallel to the magnetic field is consistent with zero. No data are presented prior to t = 180 seconds due to the lack of an adequate attitude solution during the early portion of the flight. The large perturbation in the data at t = 373 seconds is once again an effect of the barium shaped charge experiment which produces a momentary perturbation of the plasma flow velocity and thus the observed electric field.

Figure IV.3 shows the magnetic projection of the observed DC electric field to an altitude of 110 km. The plasma flow implied by the resulting E×B drift is generally equatorward and of much larger magnitude outside the arc than inside.

Ion measurements

Throughout the flight the counting rates detected by the ion ESA were too far too low to be statistically significant without averaging over long times. Even then most counts are due to detection of scattered ultraviolet from those times that the instrument viewed angles close to the sun. Figure IV.4 is an example of a spectrum obtained by averaging ion data for 50 seconds starting at t = 250 seconds. This spectrum is representative of that seen throughout the flight. As a result of the general lack of energetic ions, the ion composition experiment also yielded no data of interest.

Magnetometer data

As was discussed in the instrumentation section, the magnetometer data were used primarily for attitude analysis. However, by subtracting the model magnetic field from the

observed data, field-aligned and ionospheric sheet currents may be revealed as perturbations in the residual field. The residual noise limited the resolution of magnetic perturbations to about 25 γ. This would correspond to a sheet current of about .02 A/m. No field-aligned sheet currents of this magnitude were discerned in the data. Just before the end of the data, a perturbation of about 90 γ was observed. This is attributed to an E-layer sheet current of about .08 A/m which was traversed on reentry.

IV.B. Anticorrelation of electric field and electron precipitation

Comparison of the top panel of Figure IV.1 and the bottom panel of Figure IV.2 shows that the variations in the total electric field closely mimic, in an inverse sense, the variations in the peak energy of the auroral electrons. In Figure IV.5 the inverse of the DC electric field is plotted along with the secondary peak energy of the simultaneously observed precipitating electrons. It has been noted in numerous sets of auroral data that the ionospheric electric field decreases and sometimes increases (De La Beaujardiere, 1977) within auroral arcs but it is interesting to note the remarkable degree of anticorrelation which occurs within this arc. The two temporary retreats in the peak electron energy as the aurora gains in strength are reproduced quite faithfully as temporary recoveries in the electric field strength which generally decreases during this portion of the flight. The detailed relationship between the particle fluxes and the electric field will be explored in detail in the analysis section.

IV.C. Electron distribution function

One of the more interesting results of this flight was the observation of changes in the distribution function of the precipitating electrons apparently associated with the occurrence of the barium plasma injection. In the statistical description of plasma dynamics the distribution function, $f(\mathbf{r},\mathbf{v})$, which is the number of particles per unit volume in phase space, is used.

Typically, particle flux measurements are reported in terms of the differential particle flux, $j(E,\alpha)$, which is the number of particles hitting a unit area per unit incident solid angle per unit time per unit energy at the energy E and the pitch angle α. With the appropriate change in variable dependences it is easily shown that these two functions are related by

$$f = \frac{m^2}{2E} j \qquad \text{(IV.1)}$$

In the discussion which follows we will use the quantity j/E when referring to the distribution function.

Due to the unanticipated change in attitude of the cannister, the electron ESA monitored electron fluxes at pitch angles between 60 and 120 degrees. Figure IV.6 displays two sets of electron distribution functions as measured by the electron ESA, one from before the barium injection and one from afterwards. These data are obtained as the cannister rotates and no attempt to sort them by pitch angle has been made here. Nevertheless a clear difference is noticeable in the fact that the pre-barium distribution functions display a marked peak at 2 to 3 keV while the post-barium distribution functions do not. The one non-peaking case in the pre-barium examples occurs at a time when the payload attitude gave the electron ESA a view of electrons with pitch angles greater than 90 degrees, that is electrons moving upward.

These data may be more clearly presented in the form of a polar plot of iso-intensity distribution function contours as in Figure IV.7. This figure displays distribution function contours in electron velocity space. The left (right) half of the figure represents the distribution function before (after) the barium injection. Notice that data are obtained only between 60 and 120 degrees. The rest of the figure is drawn in as an educated guess based on an extrapolation of these data and results of previous observations and should not be taken too seriously. On this plot the thermal electrons are represented by an intense narrow spike at the origin while the secondary electrons formed by the collisional interaction of the primary beam with the atmosphere is seen as the broad, downward sloping portion at moderate velocities.

The pre-barium distribution function contours are characterized by a ridge at downward pitch angles which is eroded into a plateau following the barium injection. The ridge begins to recover about 60 seconds after the barium detonation but never regains its pre-barium magnitude. There is good evidence that the distribution actually peaks close to 90 degrees.

Such secondary peaks in particle distribution functions are well known sources of free energy for the growth of plasma waves. The deterioration of the electron distribution peak will be explored in more detail in the analysis section.

IV.D. High-frequency plasma waves

Figure IV.8 displays twelve successive half second sweeps of the high frequency spectrum analyzer including the period of intense emissions near $t = 400$ seconds referred to earlier. In the first sweep the most prominent features are a sharp line at the upper hybrid frequency ($\approx$ 2.4 MHz) and a broader line at the plasma frequency ($\approx$ 2.05 MHz). In successive sweeps the upper hybrid emission grows to very large magnitude and then dies away. Figure IV.9 is a detailed version of the seventh of these sweeps and shows the richness of the observed spectrum very clearly.

The upper hybrid line is so sharp that it is not resolved by the instrument. Assuming its width to be equal to this resolution, a lower bound for the line strength may be computed. Such a calibration is used for the abscissa in Figure IV.8 and Figure IV.9 instead of the usual mV/m /Hz$^{1/2}$. A line strength reading of 1 mV/m corresponds to a spectral density of .033 mV/m /kHz$^{1/2}$. The upper hybrid emission line strength calculated in this manner is greater than 20 mV/m during the strongest portion of the emissions.

As the upper hybrid emission grows waves at a large variety of frequencies are observed. At least two and perhaps three sidebands emerge at 200 kHz intervals on either side. On the low frequency side these sidebands ride on the back of a broad plasma frequency emission. A

pair of lower frequency emissions at 200 and 400 kHz, several small very high frequency (4-5 MHz) oscillations, and finally a large emission feature at $\approx$ 650 kHz are also observed during this period.

Several of these emissions fit well into the picture of a parametric decay process taking energy from the upper hybrid pump wave and distributing it into the sidebands and the 200 and 400 kHz emissions. Also the emissions appear to be stimulated in some manner by the presence of the barium cloud. These waves, their relation to the barium cloud, and the changes observed in the electron distribution function will be analyzed more thoroughly in the analysis section.

IV.E. Summary

To review the main points of the data, the payload was in a soft precipitation region equatorward of a quiet arc from t = 165 seconds to t = 230 seconds. For the rest of the flight it encountered auroral electron precipitation at energies up to 4 keV. The DC electric field magnitude showed a remarkable degree of anticorrelation with fluctuations in the peak energy of the precipitating electrons. At t = 373 seconds a barium shaped charge experiment was detonated causing a large plasma density enhancement surrounding the payload. Immediately after this the local electron distribution function lost the prominent peak which it had previously displayed at downward pitch angles. Several brief enhancements in the flux of 25 eV electrons were observed. A strong emission at the upper hybrid frequency began when the local plasma frequency returned to the low side of the second electron cyclotron harmonic and ended in an intense burst of plasma emissions at a large number of frequencies.

In the next section we will discuss possible mechanisms for these observations.

V. ANALYSIS

V.A. On the control of the ionospheric electric field

A simple model and some considerations

The remarkable anticorrelation between particle precipitation and the electric field seems to imply a controlling influence of one phenomenon over the other. The relationship at once suggests the possibility that the ionospheric conductivities are modulated in a temporally responsive fashion by the instantaneous electron precipitation and its ability to enhance the plasma density in the lower ionosphere. The presence of a large scale ionospheric current system might then determine the ionospheric electric field and produce the type of inverse relationship observed here.

What might be required to produce the observed anticorrelation? One could at first be led to consider the relationship of the ionospheric electric field to the field-aligned electric field which produces the energetic electrons. An application of $\int_c \mathbf{E}\cdot d\mathbf{l} = 0$ to closed paths linking the magnetosphere to the ionosphere might be expected to yield a type of inverse relationship between the field-aligned potential drop and the ionospheric field. As a result, a relationship of the form E + constant·(PeakEnergy) = constant might be obtained. A quantitative model of this sort is impossible due to our lack of knowledge of the boundary conditions, namely - the magnetospheric potential configuration. However, for the simple assumption that $E_{max} = 0$ or E_{max} = constant, Figure V.1a and b displays the resulting ionospheric and peak electron energy profiles. Figure V.1b differs from Figure V.1a only by virtue of an offset imposed on the

ionospheric electric field by the magnetospheric potential gradient. No inverse relationship is evident in either of these cases. On the other hand, Figure V.1c shows that it is possible to construct a potential configuration for the magnetosphere which produces the postulated relationship (or any other relationship). We view this possibility as remote, especially when the contortions required to reproduce the complex peak energy profile of this arc are considered.

An alternative model could be constructed as follows. First the ionospheric conductivities should vary in direct proportion with the peak energy of the precipitating electrons. This would be due to the enhanced ionospheric electron density created by the energetic electron precipitation. Second the ionospheric currents perpendicular to **B** should be constant in both time and space. That is, the currents are determined by large scale features of the magnetosphere-ionosphere interaction and are relatively unaffected by the arc. Implicit in this assumption is the requirement that negligible field-aligned currents flow in the region of interest since they would lead to a divergence of and therefore a variation in the ionospheric current system. Even though substantial field-aligned currents are known to flow in auroral arcs, this assumption is not unreasonable. Maximum field-aligned current densities are typically a few $\mu A/m^2$ and even a 10 km wide region of such a current density would produce only a few hundredths of an A/m of field-aligned sheet current. Ionospheric sheet currents can easily reach an A/m and thus will be relatively unaffected by such a field-aligned sheet current. Under these assumptions the electric field would be inversely proportional to the conductivity and, thus, the peak energy of the precipitating particles.

Electric field measurements in the ionosphere are highly frame dependent and thus any attempt to link measured electric fields with other measurements must be approached with caution. For calculations involving the classical Hall and Pedersen conductivities the proper frame in which to work is that of the neutral particles. Unfortunately this frame is neither well-defined, due to large shears in the neutral wind velocity with altitude, nor even measured in most cases. Thus the effective electric field for current calculation purposes may be altitude

dependent due only to the altitude dependence of the neutral frame itself and, worse yet, completely unknown.

Furthermore there are several problems with this model. Time variations in the precipitation are not considered. Also the fact that the current is actually related to the electric field through a tensor and not a scalar conductivity complicates the problem.

When the electron precipitation varies there is a time lag associated with the build up or decay of the plasma density. The equation governing the electron density, n, in the presence of a production rate, q, and a recombination coefficient, α, is

$$\frac{dn}{dt} = q - \alpha n^2 \qquad \text{(V.1)}$$

The recombination rate is effectively a function of altitude through its dependence on the temperature. The production rate is also a function of altitude. Due to the non-linearity of Equation V.1 the time scales for build-up and decay of the electron density are functions of the strength of the aurora as well as the altitude. For stronger precipitation the recombination term becomes important more quickly and the electron density "tracks" the changes in the precipitation more closely. Jones and Rees (1973) used a model ionosphere and a typical auroral precipitation profile to calculate the time constants for electron density build-up and decay. The times vary from 5 to 70 seconds in the altitude range considered. The fastest time constants occur in the E-region which is where the major contribution to the ionospheric height integrated conductivities is found. Thus one might expect typical lags on the order of ten seconds between precipitation changes and conductivity changes. Note that this effect is important even in the case of steady precipitation if there is motion of the ionized component relative to the arc. For example, flow across an arc would be expected to produce enhanced conductivities downstream from the arc and anomalously low conductivities within the arc. Since plasma flow speeds may be as high as 1 or 2 km/s and auroral thicknesses can be on the order of a few km, the plasma may be able to completely traverse an arc in a time less than the build-up or

decay time constant. This would lead to reduced conductivities within the arc and an extended downstream region of enhanced conductivities relative to those expected in a non-flow situation.

Another complicating effect of time variations is seen in the fact that the electric field itself may not be able to change instantaneously even if the conductivities could. In the absence of wave turbulence generated anomalous resistivity along magnetic field lines, the ionospheric electric field is coupled to the magnetosphere due to the high field-aligned D.C. conductivity of the magnetospheric plasma. Changing the ionospheric electric field is then equivalent to altering the plasma convection velocity and thus the momentum of all the magnetospheric plasma contained in the flux tube linking the region of the ionosphere under consideration. Anomalous resistivity effectively decouples the motion of the magnetospheric plasma from that of the ionospheric plasma by enabling field-aligned potential drops to exist. In this case it might appear that rapid changes in the ionospheric electric field would be possible since the inertia of the magnetospheric plasma has been removed. We must remember, however, that we are talking about time variations in the ionospheric electric field and thus we need to consider the A.C. field-aligned conductivity. This A.C. conductivity is determined by the properties of Alfven waves which transmit the perturbation electric field along the field lines. Thus, for time varying electric fields, the inertia of the magnetospheric plasma still plays a role. When the precipitation and thus the ionospheric conductivities change in a limited spatial region, a non-zero divergence of the horizontal current system in the ionosphere creates charge layers at the boundaries. This divergence cannot persist and is eventually eliminated in one or a combination of two ways. If A.C. field-aligned currents are somehow prevented from flowing the ionosphere will polarize until the resulting electric field once again permits a divergenceless horizontal current system. If, on the other hand, A.C. field-aligned currents are completely unimpeded they might account for any divergence with no need for polarization.

In fact neither of these mechanisms can exist in the absence of the other. In the first case complete polarization would imply a decoupling of the ionospheric electric field from that of the magnetosphere. This situation would soon be eliminated by field-aligned currents driven by the resulting field-aligned potential difference. The polarization field created in the ionosphere will eventually be communicated to the magnetosphere. In the second case, field-aligned currents imply the flow of charge which will inevitably be accompanied by a perturbation electric field. In other words the ionosphere must polarize to some extent to drive the field-aligned currents.

Thus the only self-consistent solution of the problem is a combination of the two effects. The question of which is the dominant process can be answered by looking at the relative impedances of the two return paths available for the polarization charge created by the initial divergence. Mallinckrodt and Carlson (1978) have shown that the conductivity for field-aligned currents associated with perturbation fields, the so-called wave conductivity, is on the order of .5 mho while auroral ionospheric conductivities are typically 10 mho. Thus, in fact, A.C. field-aligned currents are also relatively highly impeded. Over the course of time a new D.C. configuration is established. Goertz and Boswell (1979) have determined that the steady state currents are achieved on time scales of the order of hours. As a result the ionosphere does polarize but the inductive effects of the momentum of the plasma on the magnetospheric flux tube delay the establishment of the steady state electric field. Once again this time dependence need only occur in the frame of the plasma and so convection plays an important role in this process as well.

Finally the model is incomplete because of its failure to account for Hall currents which can be even greater than the normal Pedersen currents. Since the ionospheric currents do not flow in the direction of E and since variations in the auroral electron density affect the Hall and Pedersen conductivities differently, one cannot simply assume that a constant and uniform ionospheric current traversing ionospheric plasma density variations will lead to an inversely related electric field. Obviously we must be more precise in the mathematical description since

the relationships are more complicated than indicated by our simple model.

The numerical simulation and application to flight data

In an attempt to understand the observed anticorrelation, a numerical procedure was developed to simulate the electrodynamics of auroral ionospheric phenomena. The routines are described in detail in the appendix and the reader is referred there for a more detailed discussion of the calculational procedure. In the following discussion we refer to the coordinate system defined there and shown in Figure V.2. The assumptions of the numerical routine limit us to considering only those cases in which there is a sensible "arc frame" in which all quantities are time independent and in which $\frac{\partial}{\partial y}$ (the longitudinal gradient) vanishes. Both of these assumptions are fairly well justified due to the fact that the visible aurora displayed the typical longitudinal extension and lack of dynamics of a quiet arc.

Under these assumptions and the further assumption of a negligible field-aligned component of the electric field (well justified below 250 km), it is required that E_y be constant throughout the region and time of interest. The electric field data from the flight indicate a fairly constant component in a direction approximately 30° south of west. Figure V.3 displays the electric field of Figure IV.2 rotated by 30° into this orientation. Notice that, with the exception of the barium perturbation, E_y is fairly constant for a good portion of the flight. The particular arc that the rocket penetrated was too faint to be observed by all sky cameras. However this direction corresponds well with the observed orientation of the arc poleward of the rocket position. Since multiple arcs generally align themselves in similar directions we choose this orientation as the most likely direction of extension for the arc.

Next we must determine the motion of the arc frame relative to the geographic frame in which the electric field measurements are reported. Figure IV.1 reveals a certain degree of symmetry in the particle precipitation about $t = 420$ seconds. This time is very close to the

time at which the payload reverses its direction magnetically as shown in Figure III.1 and Figure III.2. Thus a likely possibility is that the arc is essentially motionless in a geographic frame and the rocket merely penetrates to a position which may even be equatorward of the maximum energy electron precipitation. Notice that only motions in the x-direction are perceptible due to the assumption of vanishing y dependence. Thus the y-component of the arc's motion is arbitrary at this point. Some time variation clearly occurs since the particle spectra are slightly different during the downward portion of the flight when the payload retraces the magnetic coordinates of the upward leg. These differences are slight and occur on a time scale of minutes. As was pointed out above, the electron density in the ionosphere requires times of the order of tens of seconds to adjust to changes in ionization rates. Thus the steady state assumption seems well justified.

The data between 220 and 410 seconds were used to obtain average precipitating particle spectra at one kilometer intervals from the equatorward edge of the arc to the maximum penetration position. This corresponds to a total distance of 32 kilometers perpendicular to **B**. Notice that during the interval between 380 and 445 seconds the payload's motion transverse to **B** was limited to about one kilometer.

Using these spectra and an ionospheric model, ionospheric production rates, q, were calculated. The program uses the collisional ionization algorithm of Rees (1963) in a manner similar to Evans (1977). Although there is some evidence that non-collisional processes may be important in limiting the altitudinal extent of the ionization produced (Stenbaek-Nielsen and Hallinan, 1979), such processes seem to be more important in pulsating auroras. Once again, see the appendix for more details on the calculational procedure. To calculate the equilibrium electron densities, we must know v_i, the velocity of the ionized component relative to the arc frame. The y-component of v_i is irrelevant for the calculation of the convective derivative of the electron density so we choose it to be zero and let v_i be the component of the ionization drift in the $+x$-direction. As a first approximation we will assume no drift. In this case there

is no problem with time constants for ionization build-up and decay and the steady state may be assumed. In the steady state, the electron densities are determined from

$$n = \sqrt{q/\alpha} \tag{V.2}$$

These densities are then used to calculate the height integrated Hall and Pedersen conductivities. Figure V.4 displays the calculated height integrated conductivities as functions of position within the arc.

Now note that in our model

$$\frac{\partial}{\partial x} I_x = -j_{\parallel} \tag{V.3}$$

where I is the height integrated current perpendicular to B and $j_{\parallel}$ is the field aligned current density into the ionosphere. (Recall that $\frac{\partial}{\partial y} I_y = 0$ in this model.) In accordance with the magnetometer data which indicate no appreciable field-aligned currents (see discussion of magnetometer data in the data section), we set $j_{\parallel} \equiv 0$ yielding I_x = constant. Notice that I_y need not be constant with respect to x.

The use of our conductivities to determine the relationship between the electric field and the particles is hindered by one major gap in our information - the neutral wind speed. The relationship

$$\mathbf{I} = \begin{pmatrix} \Sigma_P & -\Sigma_H \\ \Sigma_H & \Sigma_P \end{pmatrix} \cdot \mathbf{E} \tag{V.4}$$

is true only in the rest frame of the neutral particles. To perform the calculation in the arc frame we must correct the electric field and obtain

$$\mathbf{I} = \overline{\Sigma} \cdot (\mathbf{E} + \frac{\mathbf{v}_n}{c} \times \mathbf{B}) \tag{V.5}$$

where $\mathbf{v}_n$ is the neutral wind velocity with respect to the arc frame. Note that the current is independent of reference frame under the assumption of quasi-neutrality for the ionospheric plasma.

Notice that in Equation V.5 v_n is assumed to be independent of altitude. This is clearly not generally the case, however the fact that the ionospheric current flows predominantly in an altitudinally thin layer of about 20 km around the position where the conductivities peak might mean that as long as an average neutral wind velocity in that region is used, the error could be small. In fact even in this limited region the neutral wind shears can be as large as 100 m/s (Roble *et al.*, 1979) but with no data available we must make the assumption as noted. We further assume v_n to be independent of x. Then from Equation V.3 and Equation V.5 we find that specifying E_x at one position determines E_x at all other positions. Specifically,

$$E_x'(x) = \frac{E_x'(0)\Sigma_P(0) - E_y'\left[\Sigma_H(0) - \Sigma_H(x)\right]}{\Sigma_P(x)} \tag{V.6}$$

where $\mathbf{E}' = \mathbf{E} + \frac{\mathbf{v}_n}{c} \times \mathbf{B}$ It is convenient at this point to specify the y-component of the the neutral wind velocity relative to the arc frame to be equal to zero. This can be done without loss of generality. Figure V.5 shows the relative velocities between the geographic, arc, and neutral frames. Since the electric field measurements are presented in a geographic frame, we must transform them to the arc frame. With this choice of neutral wind speed, which is equivalent to specifying the as yet unspecified y-component of the arc frame velocity relative to the geographic frame, it is a simple matter to transform the geographic electric field to the arc frame. The transformation is given by

$$E_x = E_x^G + \frac{u_y}{c} B \tag{V.7}$$

$$E_y = E_y^G - \frac{u_x}{c} B \tag{V.8}$$

where u_y is the y-component of the neutral wind velocity relative to the geographic frame and u_x is the x-component of the arc velocity relative to the geographic frame.

With this choice Equation V.6 can be written

$$E_x(x) = E_x(0)\frac{\Sigma_P(0)}{\Sigma_P(x)} - \left(E_y - \frac{v_n}{c} B\right)\left[\frac{\Sigma_H(0) - \Sigma_H(x)}{\Sigma_P(x)}\right] \tag{V.9}$$

where v_n is to be taken positive in the $+x$-direction and negative in the $-x$-direction. In our first approximation we have already taken $v_i = u_x = 0$. We will now also assume $u_y = v_n = 0$. Thus we can use the electric field data of Figure V.3 , the conductivities of Figure V.4 , and Equation V.9 to compare the model to the data. To do this the position of maximum poleward penetration at $t = 410$ seconds is chosen as $x = 0$. The x-component of the electric field at this time was essentially zero so we set $E_x(0) = 0$. Also, in the time interval of interest E_y was relatively constant at about 19 mV/m so we choose this value for E_y. The results of applying Equation V.9 to these values are shown in Figure V.6. In this figure $E_x(x)$ as calculated is compared with the observed $E_x(x)$. The transformation of the data of Figure V.3 to that of this figure involves the use of only that portion of the data between $t = 220$ and 410 seconds, reversing its order, and accounting for the fact that the x-component of the payload velocity was not constant during this interval.

As expected, the figure shows general agreement in the broad features but there is room for improvement. In particular the field equatorward of the arc is much too great. Also the data curve is much smoother than the calculated curve.

Both of these problems can be overcome by recognizing the effects of finite arc motion and plasma convection. As noted previously, these have the effect of introducing time variation into the precipitation seen by a given element of the ionospheric plasma. Then build-up and decay times become important and the plasma density at any point is a function of the precipitation it has experienced over the past minute or so. Thus we now need to consider more realistically the probable values for v_i, v_n, u_x, and u_y. We will start by pointing out some of the general considerations which limit the possible values of these parameters.

First, neutral wind speeds rarely exceed 200 m/s (Hays *et al.*, 1979). As a result u_x and $u_x + v_n$, the components of the neutral wind velocity in a geographic frame, should be no larger than this. Notice that v_n itself is not restricted since it is the speed of the neutral winds relative to the arc frame.

Second u_x is probably not very large. As was pointed out before, the electron precipitation data imply that the arc was both fairly steady and motionless in the geographic frame. Assuming as we have that the variations in the data are spatial and not temporal, an arc speed of more than about 100 m/s would have shifted the observed symmetry noticeably away from the point of maximum poleward magnetic position.

Finally, what can we say about v_x, the x-component of the ionization drift velocity in the arc frame? At high altitudes v_x is clearly just the normal E×B plasma drift. At very low altitudes it is the neutral wind speed since the plasma becomes collision dominated. What about in between? At what height does the transition take place and how does v_x behave in the transition region? As discussed in the appendix, the transition takes place below 100 km. Since almost no ionization occurs below this altitude in an arc as weak as this one it is reasonable to assume v_x to be equal to the x-component of the plasma drift in the arc frame.

For the moment let us consider the effect of this non-zero v_x on the previous results. Since E_y = 19 mV/m, we actually have a southward v_x of about 380 m/s. At this speed plasma will cross the 32 km of the geographic frame in which we have collected data in about 80 seconds. Considerable smearing out of the plasma density is expected and an equatorward region of enhanced conductivity will be produced thus decreasing the calculated electric field there. Figure V.7 shows the effect of including this drift on the height integrated conductivities. The microstructure evident in the particle precipitation is now completely gone. In order to obtain the observed electric field, a large and fortuitously arranged divergence of the horizontal current system associated with field-aligned current densities on the order of 50 μA/m^2 would be required. Clearly a plasma drift relative to the arc frame of this magnitude is unacceptably large for our present model. This difficulty can be overcome in two ways - an equatorward arc motion or enhanced recombination coefficients.

If the arc has a significant equatorward motion, E_y and thus the speed of the ionized component relative to the arc are reduced. This results in less smearing out of the ionospheric

plasma density. Figure V.8 shows the height integrated conductivites resulting from various values for u_x, equivalent to choosing lesser values for E_y in the arc frame. Notice that as u_x increases, the arc width also increases due to the fact that the data under consideration are obtained from the poleward going portion of the flight and any equatorward arc motion implies an increased arc thickness. The relative positioning of features in each case also shifts due to the non-linear mapping between flight time and magnetic latitude.

Figure V.8 shows that in order to minimize the smearing effect of v_i, E_y must be less than 5 mV/m. This corresponds to a u_x of more than 300 m/s, three times the likely upper limit placed on the arc motion above. In addition for such rapid arc motions, the inferred arc thickness is over 100 km. Thus it does not seem that arc motion can be invoked to diminish the effects of plasma motion across the arc.

If the recombination coefficients are increased we will obtain a decreased time constant for plasma density equilibration. This could decrease the smearing effect without the need for large arc velocities. A side effect, however, is that the steady state plasma density is also decreased. As a result the conductivities are also decreased. Equation V.1 implies that for small changes in q, the time constant, τ, for changes in the equilibrium density is approximately,

$$\tau = \frac{1}{2\sqrt{q\alpha}} \tag{V.10}$$

so that to decrease τ by a factor of three, α would need to be changed by an order of magnitude. The equilibrium densities and conductivities would also be decreased by a factor of three. It does not seem likely that the height integrated conductivities should be so low (see e.g. Brekke *et al.*, 1974), nor does it seem probable that the values used for the recombination coefficient are in error by an order of magnitude. Thus we are inclined to dismiss this possibility as well.

The conclusion reached after these considerations is that the ionized component must somehow have a smaller velocity with respect to the arc than would be obtained from using the

E×B drift. The results of our more naive model in which v_i was an independent parameter are closer to the observed data. Perhaps the transition to the E×B drift speed occurs at a higher altitude than obtained from our model. This could be due to an underestimate of the neutral atmosphere density or the temperatures at higher altitudes, leading to an underestimate of the electron-neutral and ion-neutral collision frequencies. In the remaining discussion we will assume that, for whatever reason, $v_i = u_\perp = 0$ and note that a small v_i ($\leqslant$ 50 m/s) would be adequate to smooth the results of the simulation while any larger values would begin to eliminate the observed correlation.

We would like to now consider the effects of v_n and $u_\perp$ on the simulation. Recall that $u_\perp$ is the y-component of the neutral wind velocity relative to the geographic frame and that it is used to conveniently fix the otherwise irrelevant y-component of the arc velocity. A non-zero value of $u_\perp$ is manifested by a zero-level shift on the observed values of $E_\perp$. For instance, if we chose $E_\perp(0) = 5$ mV/m instead of the observed 0 mV/m in the geographic frame, a neutral wind speed of

$$u_\perp = c\frac{(E_\perp(0) - E_\perp^G(0))}{B} \tag{V.11}$$

or about 100 m/s, westward, (since $E_\perp^G(0) = 0$ in this case) is implied. Recalling that neutral wind speeds rarely exceed 200 m/s we will limit ourselves to values of $|E_\perp(0)|$ less than 10 mV/m. We will also limit ourselves to values of $|v_n|$, the x-component of the neutral wind speed, less than 100 m/s. This, more stringent, restriction results from our conclusion that the ionized component was somehow more rigidly tied to the neutral particles and that the speed of the former was very small.

Figure V.9 displays the $E_\perp$ profile resulting from the application of our numerical procedure to the data with $u_\perp = v_i = 0$ and various values of $u_\perp$ and v_n. The figure shows that the $E_\perp$ profile is very sensitive to the choice of $E_\perp(0)$ and also fairly sensitive to the choice of neutral wind speed. Notice that regardless of the neutral wind speed chosen, $E_\perp(0) = -10$ mV/m

produces profiles with values of E_x > 200 mV/m, a value rarely observed in the ionosphere.

At this point it is necessary to ask ourselves what features constitute a good fit to the data. If we settle on reproducing the observed net change in E_x of 93 mV/m (0 to -93 mV/m in the geographic frame) then we discover that a range of choices for u_y and v_n is possible. The values are, however, dependent and the dependence may be fairly accurately expressed by the relation

$$u_y = 100\text{m/s} - .6v_n \qquad \text{(V.12)}$$

within the range of acceptable values for the parameters. If, on the other hand, we concentrated on reproducing the overall form of the observed E_x profile or some portion of that form, a different conclusion might be reached. In general u_y and v_n will be dependent on one another and a certain range of values for one will produce acceptable results provided the other is properly adjusted. Since we did not measure the neutral wind speed we can say no more except to note that the observed E_x profile can be fairly accurately reproduced with reasonable values of u_y and v_n.

Finally we would like to discuss the basic source of the observed anticorrelation. As was pointed out in the discussion of the simple model, the inverse relationship between the electric field and the precipitating particles would seem to imply a linear relationship between the height integrated conductivities and the energy of the auroral electrons. The simulation routine was used to calculate the conductivities as a function of peak energy for three different values of the source temperature. The source temperature is the temperature of the plasma sheet electrons which are accelerated to become the auroral beam and is essentially a measure of the slope of the distribution function above the secondary peak. Figure V.10 shows the results of these calculations. Notice that regardless of the source temperature, the conductivities are fairly linear functions of the peak energy for energies between 1 and 4 keV, the energies observed in this rather mild arc. For higher energies the Pedersen conductivity in particular levels off. This is a result of the increased ionization at lower altitudes which does not enhance the Pedersen

conductivity nearly as much as the Hall conductivity. Therefore, for more intense arcs the linear behavior is non-existent and the anticorrelation would be expected to be less exact.

V.B. On the high amplitude wave observations and the wave-particle effects

In the previous section it was shown that the electron distribution function undergoes a rapid change after the detonation of the barium shaped charge experiment. The large secondary peak at downward pitch angles which was present in the pre-barium data is flattened into a plateau in the post-barium data. The introduction of the barium into the ionospheric plasma appears to have acted as some sort of catalyst for a process which removes the free energy in the distribution function which is represented by the secondary peak. Barium shaped charge experiments have been observed to stimulate lower frequency, ion cyclotron waves (Koons and Pongratz, 1979) due to the direct impulse of the explosion. The observations reported here appear to depend only on the presence of the barium cloud and not on the explosion or plasma turbulence associated with the explosion.

The question might be raised, how can the peak survive at all? Such secondary peaks require a region of positive slope in the distribution function which is one of the most fundamental sources of plasma instability. Plasma waves which can interact with the electrons in the unstable region may extract energy from the particles causing a redistribution of particles from higher energies to lower energies and thus eliminating the peak. In the linear theory, the rate at which these waves convert the free energy of the particles into wave energy is proportional to the amplitude of the wave itself. The process is described in terms of an exponential growth rate, γ, which depends on the wave mode and the particle distribution function.

A particle distribution function is not necessarily unstable as a result of the existence of such a secondary peak. The question of instability can only be answered by detailed calculations based on the dispersion relations of all applicable wave modes and the entire particle dis-

tribution function. A great variety of deviations from a Maxwellian distribution may result in the growth of certain wave modes.

In auroral arcs, the particles that these waves interact with are not a fixed population. The auroral beam is produced continuously by the acceleration region. Thus in order for the waves to have an appreciable effect on the observed distribution function, they must be of sufficient amplitude that the power they extract from the beam is comparable to the power input to the particles in the acceleration region.

In order for the waves to attain these amplitudes they must remain in contact with the auroral beam for some time. This requirement may be difficult to achieve since the auroral beam is typically confined to a latitudinally narrow volume of space (Maggs, 1976; Maggs, 1978). For wave packets with group velocities perpendicular to the auroral strip, unless $\gamma >> v_g/w$ where w is the width of the auroral beam, the wave packets will not grow to any appreciable amplitude before they leave the arc and their effect on the observed particle distribution will be negligible.

The restriction is not nearly as severe if the wave packets travel along the arc. Such a case has been treated by Maggs (1976) and the extended period of auroral contact may result in substantial growth for certain wave modes. The requirements on the auroral geometry however are such as to rule out such a mechanism in all but a small number of real cases.

Thus in general the beam is effectively stable by virtue of its limited spatial extent and the resulting brief period of contact for the waves. In the first half of the flight the particle data indeed reveal a stable secondary peak. The high frequency wave data indicate only occasional emissions near the plasma frequency and at the second electron cyclotron harmonic. Notice that at the times of the latter emissions the plasma frequency has dropped to a value which would make the upper hybrid frequency, $\omega_{uh}^2 = \omega_p^2 + \omega_c^2$, essentially the same as the second electron cyclotron harmonic. This fact will be important in the subsequent analysis of the

dispersion relation for these waves. These occasional emissions may correspond to the arrival in the vicinity of the ejectable probe of wave packets which have been fortunate enough to remain within the auroral beam for relatively long periods. Still their existence in any one location is of too transient a nature to cause any noticeable redistribution of the auroral electron distribution. The occurrence of the barium detonation alters both of these observations. The auroral beam is rapidly eroded, eliminating the region of positive slope from the distribution function, and very large amplitude plasma waves are observed for an extended period. Evidently the barium cloud has somehow formed an environment conducive to energy transfer from the beam to the plasma waves.

Dispersion relations

Now we would like to examine the dispersion characteristics of waves at the observed frequencies. Notice in Figure IV.1 that the most prolonged emissions occur at twice the electron cyclotron frequency. Weaker emissions occur simultaneously at a frequency corresponding to the unperturbed plasma frequency. During this period $2f_{ce} \approx 2.4$ MHz while $f_{pe} \approx 2.05$ MHz. Thus to the accuracy of our measurements the upper hybrid frequency is equal to or slightly less than the second electron cyclotron harmonic. This is the transition point in the first two branches of the dispersion relation for electron Bernstein waves, electrostatic waves traveling perpendicular to the magnetic field.

Barbosa (1976) has examined the dispersion relations for high frequency electrostatic waves and extended the analysis to oblique wave vectors. The electrostatic portion of the dielectric tensor may be written

$$\epsilon_{\parallel} = 1 + \frac{\bar{\omega}_p^2}{b_\perp^2 + b_\parallel^2}\left\{1 - \sum_{n=-\infty}^{\infty} e^{-b_\perp^2} I_n(b_\perp^2)\left(\frac{\bar{\omega}}{\bar{\omega}-n}\right)\cdot\left[1 + \frac{b_\parallel^2}{(\bar{\omega}-n)^2} + \frac{3b_\parallel^4}{(\bar{\omega}-n)^4} + \cdots\right]\right\} \quad \text{(V.13)}$$

where $\mathbf{b} = \frac{\mathbf{k}}{\Omega}\left(\frac{KT}{m}\right)^{1/2}$, $\bar{\omega}_p = \omega_p/\Omega$, $\bar{\omega} = \omega/\Omega$ and Ω, ω_p, T, and m are the electron cyclotron

frequency, plasma frequency, temperature, and mass. Equation V.13 assumes that $|b_{\parallel}| << |\bar{\omega} - n|$ for all n. This condition is necessary to limit the effects of cyclotron damping on the waves of interest. Setting $\epsilon_{\parallel} = 0$, Equation V.13 can be solved to yield

$$b_{\parallel}^2 = \frac{\beta}{2\alpha}\left[1 \pm \left[1 - \frac{4\alpha\gamma}{\beta}\right]^{1/2}\right] \tag{V.14a}$$

where

$$\alpha = 3\bar{\omega}_p^2\bar{\omega}^2 e^{-b_\perp^2}\left[I_0(b_\perp^2)/\bar{\omega}^6 + 2\sum_{n=1}^{\infty} I_n(b_\perp^2)\frac{\bar{\omega}^4 + 10\bar{\omega}^2 n^2 + 5n^4}{(\bar{\omega}^2 - n^2)^5}\right] \tag{V.14b}$$

$$\beta = 1 - \bar{\omega}_p^2\bar{\omega}^2 e^{-b_\perp^2}\left[I_0(b_\perp^2)/\bar{\omega}^4 + 2\sum_{n=1}^{\infty} I_n(b_\perp^2)\frac{\bar{\omega}^2 + 3n^2}{(\bar{\omega}^2 - n^2)^3}\right] \tag{V.14c}$$

$$\gamma = -b_\perp^2 + \bar{\omega}_p^2\left\{-1 + e^{-b_\perp^2}\left[I_0(b_\perp^2) + 2\sum_{n=1}^{\infty} I_n(b_\perp^2)\frac{\bar{\omega}^2}{\bar{\omega}^2 - n^2}\right]\right\} \tag{V.14d}$$

It is convenient to plot the dispersion relation as contour plots in a temperature normalized index of refraction space, $\mathbf{d} = \mathbf{b}/\bar{\omega} = \frac{kc}{\omega}\left[\frac{KT}{mc^2}\right]^{1/2}$. Figure V.11 shows six different sets of constant wave frequency contours in $\mathbf{d}$-space for fixed plasma frequencies in the range of interest. (Note that since Ω is essentially constant we consider changes in $\bar{\omega}_p$ to be due to changes in the plasma density and hence the plasma frequency.) The solid contours in each case correspond to the lower frequency branch of the electron Bernstein mode. The dashed contours correspond to the higher frequency branch. These plots give the contours as a function of positive $d_{\parallel}$ and one component of $d_{\perp}$. Since the dispersion relation is an even function of $d_{\parallel}$ the full three-dimensional iso-frequency surfaces are constructed in the obvious way by mirroring across the $d_{\perp}$ axis and rotating 360° about the $d_{\parallel}$ axis. With this three-dimensional picture in mind we note the following characteristics.

In all cases, "bulbs" form around the $d_{\parallel}$ axes which increase in size with wave frequency. These are just the off-axis generalization of the electrostatic plasma waves which have the dispersion relation

$$\omega^2 = \omega_p^2 + \frac{3}{2}k_{\parallel}^2 v_e^2 \tag{V.15}$$

for $k_\perp = 0$ and where v_e is the electron thermal speed. These bulbs collapse to the plasma frequency when $k_\parallel = 0$.

In addition toroidal surfaces form around the $d_\parallel$ axis when ω_p is less than twice the electron cyclotron frequency. The size of these toroids decreases with increasing wave frequency and they collapse to the lesser of the upper hybrid frequency, $\bar{\omega}_{uh}^2 = \bar{\omega}_p^2 + 1$, or twice the electron gyrofrequency, 2, when $k_\perp = 0$.

The curves of Figure V.11 may also be used to determine the propagation direction of the wave packets. Since the group velocity is just the gradient of ω in **k**-space, wave packets will have propagation directions given by the direction perpendicular to the iso-frequency surface toward larger frequencies. Care must be taken in this and subsequent discussion not to confuse motion in real space with motion in **k**- or **d**-space.

Wave growth

A proper calculation of the amplification of waves in the region of the barium cloud would involve several steps. Having found the dispersion relation which applies strictly only to the thermal background particles, we would then need to calculate the growth rates for waves of different frequencies as a function of the local plasma frequency and **d**. This would be done by using the measured electron distribution function including the energetic electrons which were considered a minor perturbation in solving for the real part of the wave frequency. A spatial model for the barium cloud density along with the dispersion relation and growth rates would then be input into a ray tracing program to compute the convective growth of waves of various frequencies.

Since we have incomplete knowledge of the electron distribution function and since any detailed model for the barium cloud density profile would be somewhat speculative, this procedure does not seem warranted. Fortunately it is also largely unnecessary. Several authors

(Kaufman *et al.*, 1978a; Kaufman *et al.*, 1978b; Lotko and Maggs, 1979; Kaufman, 1980; Lotko and Maggs, 1980; and Maggs and Lotko, 1980) have shown that distributions displaying $\partial f/\partial v_\perp > 0$ are most unstable to upper hybrid waves in the lower ionosphere. Kaufman *et al.* (1978a), Kaufman *et al.* (1978b), and Kaufman (1980) analyzed an observed distribution function with a moderate secondary peak and found it weakly unstable to these waves. The pre-barium distribution function displayed a much more dramatic peak than the one analyzed by Kaufman so it seems safe to assume that an instability was present. Also as it turns out, the most important properties of the barium cloud are its peak density and the fact that it elongates along the magnetic field direction and remains fairly narrow in width.

It is not sufficient to say that the distribution function is unstable. There will in general be a limited region of **d**-space which is unstable. Only those waves which interact more strongly with the electrons in the region of positive slope than with the thermal background will display growth.

In Kaufman's analysis, it is shown that waves may grow when

$$\sum_{n=-\infty}^{\infty} (H_{\perp n} + H_{\parallel n}) > 0 \tag{V.16a}$$

where

$$H_{\perp n} = 2\pi n \Omega \int_0^\infty dv_\perp J_n^2 \frac{\partial f}{\partial v_\perp}\Big|_{v_{\parallel r}} \tag{V.16b}$$

$$H_{\parallel n} = 2\pi k_\parallel \int_0^\infty dv_\perp v_\perp J_n^2 \frac{\partial f}{\partial v_\parallel}\Big|_{v_{\parallel r}} \tag{V.16c}$$

$$k_\parallel v_{\parallel r} = (\bar{\omega} - n)\Omega \tag{V.16d}$$

where the argument of the Bessel functions is $k_\perp v_\perp/\Omega$ and $v_{\parallel r}$ is the velocity of a resonant electron. The process of finding unstable wave modes amounts to picking a wave with a frequency $\bar{\omega}$, wave vector components, and an n such that the region of positive slope in the distribution function lies at $v_\parallel = v_{\parallel r}$ and at the value of $v_\perp$ which maximizes J_n^2. In addition other terms in the infinite sum of Equation V.16a which will generally be negative must be kept

small. We are generally interested in the strong emissions at the upper hybrid frequency. For these waves we are forced to choose $n = 2$.

The main contribution to the growth of these waves comes from the perpendicular peak and specifically $H_{\perp 2}$. In order to decrease damping from the $H_{\parallel}$ terms we must keep $k_{\parallel}$ small. Looking back at Equation V.13, recall that the approximation $b_{\parallel} << |\bar{\omega} - n|$ was made. For $b_{\parallel}$ violating this condition not only is cyclotron damping important, but the dispersion relation itself may be in error. In any case, waves with large $b_{\parallel}$ or $d_{\parallel}$ are not expected to grow and we can limit our attention to waves close to the $b_{\perp}$ or $d_{\perp}$ axis. For our purposes we will consider a wave to be strongly damped by the thermal electrons if $d_{\parallel} > \frac{|\bar{\omega} - n|}{3\bar{\omega}}$. Equation V.16d also limits the range of $k_{\parallel}$ over which we may expect growth. The unstable perpendicular peak is only observed at values of $v_{\parallel} \geq -6\times10^{8}$ cm/s and by extrapolation only exists up to a maximum of $v_{\parallel} \approx 2\times10^{9}$ cm/s. The most positive values of $\frac{df}{dv_{\perp}}$ occur for $|v_{\parallel}| \leq 6\times10^{8}$ cm/s and thus by Equation V.16d we expect growth only for values of $|k_{\parallel}| \geq 1.3|\bar{\omega} - n|$ m^{-1} where we have used $\Omega = 7.5\times10^{6}$ s^{-1} For an electron temperature of .2 eV this translates to $|d_{\parallel}| \geq \frac{1}{30}\frac{|\bar{\omega} - n|}{\bar{\omega}}$.

Thus the two restrictions on $d_{\parallel}$ are compatible and yield the region

$$\frac{1}{30}\frac{|\bar{\omega} - n|}{\bar{\omega}} < |d_{\parallel}| < \frac{1}{3}\frac{|\bar{\omega} - n|}{\bar{\omega}} \qquad \text{(V.17)}$$

in which wave growth may be expected. For $d_{\parallel}$ too small the waves interact with portions of the distribution function at large $v_{\parallel}$ where there are few particles and no secondary peak. For $d_{\parallel}$ too large, interaction with the thermal background becomes dominant. This results in strong damping. Another way of looking at this restriction is that large $d_{\parallel}$ implies small $v_{\parallel}$, and a cut across the distribution function at small enough $v_{\parallel}$ will include the region of highly negative $\frac{df}{dv_{\perp}}$ associated with the thermal electrons.

Finally we need to consider restrictions on $d_\perp$. In order to maximize $H_{\perp 2}$ we need to pick $k_\perp$ which maximizes $J_2(k_\perp v_\perp/\Omega)$ at $v_\perp \approx 2\times10^9$ cm/s $\pm$ 4×10^8 cm/s where the region of positive $\frac{df}{dv_\perp}$ lies. Since J_2 has a maximum when the argument is 3 this restriction implies $k_\perp \approx 1.1 \pm .2$ m^{-1} or,

$$d_\perp = .014 \pm .003 \tag{V.18}$$

For large $d_\perp$, J_2 peaks at small $v_\perp$ where $\frac{df}{dv_\perp}$ is highly negative. These waves are likely to be damped. At small $d_\perp$, J_2 peaks at large $v_\perp$ and little or no wave growth is expected.

Wave packet trapping

We now would like to qualitatively analyze the convection and growth or decay of specific wave packets as they interact with the barium produced plasma density enhancement. To do this we consider the dispersion relation of a given wave frequency as the plasma frequency (density) varies. In Figure V.12 contours of constant plasma frequency are plotted in d-space for a given wave frequency. Lines have been drawn indicating the regions of strong damping, weak damping, and growth as given by Equation V.17 and Equation V.18.

Once again the bulb shaped contours form around the $d_\parallel$ axis for all values of $\bar{\omega}$, but now they decrease in size with increasing plasma frequency collapsing to the wave frequency when $k_\parallel = 0$. Also the toroidal surfaces are present for wave frequencies smaller than twice the electron cyclotron frequency, but now they increase in size with increasing plasma frequency and when $k_\perp = 0$ they collapse to the plasma frequency that makes $\bar{\omega} = \bar{\omega}_{uh}$. Another interesting feature of these plots is that when $\bar{\omega} = 2$ all the contours collapse to $k_\perp = k_\parallel = 0$.

Consider a wave packet of a given frequency, $\bar{\omega}$, moving through a region of space in which the plasma frequency, $\bar{\omega}_p$, varies from $\bar{\omega}_{p_{min}}$ to $\bar{\omega}_{p_{max}}$. Due to refractive effects we expect that in time the wave will tend to visit every region of d-space available to it. Looking at Fig-

ure V.12 we see that if $\bar{\omega} > 2$ then, except for a small range of plasma frequencies just above the wave frequency, the wave will have access to large values of $d_{\|}$ where it will be strongly damped. Thus we do not expect to see any waves at other than the plasma frequency above 2Ω. This is the situation observed on this flight. These waves are driven primarily by a secondary peak at low pitch angles. Since these particles were not measured we will not speculate further on the details of their occurrence except to note that the observation of plasma waves might be expected to coincide with pockets of diminished plasma density. An examination of the dispersion relation for waves near the plasma frequency shows that such pockets will be able to trap waves near the minimum plasma frequency spatially and confine them to small values of $d_{\|}$. A similar mechanism will be shown to hold for upper hybrid waves except that the requirement in that case is that there be a small plasma density enhancement.

If $\bar{\omega} < 2$ there is a range of $\bar{\omega}_p$ from $\bar{\omega}_p = \sqrt{\bar{\omega}^2 - 1}$ up to some $\bar{\omega}_p < 2$ in which $d_{\|}$ is bounded. These are the toroidal contours. Notice that when $\bar{\omega}_p = \sqrt{\bar{\omega}^2 - 1}$ then $\bar{\omega} = \bar{\omega}_{uh}$. Notice also that these waves cannot exist in regions where $\bar{\omega}_p < \sqrt{\bar{\omega}^2 - 1}$. There is a cutoff at this value of $\bar{\omega}_p$ and any wave propagating toward less dense regions will be reflected at this point.

Now consider a simple model of the barium cloud. It is a cigar shaped plasma density enhancement extended along the magnetic field lines. In the case of this flight the ambient plasma frequency was just slightly less than $\sqrt{3}\Omega$. This is the plasma frequency which makes $\omega_{uh} = 2\Omega$. The plasma frequency within the cloud rose to well above 2Ω and decayed as the cloud expanded to the ambient value after about 40 seconds. Since the ambient plasma frequency is less than $\sqrt{3}\Omega$, waves at frequencies less than 2Ω will have access to all portions of d-space within the curve corresponding to $\bar{\omega}_{p_{max}}$. When $\bar{\omega}_{p_{max}}$ is above 2 these waves will often take on large values of $d_{\|}$ and thus be strongly damped. Thus no waves should be observed until $\bar{\omega}_{p_{max}}$ decays to less than 2. In fact waves are observed slightly prior to this according to

the calculated value of ω_p but the rule appears to be obeyed within the uncertainty of the measurements.

As $\bar{\omega}_{p_{max}}$ continues to decrease the waves are confined to smaller and smaller values of $d_{\parallel}$ and the possibility for growth increases. Figure V.13 shows detailed dispersion relations for $\bar{\omega} = 1.97$, 1.98, and1.99. For $\bar{\omega} = 1.97$, Figure V.13a shows that most waves having access to the region of growth are damped by virtue of the large values of $d_{\perp}$ that they have access to. For $\bar{\omega} = 1.98$, Figure V.13b shows clearly that if $\bar{\omega}_{p_{max}} < 1.74$ the wave is confined to regions of growth or weak damping at worst. For $\bar{\omega} = 1.99$, Figure V.13c shows that all waves having access to the growth region at this frequency are damped by virtue of the large values of $d_{\parallel}$ which they attain at smaller values of $d_{\perp}$. From this analysis then, we expect waves at $\bar{\omega} = 1.98$ to be the most likely candidates for convective growth. Notice that $\bar{\omega}_{p_{min}}$ is not important for this consideration. In this case the curves collapse to $\mathbf{d} = 0$ for $\bar{\omega}_p = \sqrt{\bar{\omega}^2 - 1} = 1.709$. Even if $\bar{\omega}_{p_{min}}$ is greater than this the wave is still confined to favorable values of $\mathbf{d}$. To understand the importance of $\bar{\omega}_{p_{min}}$ we must consider the spatial propagation of these wave packets. If $\bar{\omega}_{p_{min}} > \sqrt{\bar{\omega}^2 - 1}$ the wave packets are unbounded spatially and will escape the density enhancement and thus the auroral beam. If $\bar{\omega}_{p_{min}} < \sqrt{\bar{\omega}^2 - 1}$ the wave packets are trapped within the density enhancement due to the reflection at the cutoff point. As a result they interact with the beam for a prolonged period and may achieve substantial growth. The frequencies that are observed correspond to normal modes of the ambient plasma since it is the cutoff at the borders of the plasma density enhancement that traps the waves.

Thus the most favorable conditions for growth of upper hybrid waves can be summarized as follows:

1 The electron distribution function displays a highly positive $\frac{df}{dv_{\perp}}$ at perpendicular pitch angles.

2 The ambient plasma frequency is just under $\sqrt{3}\Omega$.

3 A moderate plasma density enhancement yielding $\bar{\omega}_{p_{max}}$ just over $\sqrt{3}\Omega$ exists within the auroral beam. (Extreme enhancements tend to yield damping due to the larger values of $d_{\parallel}$ that are allowed.)

These are precisely the conditions which were observed during this flight and thus the large amplitude upper hybrid waves result as a natural consequence of the fortuitous conditions. These waves have a wavelength of about 6 m determined by the value of $v_{\perp}$ at which the electron distribution peaks.

Wave-particle interactions

The observed changes in the electron distribution function are now naturally ascribed to the wave-particle interaction produced by the catalytic action of the cloud. Presumably at high altitudes the electron distribution function retains its pre-barium peak. As the electrons enter the cloud where the upper hybrid wave packets are trapped, they interact with these waves. The waves liberate the free energy represented by the secondary peak and by the time the electrons are observed at the payload, the peak has been eroded into the plateau characteristic of the post-barium distribution function. The high amplitude waves were observed for about 20 seconds but the distribution function was changed for virtually the remainder of the flight. Presumably, then, wave activity continued at higher altitudes for an extended period.

An attempt was made to calculate the rate at which energy was lost from the electrons by assuming the pre-barium distribution to be extant above the cle ' The results were that energy was conserved to the accuracy of the very rough calculations. Thus it appears that the waves extract little power from the beam but exert a large influence by redistributing the energy. Notice that the peak energy of the auroral beam was growing during the development of the barium cloud and thus such a calculation based on the assumed nature of the high alti-

tude distribution function is highly uncertain.

The enhanced fluxes of low energy electrons deserves some attention at this point. Since the largest of these events occurs simultaneously with the highest amplitude upper hybrid waves, the two would seem to be associated in some way. The existence of other bursts during the early stages of the barium cloud and at times not correlated with wave observations may be further evidence that the waves are present elsewhere producing the low energy electrons which then travel to the observation point. These electrons have velocities of about 3×10^8 cm/s and will thus interact strongly with waves near the second electron cyclotron harmonic when $k_\perp v_\perp/\Omega \simeq 3$, which once again maximizes J_2. This implies a $k_\perp$ of about 8 m which is about the value obtained by the 2.2 MHz daughter wave of the upper hybrid waves as discussed below. Enhanced fluxes are not produced by a resonant interaction. Electrons must be accelerated from a higher density, lower energy portion of phase space. This would mean that the interaction would have to begin at lower energies, perhaps at higher altitudes where the dispersion relation is different. After resonantly trapping a group of low energy electrons, the resonance condition might shift to higher energies as the electrons move, accelerating the electrons.

Figure V.14 is a schematic representation of the wave-particle interaction taking place within the barium cloud. The upper hybrid wave packets are trapped within the barium cloud by the cutoff which exists in the dispersion relation for $\bar{\omega}_p$ just under $\sqrt{3}$. The waves modify the distribution function of the precipitating electrons from its form above the cloud to its form at the point of observation.

Wave-wave interactions

Now we turn our attention to the 200 and 400 kHz sidebands observed near the peak in the growth of the upper hybrid oscillations. Due to the simultaneous appearance of oscillations

at the difference frequencies these are interpreted as the product of a parametric decay process pumped by the high amplitude upper hybrid waves. Such a three wave interaction requires frequency and wave vector matching. That is,

$$\omega_0 = \omega_1 + \omega_2 \tag{V.19}$$

$$\mathbf{k}_0 = \mathbf{k}_1 + \mathbf{k}_2 \tag{V.20}$$

First we will consider the requirements of frequency matching. Figure IV.8 shows that Equation V.19 is satisfied for two cases,

$$\omega_{uh} \rightarrow \omega_{200A} + \omega_{2.2M} \tag{V.21a}$$

and

$$\omega_{uh} \rightarrow \omega_{400A} + \omega_{2.0M} \tag{V.21b}$$

where the subscripts refer to the observed frequencies of the daughter waves in Hz. The production of the sidebands above ω_{uh} is probably due to a recoupling of the low frequency waves to ω_{uh} giving the processes,

$$\omega_{uh} + \omega_{200A} \rightarrow \omega_{2.6M} \tag{V.22a}$$

and

$$\omega_{uh} + \omega_{400A} \rightarrow \omega_{2.8M} \tag{V.22b}$$

In addition the several small oscillations that are observed at higher frequencies may also be generated in some manner by couplings between the upper hybrid oscillations and its high frequency daughters. The frequency of the largest of these emissions is $2\omega_{uh} = 4\Omega$. This may be due to a coupling of the upper hybrid wave to itself.

In order to limit the scope of this analysis we will confine ourselves to the consideration of the process indicated in Equation V.21a. The next task is to find modes which exhibit the proper wave vector matching properties. We have no way of knowing for sure what all of the participating modes are or even whether they are electrostatic or electromagnetic. Assuming that all the modes are electrostatic, which seems more likely due to coupling considerations, the low frequency wave would be a whistler on the resonance cone and the high frequency

daughter would be another electron Bernstein wave with an oblique k. The whistler has a constant $k_{\parallel}/k_{\perp}$. The Bernstein wave has constant $k_{\parallel}/k_{\perp}$ for small k and becomes constant k and more oblique as k increases. In our specific case the 200 kHz whistler has a propagation direction $\tan^{-1}(k_{\parallel}/k_{\perp}) \approx 12°$. The 2.2 MHz Bernstein wave has a propagation direction $\tan^{-1}(k_{\parallel}/k_{\perp}) \approx 55°$ for $k \leq 5m^{-1}$ and eventually attains $k \approx 9m^{-1}$ for propagation directions within 45° of perpendicular to **B**.

As a result of the constant $k_{\parallel}/k_{\perp}$ behavior of the low frequency whistler there are a multitude of possible k-matching schemes. Four possibilities are sketched in Figure V.15. Two of these use the constant k portion of the Bernstein dispersion relation and have $k_1 \approx k_2 >> k_0$. The other two use the constant $k_{\parallel}/k_{\perp}$ portion and have $k_0 \approx k_1 \approx k_2$. In all four cases the pump wave is assumed to be exactly oblique. This is inconsequential in the first two cases since k_0 is small, but in the last two cases deviations from perfect obliqueness will affect, but not eliminate, the matching. These four cases share the feature that **B** is included in the plane of the matching scheme. This need not be the case however it is probable that the coupling is stronger this way due to polarization considerations. It is also possible to allow the pump wave to have a propagation direction similar to the whistler in which case an electromagnetic wave with small k might fit the requirements for the high frequency daughter.

Why 200 kHz?

At least one important question remains unanswered in the preceding analysis. What factors result in the selection of 200 kHz as the preferred difference frequency? The wave vector matching schemes presented here could apply to any frequency up to a few hundred kHz.

There are several possible answers to this question. First, given an instability which is equally likely to proceed in a number of directions, the slightest push in one of these may be all it takes to make the decision. Once a given decay mode is chosen it is likely to be strongly pre-

ferred due to a self-reinforcing stimulation. There is a radio transmitter at Lulea, Sweden, a distance of 300 km from Kiruna, which operates at a frequency of 200 kHz. While radiation from this source at this frequency would be expected to be strongly shielded from the upper ionosphere, it may have played a role in determining the decay products.

Another possibility has to do with the generation of a standing wave resonance within the barium cloud density enhancement. Since the waves were trapped by the cloud, it is possible that certain k's might have been selected by virtue of their resonance properties. This seems somewhat unlikely however due to the short wavelengths (1-10 m) of the daughter waves compared with the size of the cloud (> 10 km in any dimension).

A final interesting possibility is related to the behavior of the dispersion relation for waves at the upper and lower 200 kHz sidebands of the pump. As suggested by Figure V.11, these waves, having $\bar{\omega}$'s of 1.83 and 2.17, when propagating in a region where $\bar{\omega}_p \approx \sqrt{3}$, have very similar k's for all oblique propagation directions. Perhaps this fact, plus the common low frequency mode which couples both waves to the upper hybrid pump provides extra stimulation for the selection of these frequencies.

The multiple sideband structure may be related to this mechanism as well. The initial decay into the 200 kHz and 2.2 Mhz daughters is reinforced by the recoupling of the 200 kHz wave to the pump forming a 2.6 MHz daughter which shares wave vectors with the 2.2 MHz wave. The resulting 400 kHz difference stimulates the growth of a low frequency daughter at this frequency which couples with a 2.0 MHz Bernstein mode extracting more power from the pump and so on. Thus growth of waves in such a harmonic series is self-reinforcing due to the multiple couplings which are possible in such a scheme and the process goes on until saturation at the point where the parametric decay matches the particle stimulated growth of the pump.

VI. CONCLUSIONS

An Aries sounding rocket was launched into a quiet auroral arc and returned comprehensive data on precipitating particles, fields, and plasma density within the arc. Two striking features of the data have been analyzed here. The first, the electric field-particle energy anticorrelation, is a large scale feature of the quiet arc. The second, the wave-particle interaction, is a small scale phenomenon artificially induced by the barium shaped charge experiment.

The anticorrelation observed between the D.C. electric field and the peak energy of the auroral beam appears to be a result of the modulation of the ionospheric conductivities due to the ionization produced by the energetic precipitating electrons. The ionospheric conductivities increase as the peak electron energy increases due to generally increased number fluxes, larger ionization per incident electron, and enhanced penetration to lower altitudes where the collision frequency is larger. With the assumption of a negligible field-aligned divergence of the ionospheric current system, the electric field is required to vary in some sort of inverse fashion. The picture is complicated by the necessity to consider Hall and Pedersen conductivities, neutral winds, ionization flow velocities, and arc motion. A computer simulation was developed to properly treat the problem and the results show fair agreement with the data. As a result the nearly exact inverse relationship observed on this flight appears in retrospect to have been fortuitous, but the inferred mechanism is more than likely operative in most quiet arcs. An application of the simulation routines to other rocket data obtained in quiet arcs would be helpful in evaluating the validity of the model.

The wave observations appear to be due to the catalytic action of the barium plasma density enhancement produced within the energetic electron precipitation region by the barium

experiment. The precipitating electron distribution function is unstable to the growth of perpendicularly propagating high frequency electrostatic waves. In the unperturbed case this instability does not lead to large wave growth because of the limited spatial extent of the arc. Waves move out of the arc before growing to detectable amplitudes. In the presence of a plasma density enhancement the situation changes. Waves may exist within the enhancement that cannot exist outside. These waves are refractively trapped and interact with the electrons on much larger time scales. For the ambient plasma conditions observed on this flight, the waves trapped by the barium cloud were just those to which the electron distribution function was most unstable - the upper hybrid mode. These waves then parametrically decayed to a multitude of daughter modes producing the rich spectrum observed. As a result of the enhanced wave-particle interaction the free energy represented by the secondary peak was liberated and the electron distribution function was stabilized.

REFERENCES

Anderson, K.A., H.K. Harris, and R.J. Paoli, Energetic electron fluxes in and beyond the earth's outer magnetosphere, *J. Geophys. Res.*, **70**, 1039, 1965.

Barbosa, D.D., Electrostatic mode coupling at $2\omega_{UH}$: A generation mechanism for auroral kilometric radiation, Ph.D. Thesis, University of California, Los Angeles, 1976.

Bostrom, R., A model of the auroral electrojets, *J. Geophys. Res.*, **69**, 4983, 1964.

Brekke, A., J.R. Doupnik, and P.M. Banks, Incoherent scatter measurements of E region conductivities and currents in the auroral zone, *J. Geophys. Res.*, **79**, 3773, 1974.

Campbell, R.D. and R.P.Lin, Energy loss of low energy nuclei in silicon surface barrier detectors, *Rev. Sci. Instr.*, **44**, 1510, 1973.

Carlson, C.W., Rocket measurements of auroral zone low energy charged particles, Ph.D. Thesis, University of California, Berkeley, 1974.

Chase, L.M., Energy spectra of auroral zone particles, Ph.D. Thesis, University of California, Berkeley, 1969.

De La Beaujardiere, O., R. Vondrak, and M. Baron, Radar observations of electric fields and currents associated with auroral arcs, *J. Geophys. Res.*, **82**, 5051, 1977.

Edwards, T., D.A. Bryant, M.J. Smith, U. Fahleson, C-G Falthammar, and A. Pedersen, Electric fields and energetic particle precipitation in an auroral arc, Paper presented at the Summer Advanced Study School Magnetospheric Particles and Fields, Graz, 1975.

Evans, D.S., Precipitating electron fluxes formed by a magnetic field aligned potential difference, *J. Geophys. Res.*, **79**, 2853, 1974.

Evans, D.S., N.C. Maynard, J. Troim, T. Jacobsen, and A. Egeland, Auroral vector electric field and particle comparisons 2. Electrodynamics of an arc, *J. Geophys. Res.*, **82**, 2235, 1977.

Fridman, M. and J. Lemaire, Relationship between auroral electrons fluxes and field aligned electric potential difference, *J. Geophys. Res.*, **85**, 664, 1980.

Goertz, C.K., and R.W. Boswell, Magnetosphere-ionosphere coupling, *J. Geophys. Res.*, **84**, 7239, 1979.

Hays, P.B., J.W. Merriwether, and R.G. Roble, Nighttime thermospheric winds at high latitudes, *J. Geophys. Res.*, **84**, 1905, 1979.

Jones, R.A. and M.H. Rees, Time dependent studies of the aurora - I. Ion density and composition, *Planet. Space Sci.*, **21**, 537, 1973.

Kato, S., Theory of movement of irregularities in the upper atmosphere, *Planet. Space Sci.*, **11**, 1379, 1963.

Kaufman, R.L., D.N Walker, and R.L. Arnoldy, Acceleration of auroral electrons in parallel electric fields, *J. Geophys. Res.*, **81**, 1673, 1976

Kaufman, R.L., P.B. Dusenbery, B.J. Thomas, and R.L. Arnoldy, Auroral electron distribution function, *J. Geophys. Res.*, **83**, 586, 1978a.

Kaufman, R.L., P.B. Dusenbery, and B.J. Thomas, Stability of the auroral plasma: Parallel and perpendicular propagation of electrostatic waves, *J. Geophys. Res.*, **83**, 5663, 1978b.

Kaufman, R.L., Electrostatic wave growth: Secondary peaks in a measured auroral electron distribution function, *J. Geophys. Res.*, **85**, 1713, 1980.

Koons, H.C., and M.B. Pongratz, Ion cyclotron wave generated by an ionospheric barium injection, *J. Geophys. Res.*, **84**, 533, 1979.

Lemaire, J., Impulsive penetration of filamentary plasma elements into the magnetospheres of the Earth and Jupiter, *Planet. Space Sci.*, **25**, 887, 1977.

Lemaire, J. and M. Roth, Penetration of solar wind plasma elements into the magnetosphere, *J. Atmos. Terr. Phys.*, **40**, 331, 1978.

Lin, R.P., A charge and mass analyzer for energetic, < 5 to 500 kev solar, interplanetary, and magnetospheric ions, U.C. Berkeley Space Sciences Laboratory Report No. 555/75, October, 1974.

Lochte-Holtgreven, W. (ed.), *Plasma Diagnostics*, North-Holland Publishing Company, pp 668-776, 1968.

Lotko, W., and J.E. Maggs, Damping of electrostatic noise by warm auroral electrons, *Planet. Space Sci.*, **27**, 1491, 1979.

Lotko, W., and J.E. Maggs, $\partial F/\partial v_\perp > 0$ as a source of free energy in the auroral beam, submitted to *J. Geophys. Res.*, 1980.

Lynch, J., D. Pulliam, R. Leach, and F. Scherb, The charge spectrum of positive ions in a hydrogen aurora, *J. Geophys. Res.*, **81**, 1264, 1976.

Lyons, L R., D.S. Evans, and R. Lundin, An observed relation between magnetic field aligned electric fields and downward electron fluxes in the vicinity of auroral forms, *J. Geophys. Res.*, **84**, 457, 1979.

Lyons, L R., Generation of large-scale regions of auroral currents, electric potentials, and precipitation by the divergence of the convection electric field, *J. Geophys. Res.*, **85**, 17, 1980.

Maggs, J E., Coherent generation of VLF hiss, *J. Geophys. Res.*, **81**, 1707, 1976.

Maggs, J E., and T N. Davis, Measurements of the thicknesses of auroral structures, *Planet. Space Sci.*, **16**, 205, 1968.

Maggs, J.E., Electrostatic noise generated by the auroral electron beam, *J. Geophys. Res.*, **83**, 3173, 1978.

Maggs, J E., and W. Lotko, Altitude dependent model of the auroral beam, submitted to *J. Geophys. Res.*, 1980.

Mallinckrodt, A J. and C.W. Carlson, Relations between transverse electric fields and field-aligned currents, *J. Geophys. Res.*, **83**, 1426, 1978.

Mozer, F.S., C.A. Cattell, M.K. Hudson, R.L. Lysak, M. Temerin, and R.B. Torbert, Satellite measurements and theories of low altitude auroral particle acceleration, *Space Sci. Rev.*, in press 1980.

Paschman, G. Plasma structure of the magnetopause and boundary layer, in *Magnetospheric Boundary Layers*, proceedings of a Sydney Chapman Conference, Alpbach, published by European Space Agency, June, 1979.

Potter, D W. and R.D. Campbell, Pulse height defect and window energy loss of low energy ions in surface barrier detectors, *Nuc. Inst. and Meth.*, **153**, 525, 1978.

Rees, M H., Auroral ionization and excitation by incident energetic electrons, *Planet. Space Sci.*, **11**, 1209, 1963.

Roble, R G., R E. Dickinson, and E.C. Ridley, Thermospheric response to the November 8-9, 1969, magnetic disturbances, *J. Geophys. Res.*, **84**, 4207, 1979.

Roederer, J G., On the adiabatic motion of energetic particles in a model magnetosphere, *J. Geophys. Res.*, **72**, 981, 1967.

Roederer, J.G., *Dynamics of geomagnetically trapped radiation*, Springer-Verlag, 1970.

Stenbaek-Nielsen, H.C., and T.J. Hallinan, Pulsating auroras: Evidence for noncollisional thermalization of precipitating electrons, *J. Geophys. Res.*, **84**, 3257, 1979.

Stone, E.C., The physical significance of L, B_0, and R_0 to geomagnetically trapped particles, *J. Geophys. Res.*, **68**, 4157, 1963.

Van Allen, J.A., G.H. Ludwig, E.C. Ray, and C.E. McIlwain, Observation of high intensity radiation by satellites 1958α and γ, *Jet Propulsion*, **28**, 588, 1958.

Whalen, B A., and P.W. Daly, Do field-aligned auroral particle distributions imply acceleration by quasi-static parallel electric fields?, *J. Geophys. Res.*, **84**, 4175, 1979.

TABLE 1: EJECTABLE PROBE INSTRUMENTATION

TYPE	ORIENTATION TO SPIN AXIS	RANGE	SENSITIVITY RESOLUTION	SAMPLE TIME
Low Energy Electrons	0°, 30°, and 180°	6 to 500 eV 128 steps	5.7×10^{-3} cm^{2}ster eV ΔE = 30 eV	.004 s 1.024 s/sweep
High Energy Electrons	0°	350 eV to 30 keV 128 steps	1.8×10^{-3} cm^{2}ster(E) $\Delta E/E$ = .09	.004 s 1.024 s/sweep
High Energy Ions	0°	500(Z) eV to 40(Z) keV 128 steps	1.1×10^{-3} cm^{2}ster(E) $\Delta E/E$ = .06	.004 s 1.024 s/sweep
Ion Composition	0°	500(Z) eV to 40(Z) keV	1.1×10^{-3} cm^{2}ster(E)	.0005 s/sample
D.C. Electric Field	0°, 90°	0 to 100 mV/m	1 mV/m	.002 s
High Gain "D.C." Electric Field	0°, 90°	0 to .1 mV/m 3 to 128 Hz		.001 s
Low Frequency Spectrum Analyzers	0°, 90°	0 to 50 kHz 512 steps	300 Hz	.004 s 2.048 s/sweep
High Frequency Spectrum Analyzers	0°, 90°	0 to 5 MHz 512 steps	30 kHz	.001 s .512 s/sweep
Magnetic Field	0°, 90°	± .5 Gauss	30 γ	.004 s
Density		10^3 to 10^6 cm^{-3}		.001 s
A.C. Density		0 to 1 kHz	$\Delta n/n > .01$	.0005 s
Temperature		500 to 4000 °K		.004 s
A.C. Temperature		0 to 100 Hz	$\Delta T/T > .01$	.002 s

TABLE 2: RECORD 1 DATA

DATA	FUNCTION	UNITS	ROUTINE	TYPE
IDVPRF	Input file ID		SIMSPC	Int
IDIZEX	I or E_x profile ID		SIMCUR	Int
IDFNAL	Output file ID		SIMCUR	Int
NEBINS	# of energy bins		SIMSPC	Int
EMIN	Lowest energy	eV	SIMSPC	Real
EMAX	Highest energy	eV	SIMSPC	Real
TSRCE	Source temperature	eV	SIMSPC	Real
DSRCE	Source density	cm^{-3}	SIMSPC	Real
BRATIO	Magnetic field ratio		SIMSPC	Real
THETAD	Angle of B	Degrees	SIMPRD	Real
VNEUT	Neutral wind speed	m/s	SIMDNS	Real
PHID	Angle between v_n and B_0	Degrees	SIMDNS	Real
DX	Latitudinal step size	km	SIMDNS	Real
NXSTPS	# of steps		SIMSPC	Int
EY	Longitudinal comp. of E	mV/m	SIMDNS	Real
BMAG	B at earth's surface	Gauss	SIMDNS	Real
LETRUE	E_x or I_x indicator		SIMCUR	Log
LCURNT	I profile indicator		SIMCUR	Log
LEX	E_x profile indicator		SIMCUR	Log
ELTRJT	Electrojet current	A	SIMCUR	Real
VPOWER	Particle power law		SIMSPC	Real

TABLE 3: RECORD 3 TO END DATA			
DATA	FUNCTION	UNITS	ROUTINE
V0	Accelerating potential	V	SIMSPC
EX	Latitudinal comp of E	mV/m	SIMCUR
CX	Latitudinal height integrated current	A/m	SIMCUR
CY	Longitudinal height integrated current	A/m	SIMCUR
PED	Height integrated Pedersen conductivity	Mho	SIMCUR
HALL	Height integrated Hall conductivity	Mho	SIMCUR
EFLUX	Particle power dissipation	$erg/cm^2\ s$	SIMSPC
EJOULE	Field power dissipation	$erg/cm^2\ s$	SIMCUR
CURNT	Field aligned current at 250 km	$\mu A/m^2$	SIMSPC
Q(171)	Production rate profile	$cm^{-3}s^{-1}$	SIMPRD
DENS(171)	Electron density profile	cm^{-3}	SIMDNS
CDX(171)	Latitudinal current density profile	$\mu A/m^2$	SIMCUR
CDY(171)	Longitudinal current density profile	$\mu A/m^2$	SIMCUR
CDZ(171)	Vertical current density profile	$\mu A/m^2$	SIMCUR
SIGMAP(171)	Pedersen conductivity profile	mho/m	SIMCND
SIGMAH(171)	Hall conductivity profile	mho/m	SIMCND
TF(100)	Downward differential electron flux	$cm^{-2}s^{-1}eV^{-1}$	SIMSPC

FIGURE CAPTIONS

Figure I.1. A model of the magnetosphere.

Figure II.1. A sketch of an ejectable probe and its instrumentation. (1-6) Electric field and plasma booms. (a) ESA view direction. (b-d) RPA view directions. (e) "Belly-band" antenna. (f) Magnetometer. (g) Sun sensor.

Figure II.2. Particle detectors, (a) An RPA, (b) an ESA.

Figure III.1. The trajectory of Porcupine 2 including the value of the magnetic coordinate - L.

Figure III.2. Magnetic projection of the trajectory to 110 km.

Figure IV.1. Electron and plasma wave spectrograms.

Figure IV.2. The equatorward, westward, and total DC electric field. The large disturbance at $t = 373$ seconds is due to the detonation of the barium shaped charge experiment.

Figure IV.3. The magnetic projection to 110 km of the observed electric field. The vectors are labeled according to whether they were observed on the upward or downward leg of the flight.

Figure IV.4. A fifty second average of the ion fluxes observed between $t = 250$ and 300 seconds. This spectrum is typical of that observed throughout the flight.

Figure IV.5. A comparison of the inverse total DC electric field with the peak energy of the precipitating electrons.

Figure IV.6. Sweeps of the high energy electron detector from before and after the barium detonation.

Figure IV.7. Polar plot of the pre- and post-barium distribution function.

Figure IV.8. Twelve successive sweeps of the high frequency spectrum analyzer at the time of the high amplitude wave observations.

Figure IV.9. A detailed plot of the seventh spectrum analyzer sweep of the previous figure.

Figure V.1. (a and b) The relationship between the ionospheric electric field and the peak electron energy for a model in which the ionospheric potential configuration is calculated by adding a potential inferred from the peak electron energy to a simple assumed magnetospheric potential configuration. (c) The required magnetospheric potential configuration to produce an inverse relationship between the peak energy and the ionospheric field.

Figure V.2. Coordinate system for the auroral simulation.

Figure V.3. The D.C. electric field rotated 30° from north toward west into the coordinates of the arc.

Figure V.4. Height integrated conductivities obtained for simplest case.

Figure V.5 Relative velocities of neutral wind, arc, and geographic frames.

Figure V.6 The E_x profile obtained from the simplest case compared with the observed profile.

Figure V.7. Height integrated conductivities in the case $u_n = 0$ and $v_n = 0.19\text{mV/m}/B$.

Figure V.8 Height integrated conductivities for various values of u_n.

Figure V.9 The E_x profile resulting from various choices for u_n and v_n.

Figure V.10 Height integrated conductivities as a function of peak energy of the auroral beam for three different values of the source temperature.

Figure V.11 Constant wave frequency dispersion contours for various fixed values of $\bar{\omega}_p$. (a) 1.7 (b) $\sqrt{3}$ (c) 1.8 (d) 1.9 (e) 2.0 (f) 2.1. Curve labels are $\bar{\omega}$.

Figure V.12 Constant plasma frequency dispersion contours for various fixed values of $\bar{\omega}$. (a) 1.8 (b) 1.9 (c) 1.95 (d) 2.05 (e) 2.1 (f) 2.2. Curve labels are $\bar{\omega}_p$.

Figure V.13. Details of the dispersion relation for $\bar{\omega}$ equal to (a) 1.97 (b) 1.98 (c) 1.99.

Figure V.14. Diagram of barium cloud indicating proposed interaction of trapped waves with the precipitating auroral electrons.

Figure V.15. Four simple wave vector matching schemes for the parametric decay process.

Figure VII.1. A flowchart for SIMSPC.

Figure VII.2 A flowchart for SIMPRD.

Figure VII.3. A flowchart for SIMDNS.

Figure VII.4. A flowchart for SIMCND.

Figure VII.5. A flowchart for SIMCUR. (a) General (b) Detail of the calculational loop.

Figure VII.6. The differential electron flux (TF) at three positions within the model arc.

Figure VII.7. Simulated arc data as a function of latitudinal distance. (a) The input field-aligned potential drop. (b) The field-aligned current carried by the precipitating electrons. (c) The height integrated conductivities. (d) The equatorward component of the electric field. (e)The two components of the height integrated current. (f)The particle power input and Joule heating produced in the ionosphere.

Figure VII.8. The projection of the x and z components of the current density onto the x-z plane.

Figure VII.9. The projection of the x and z components of the current density onto the x-z plane. Downward components correspond to positive j_z.

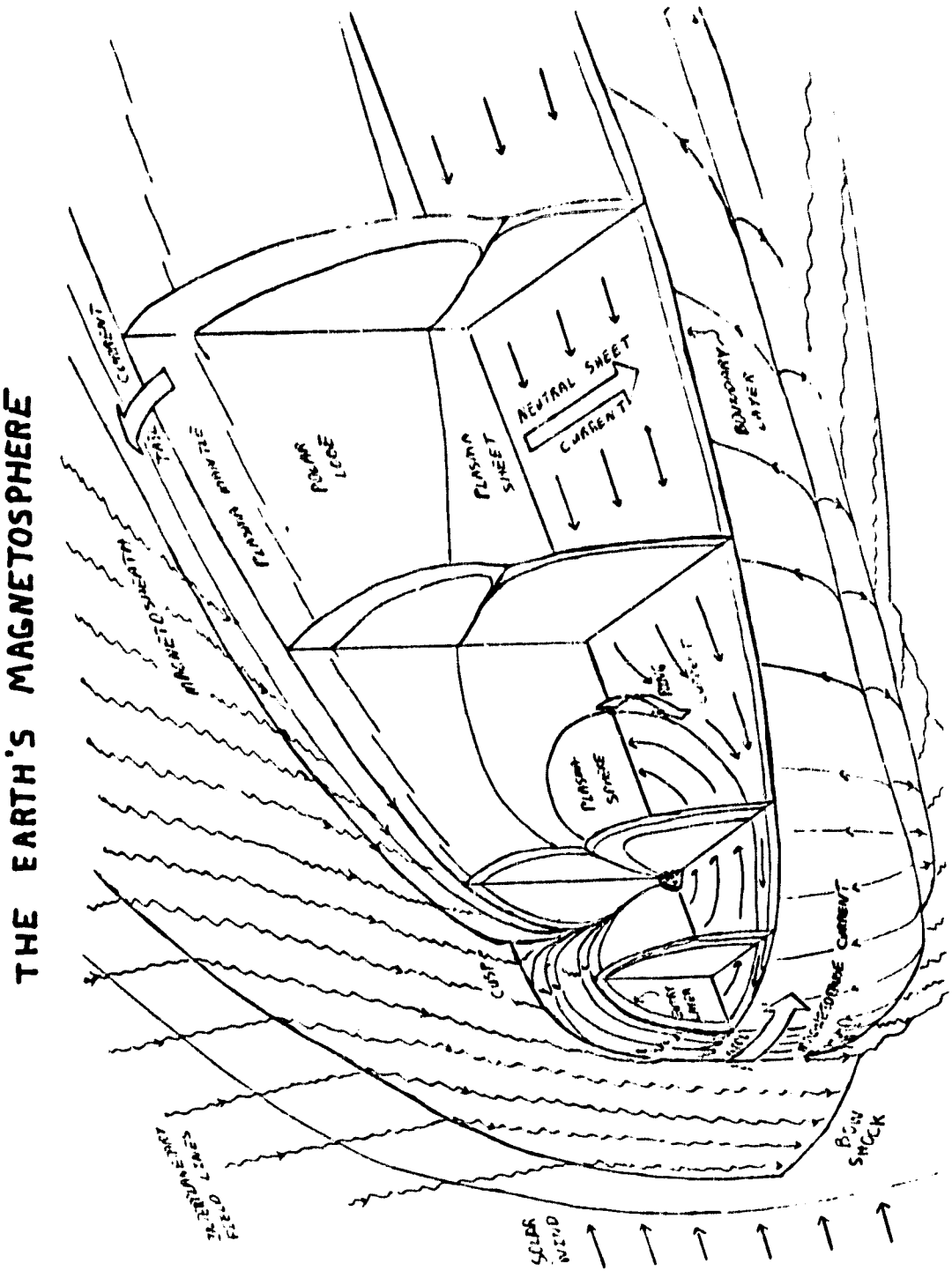
THE EARTH'S MAGNETOSPHERE
NEUTRAL SHEET
CURRENT
PLASMA SHEET
BOUNDARY LAYER
PLASMA SPHERE
CUSPS
BOW SHOCK

Figure I.1

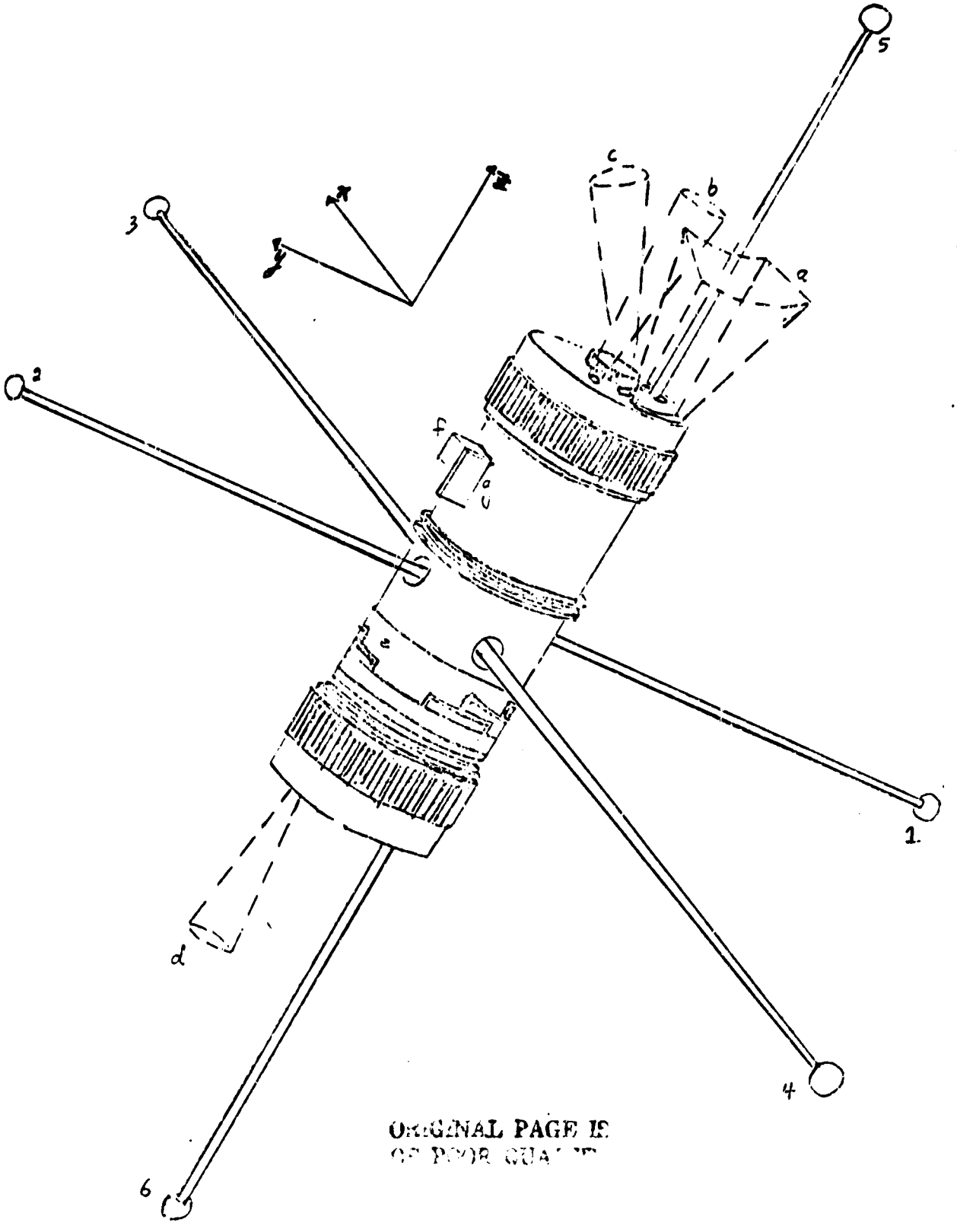

Figure II.

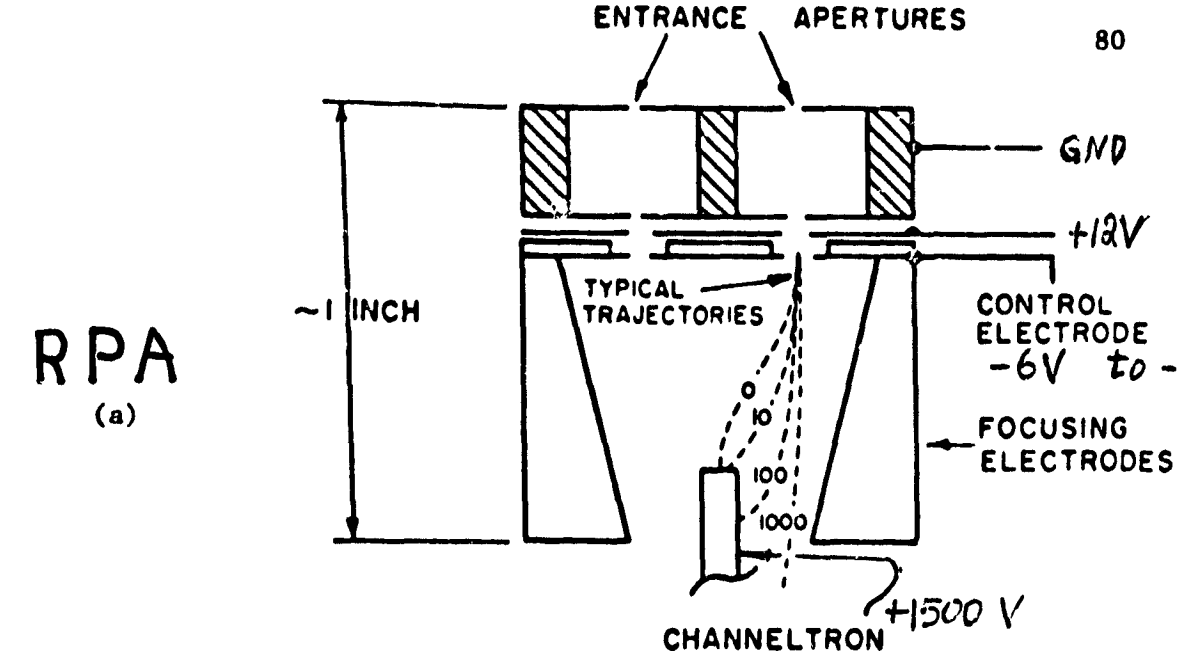

RPA

(a)

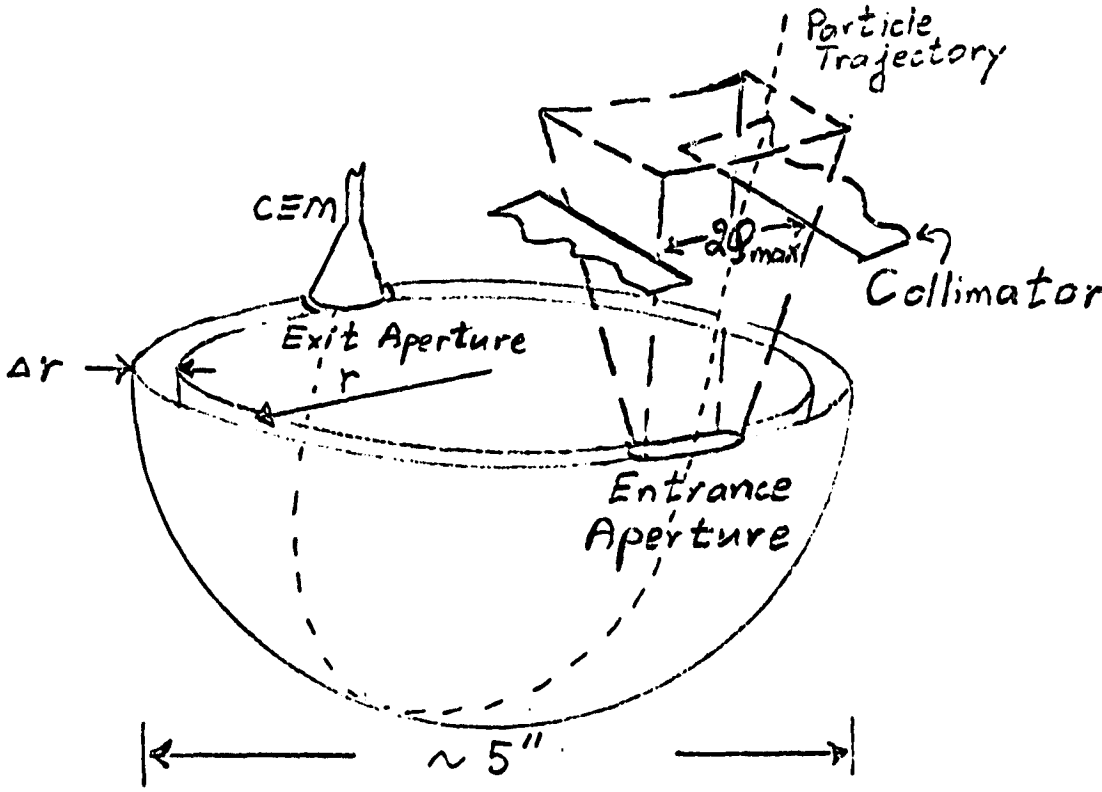

ESA

(b)

Figure II.2

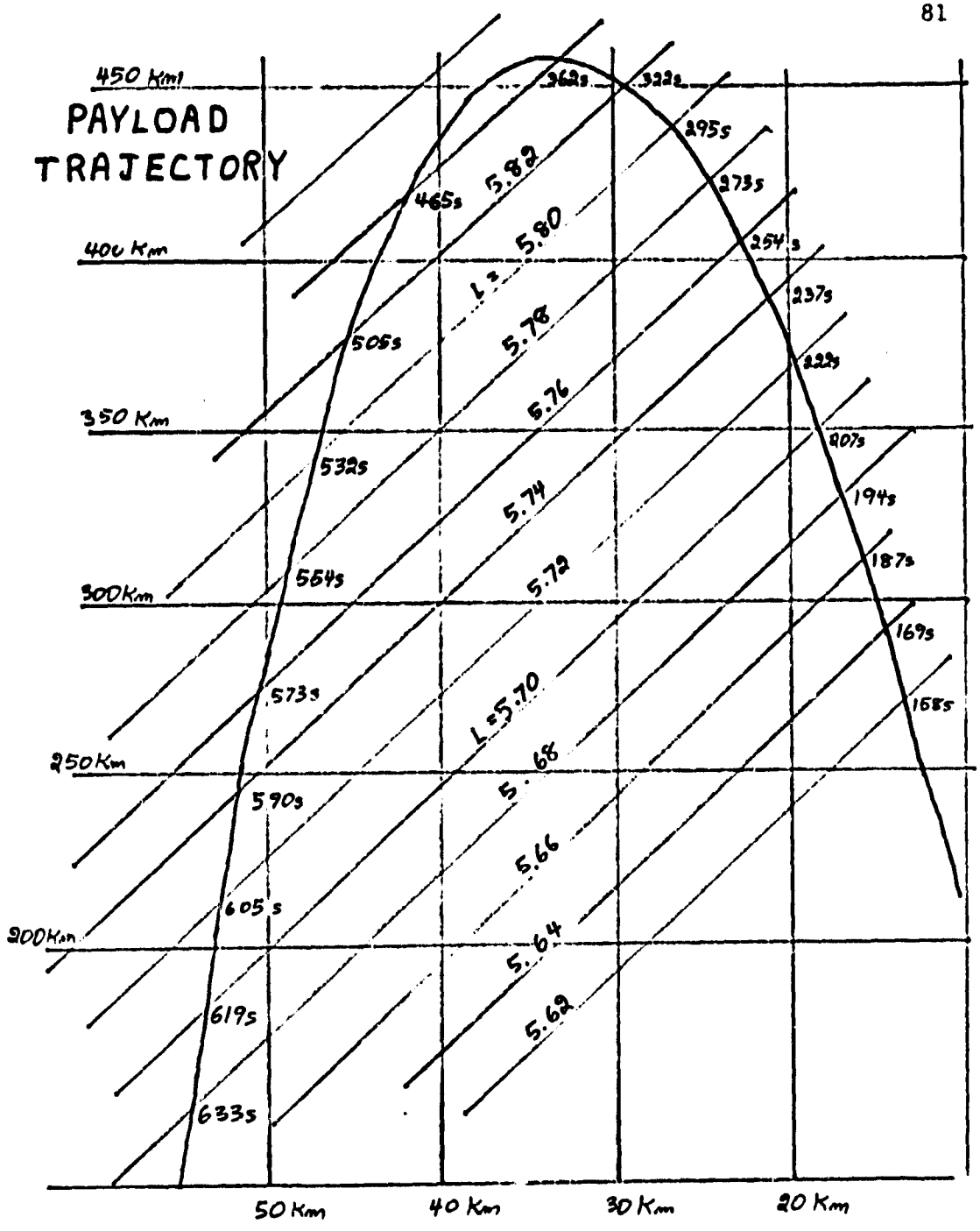
PAYLOAD
TRAJECTORY
450 Km
400 Km
350 Km
300Km
250Km
200Km
50 Km
40 Km
30 Km
20 Km
362s
322s
295s
273s
254s
237s
223s
207s
194s
187s
169s
168s
465s
506s
532s
554s
573s
590s
605s
619s
633s
5.82
5.80
5.78
5.76
5.74
5.72
L=5.70
5.68
5.66
5.64
5.62

Figure III.1

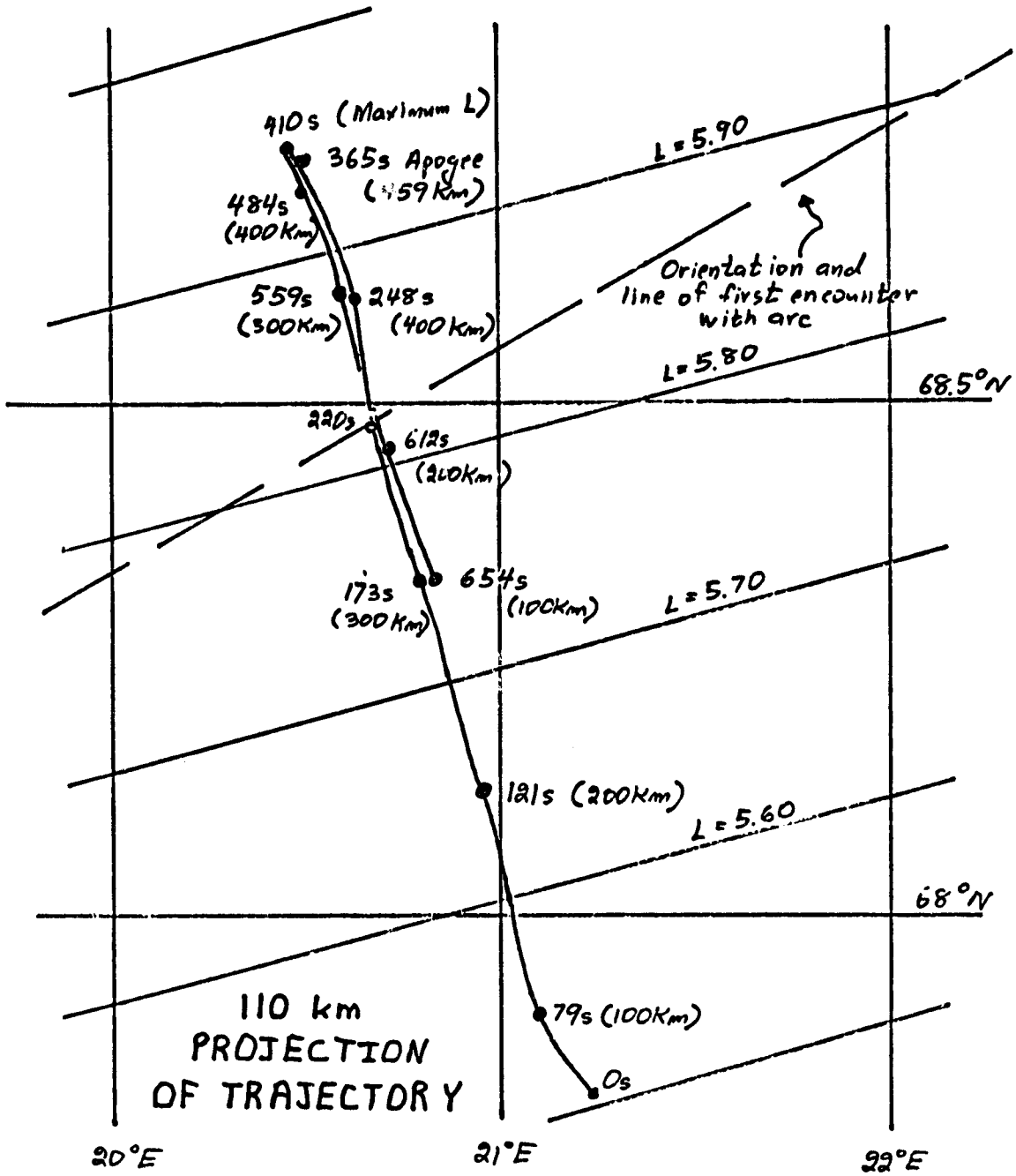
410s (Maximum L)
365s Apogee
(359 Km)
484s
(400 Km)
559s
(300 Km)
248s
(400 Km)
220s
612s
(200 Km)
654s
(100 Km)
173s
(300 Km)
121s (200 Km)
79s (100 Km)
0s
L = 5.90
L = 5.80
L = 5.70
L = 5.60
Orientation and
line of first encounter
with arc
68.5°N
68°N
110 km
PROJECTION
OF TRAJECTORY
20°E
21°E
22°E

Figure III.2

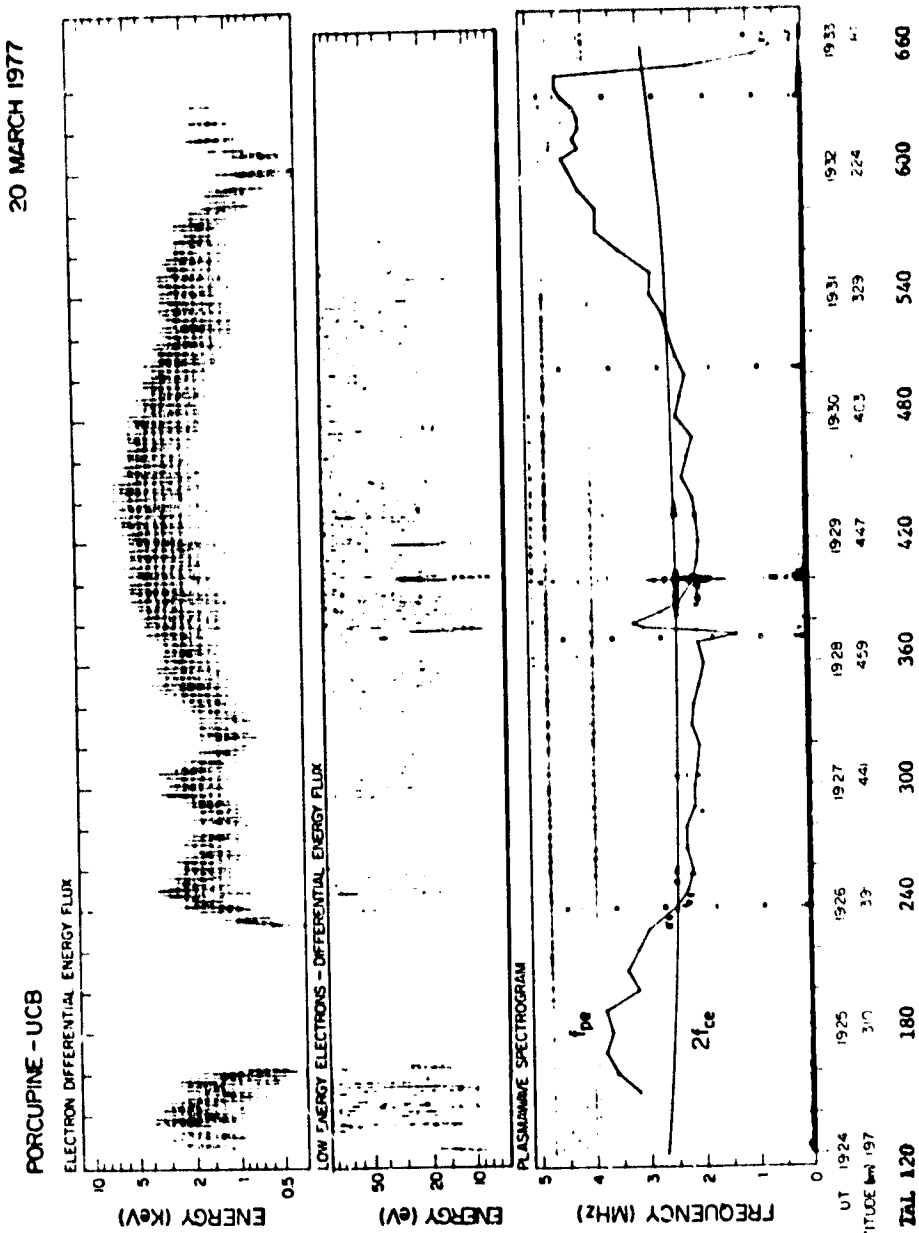
20 MARCH 1977
PORCUPINE - UCB
ELECTRON DIFFERENTIAL ENERGY FLUX
ENERGY (KeV)
LOW ENERGY ELECTRONS - DIFFERENTIAL ENERGY FLUX
ENERGY (eV)
PLASMAWAVE SPECTROGRAM
FREQUENCY (MHz)
f_{pe}
$2f_{ce}$
UT
ALTITUDE (km)
TAL
120
180
240
300
360
420
480
540
600
660

Figure IV.1

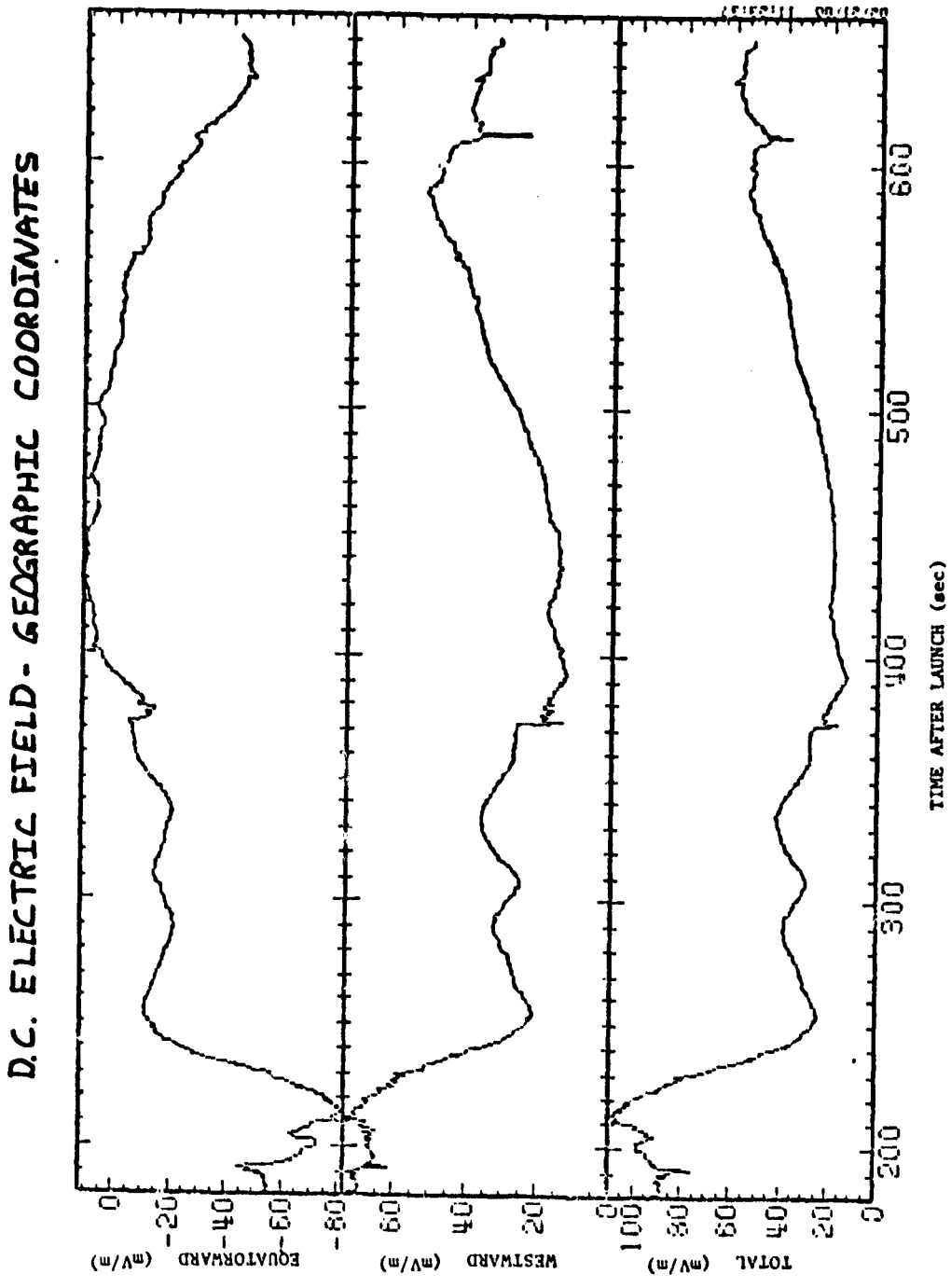
D.C. ELECTRIC FIELD- GEOGRAPHIC COORDINATES
EQUATORWARD (mV/m)
0
-20
-40
-60
WESTWARD (mV/m)
-80
60
40
20
TOTAL (mV/m)
0
100
80
60
40
20
0
200
300
400
500
600
TIME AFTER LAUNCH (sec)

Figure IV.2

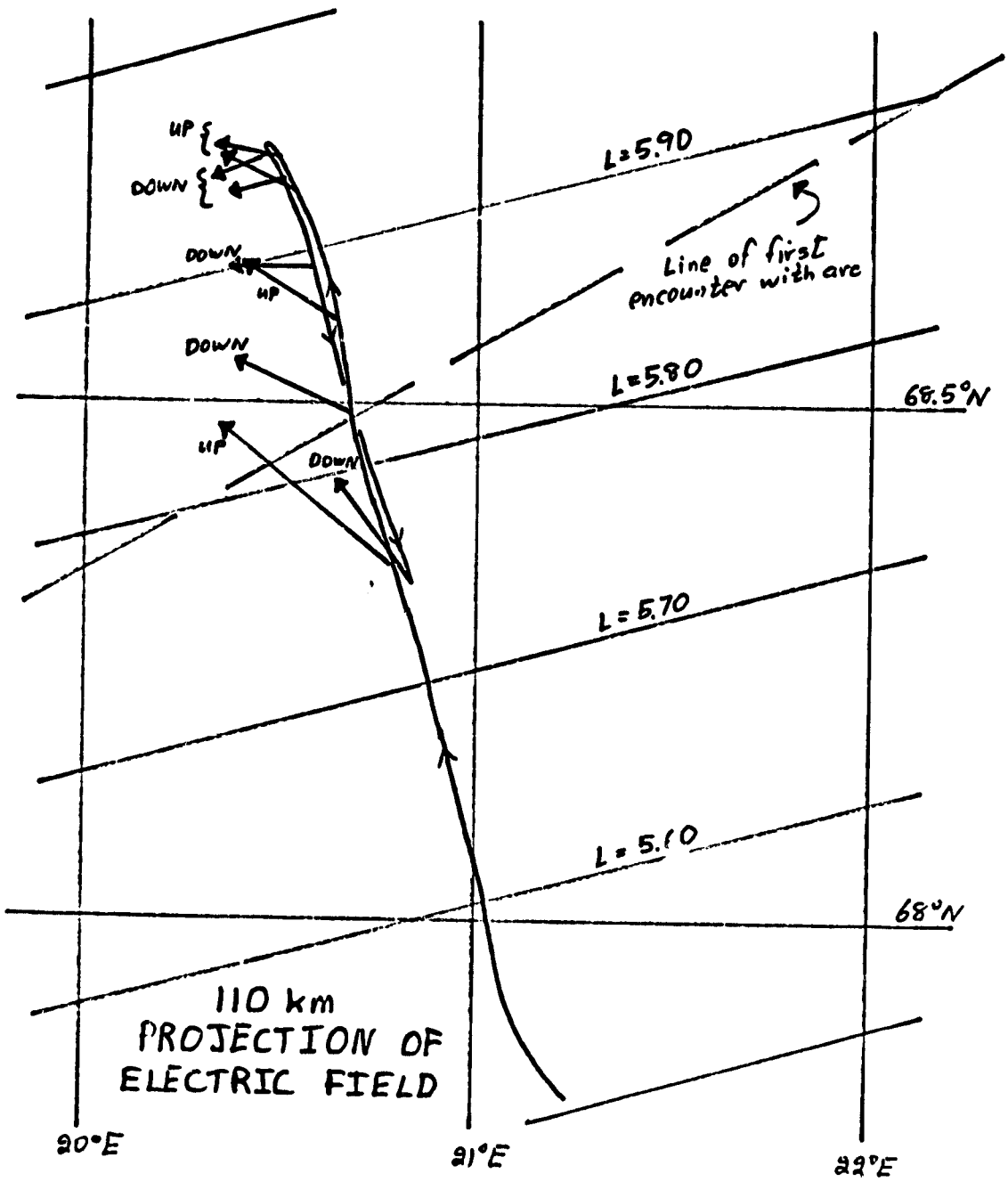
UP
DOWN
DOWN
UP
DOWN
UP
DOWN
L=5.90
Line of first encounter with arc
L=5.80
68.5°N
L=5.70
L=5.10
68°N
110 km
PROJECTION OF
ELECTRIC FIELD
20°E
21°E
22°E

Figure IV.3

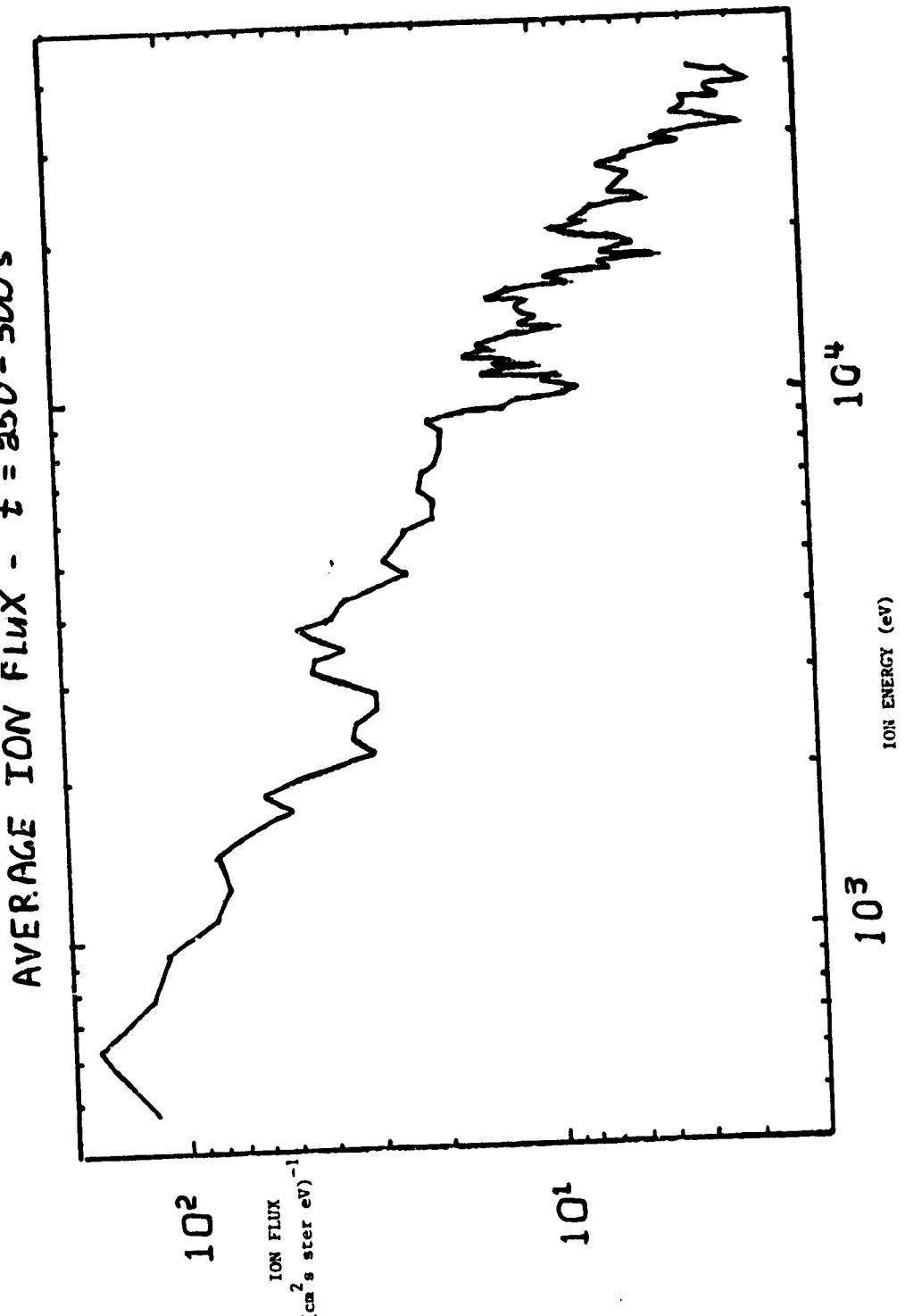
AVERAGE ION FLUX - t = 250-300 s
ION FLUX
(cm^2 s ster eV)$^{-1}$
10^2
10^1
10^3
10^4
ION ENERGY (eV)

Figure IV.4

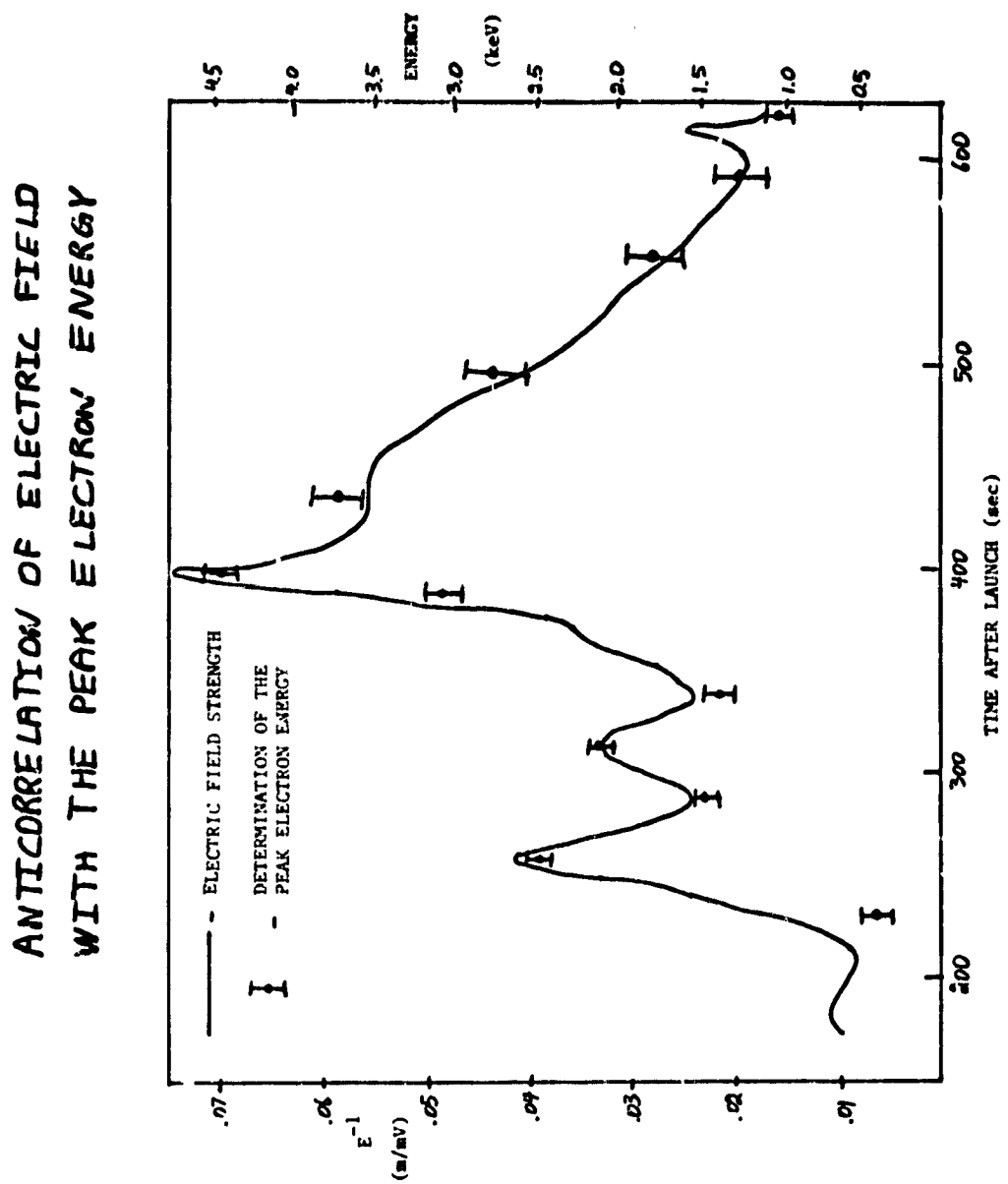
ANTICORRELATION OF ELECTRIC FIELD
WITH THE PEAK ELECTRON ENERGY
- ELECTRIC FIELD STRENGTH
- DETERMINATION OF THE PEAK ELECTRON ENERGY
ENERGY (keV)
4.5
4.0
3.5
3.0
2.5
2.0
1.5
1.0
.5
E^{-1} (m/mV)
.07
.06
.05
.04
.03
.02
.01
100
300
400
500
600
TIME AFTER LAUNCH (sec)

Figure IV.5

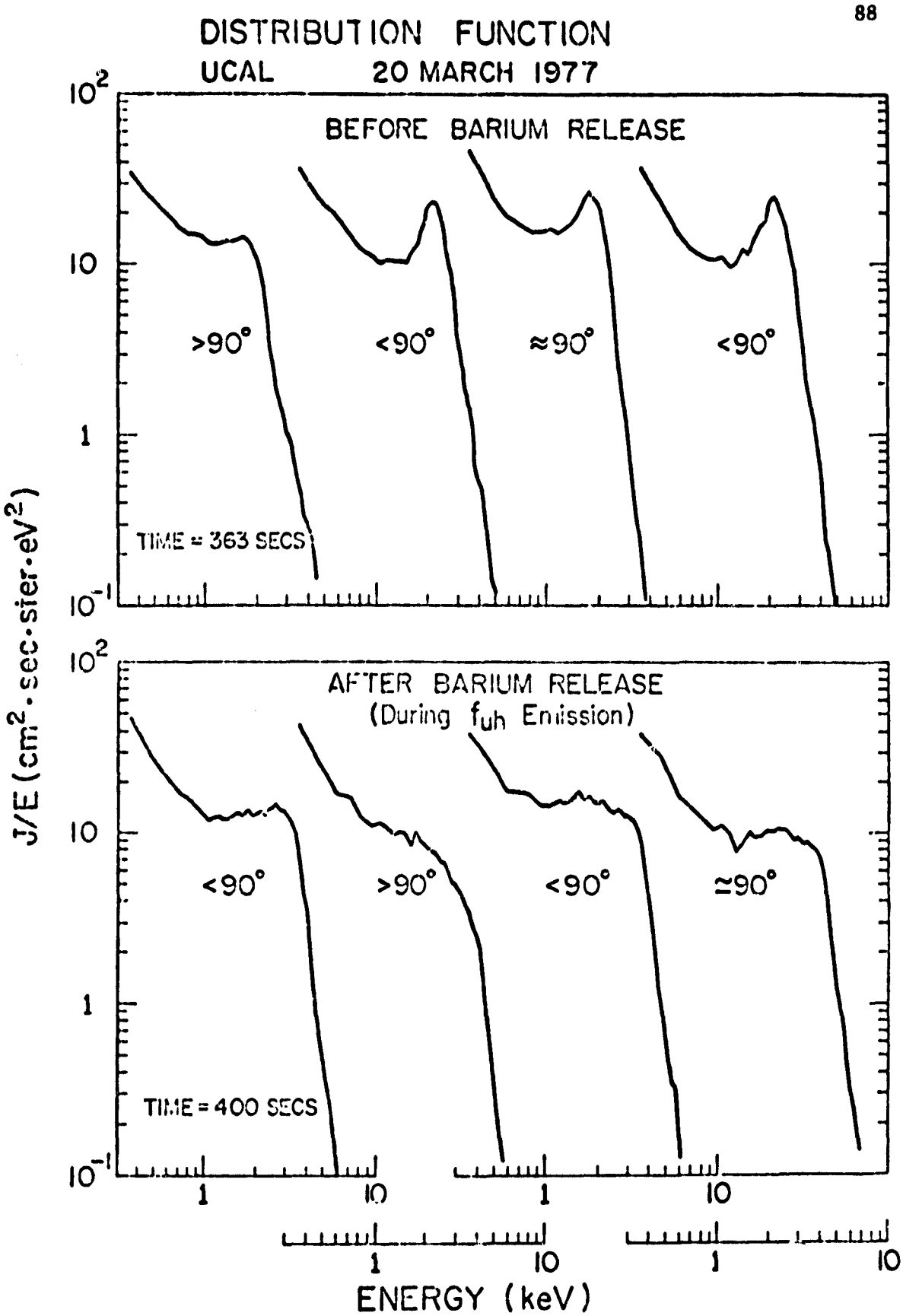
DISTRIBUTION FUNCTION
UCAL 20 MARCH 1977
BEFORE BARIUM RELEASE
>90°
<90°
≈90°
<90°
TIME = 363 SECS
AFTER BARIUM RELEASE
(During f_{uh} Emission)
<90°
>90°
<90°
≃90°
TIME = 400 SECS
J/E (cm²·sec·ster·eV²)
ENERGY (keV)

Figure IV.6

ELECTRON DISTRIBUTION FUNCTION

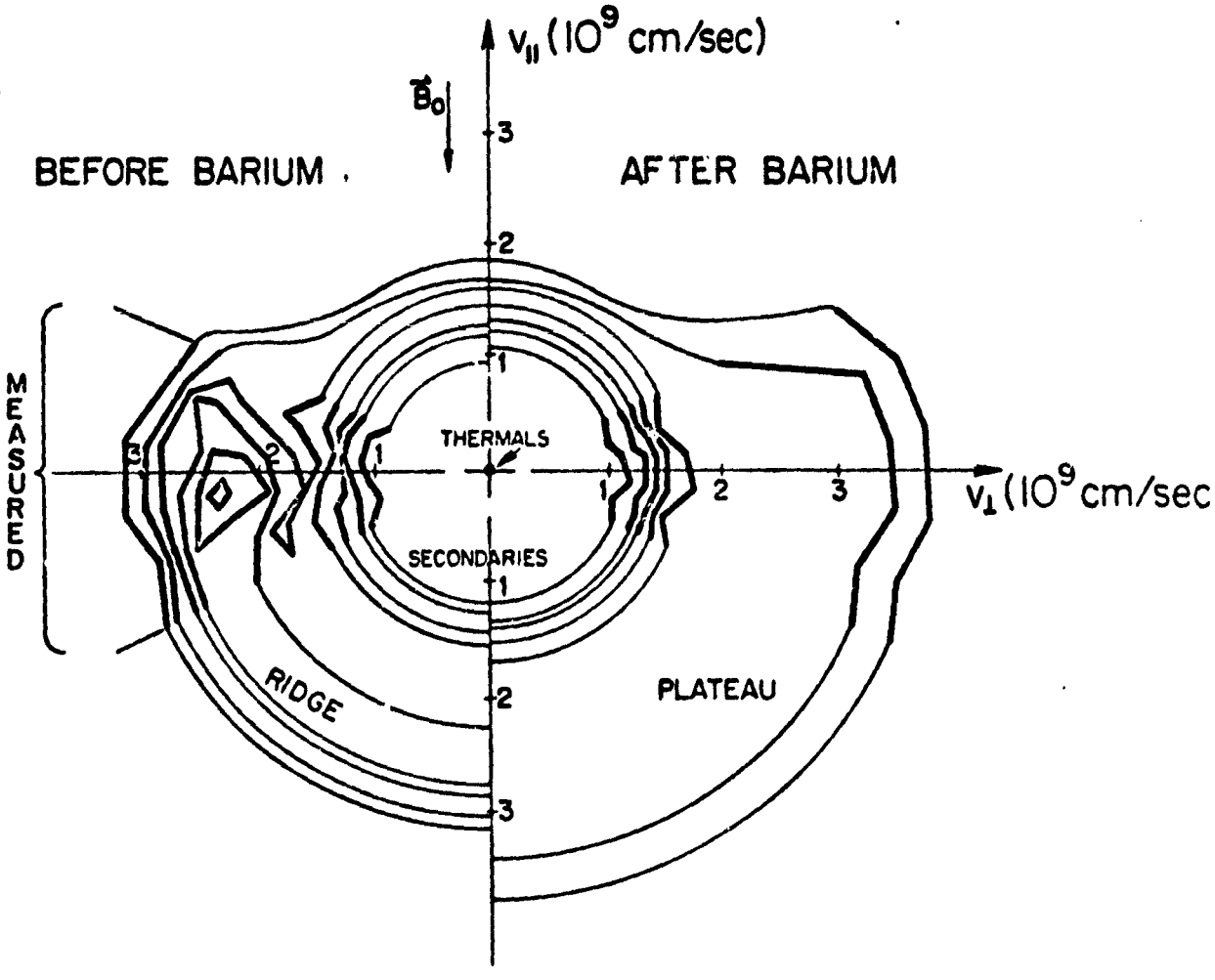

Figure IV.7

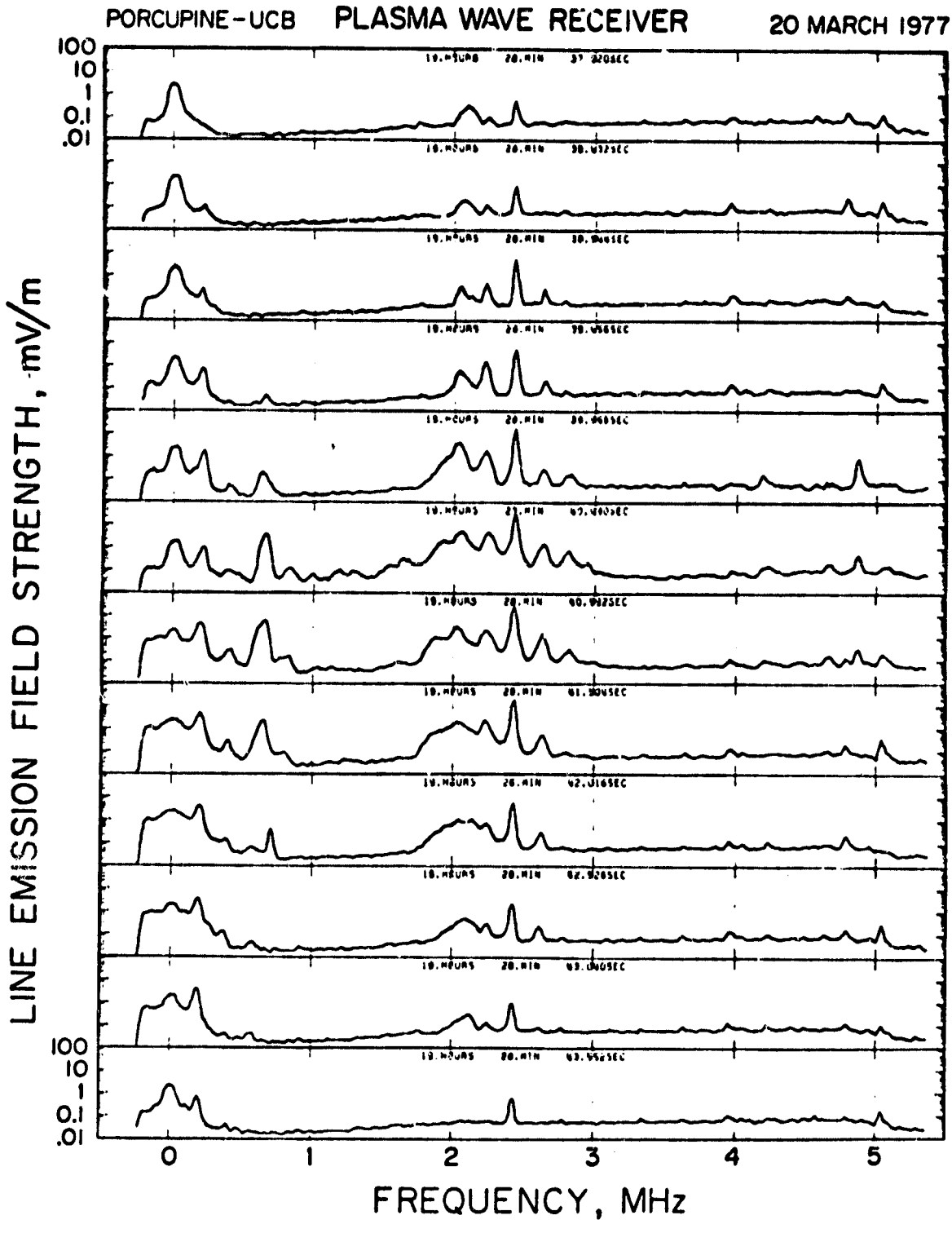
PORCUPINE-UCB
PLASMA WAVE RECEIVER
20 MARCH 1977
LINE EMISSION FIELD STRENGTH, mV/m
100
10
1
0.1
.01
FREQUENCY, MHz
0
1
2
3
4
5

Figure IV.8

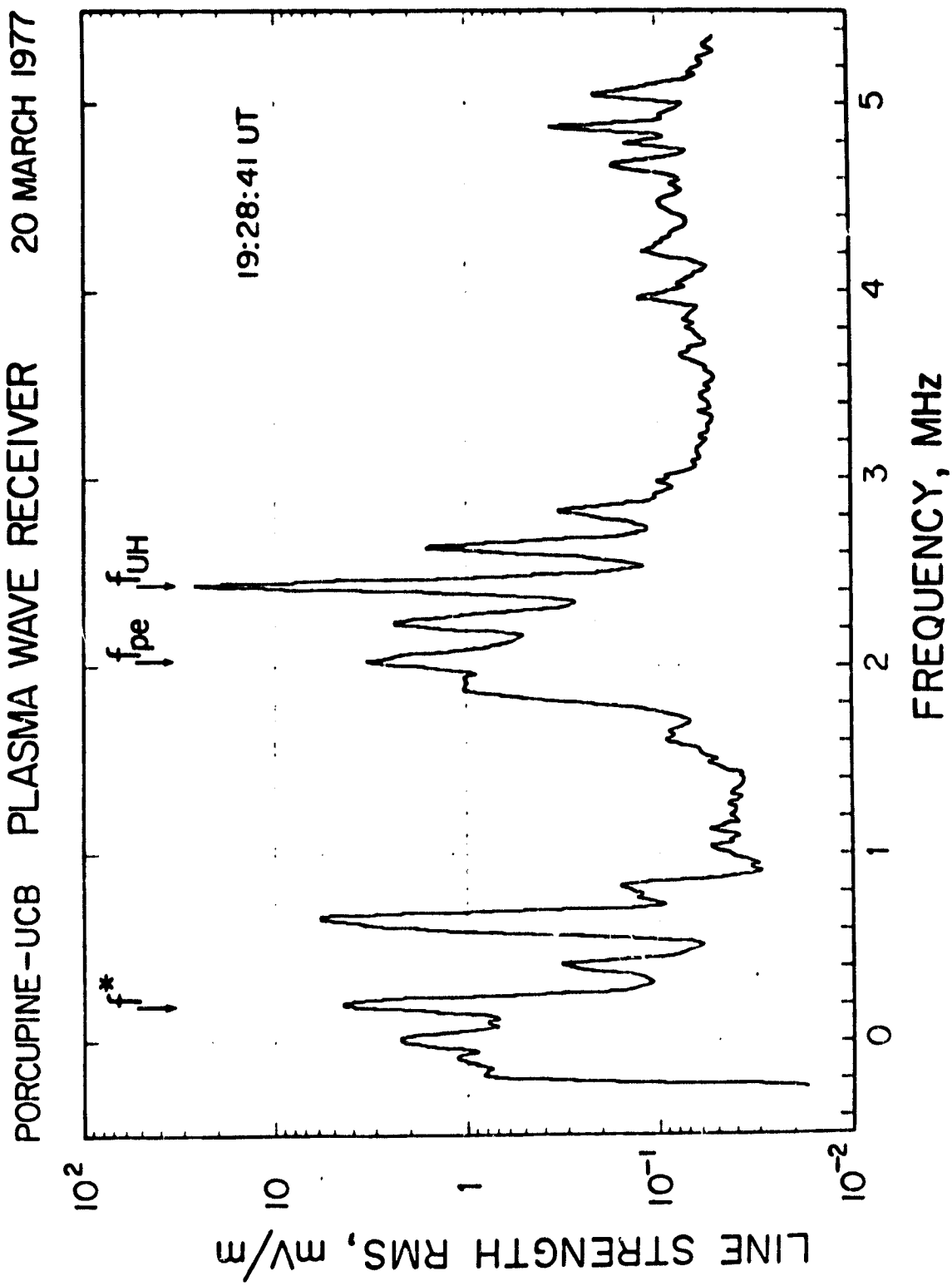
PORCUPINE-UCB PLASMA WAVE RECEIVER 20 MARCH 1977
19:28:41 UT
f^*
f_{pe}
f_{UH}
LINE STRENGTH RMS, mV/m
10^2
10
1
10^{-1}
10^{-2}
0
1
2
3
4
5
FREQUENCY, MHz

Figure IV.9

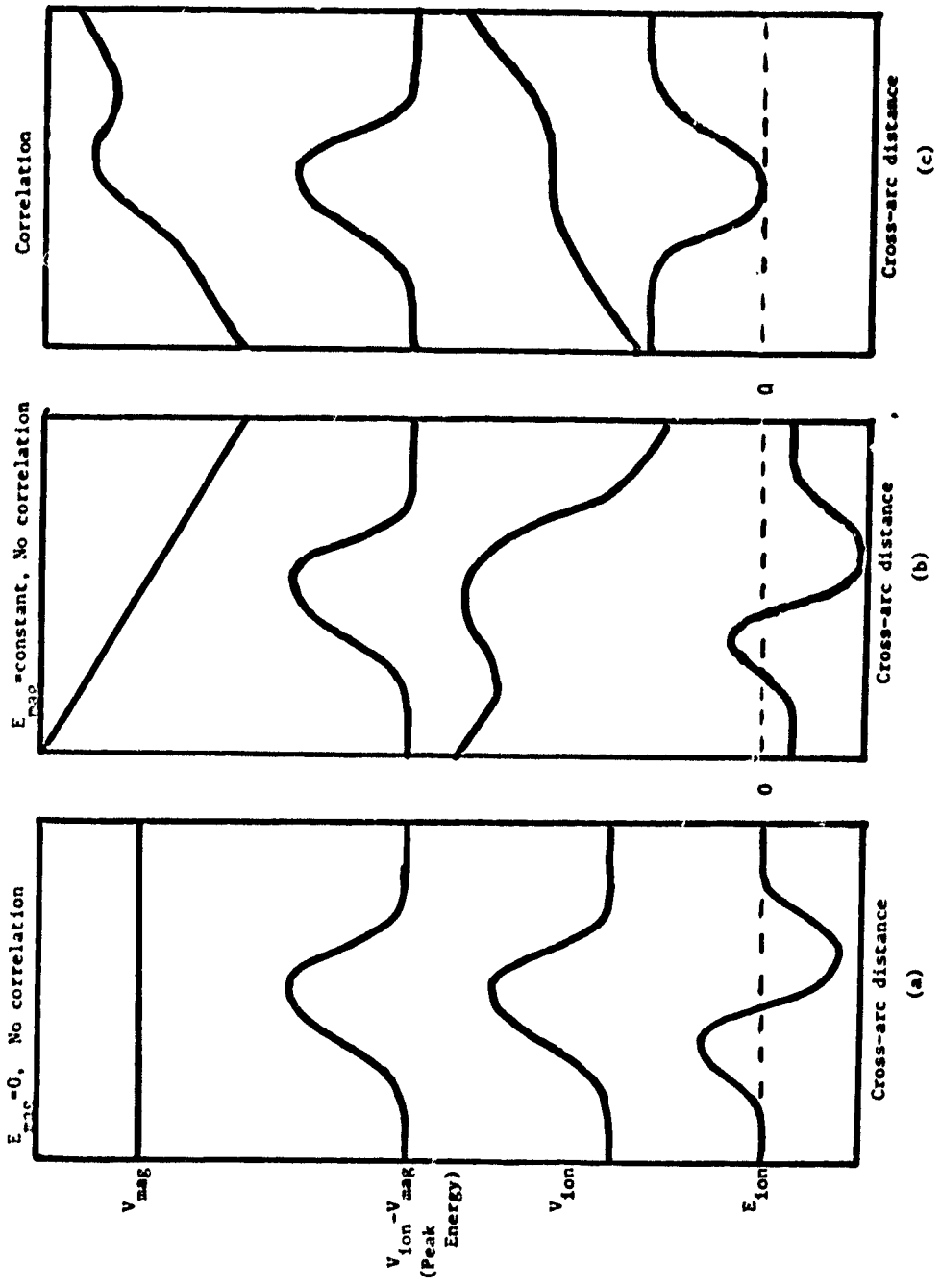
Correlation
Cross-arc distance
(c)
0
E_{mag} =constant, No correlation
Cross-arc distance
(b)
0
E_{mag} =0, No correlation
Cross-arc distance
(a)
V_{mag}
$V_{ion}-V_{mag}$ (Peak Energy)
V_{ion}
E_{ion}

Figure V.1

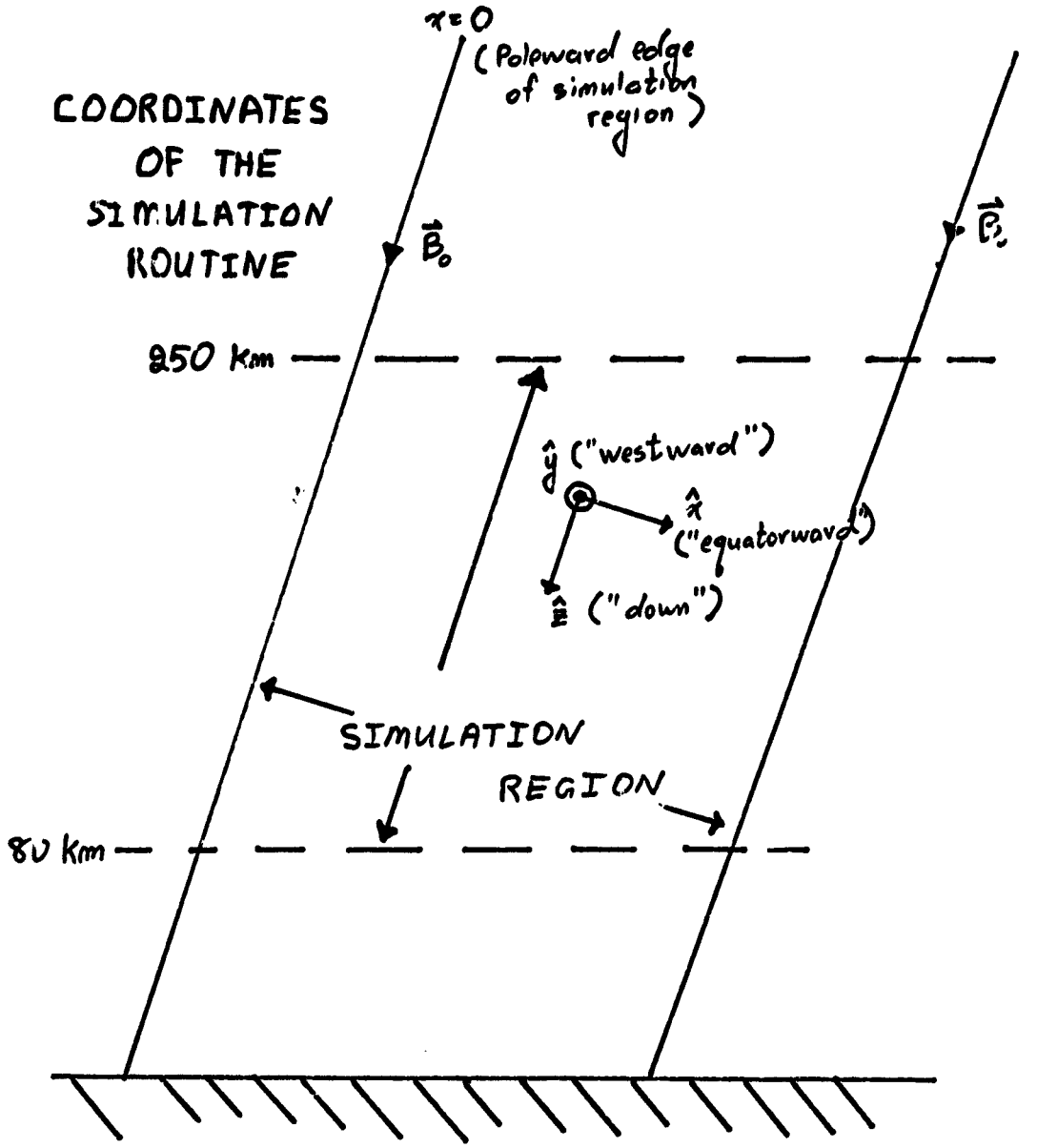
x=0
(Poleward edge of simulation region)
COORDINATES OF THE SIMULATION ROUTINE
$\vec{B}_0$
$\vec{B}_0$
250 km
$\hat{y}$ ("westward")
$\hat{x}$ ("equatorward")
$\hat{z}$ ("down")
SIMULATION REGION
80 km

C-2

Figure V.2

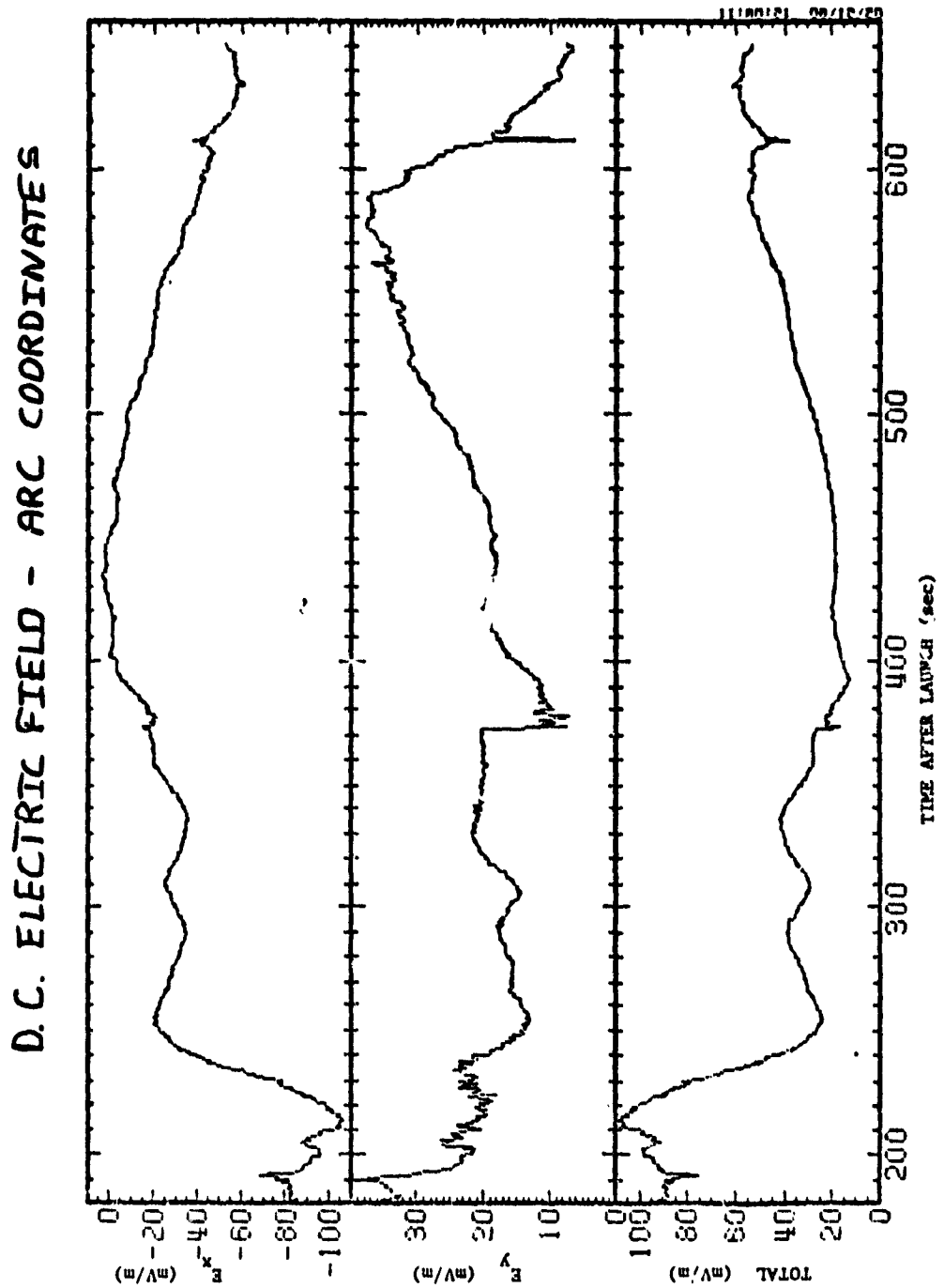
D.C. ELECTRIC FIELD - ARC COORDINATES
E_x (mV/m)
E_y (mV/m)
TOTAL (mV/m)
TIME AFTER LAUNCH (sec)

Figure V.3

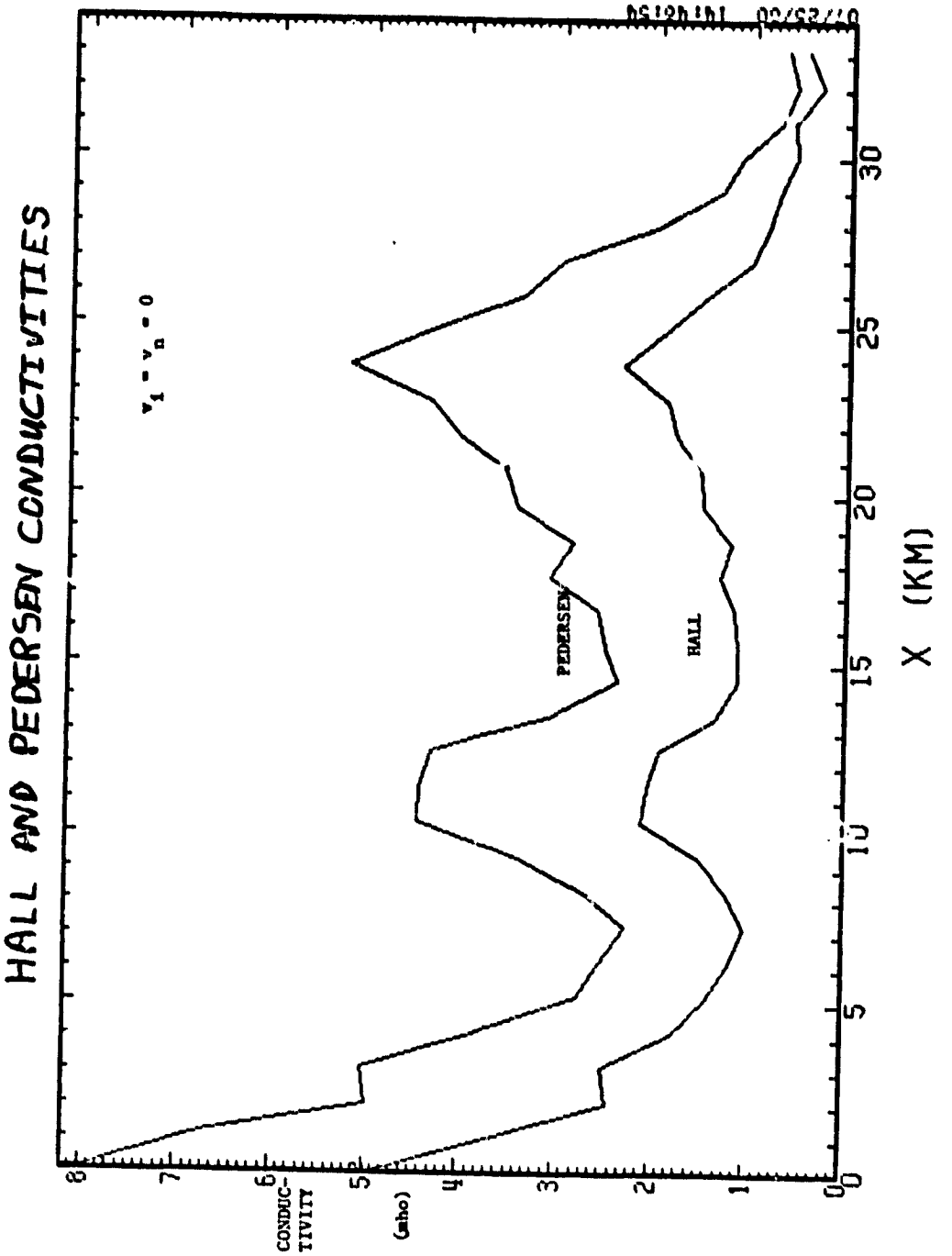
HALL AND PEDERSEN CONDUCTIVITIES
$\nu_1 = \nu_n = 0$
PEDERSEN
HALL
CONDUC-
TIVITY
(mho)
X (KM)
0
1
2
3
4
5
6
7
8
5
10
15
20
25
30

Figure V.4

RELATIVE VELOCITIES

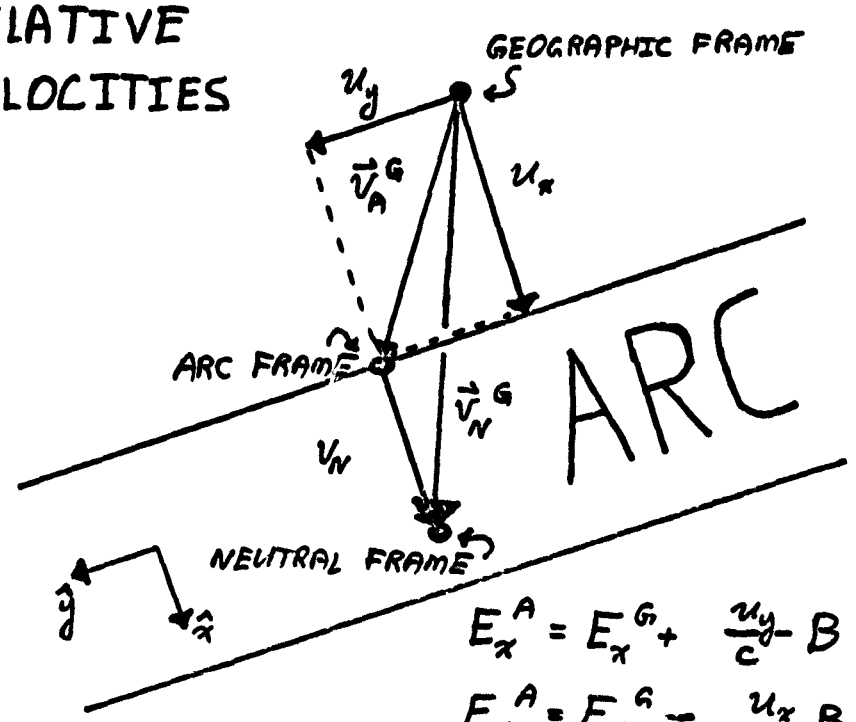

$$E_x^A = E_x^G + \frac{u_y}{c} B$$

$$E_y^A = E_y^G - \frac{u_x}{c} B$$

$\vec{V}_A^G$ = velocity of the arc in the geographic frame

$\vec{V}_N^G$ = velocity of the neutrals in the geographic frame

Figure V.5

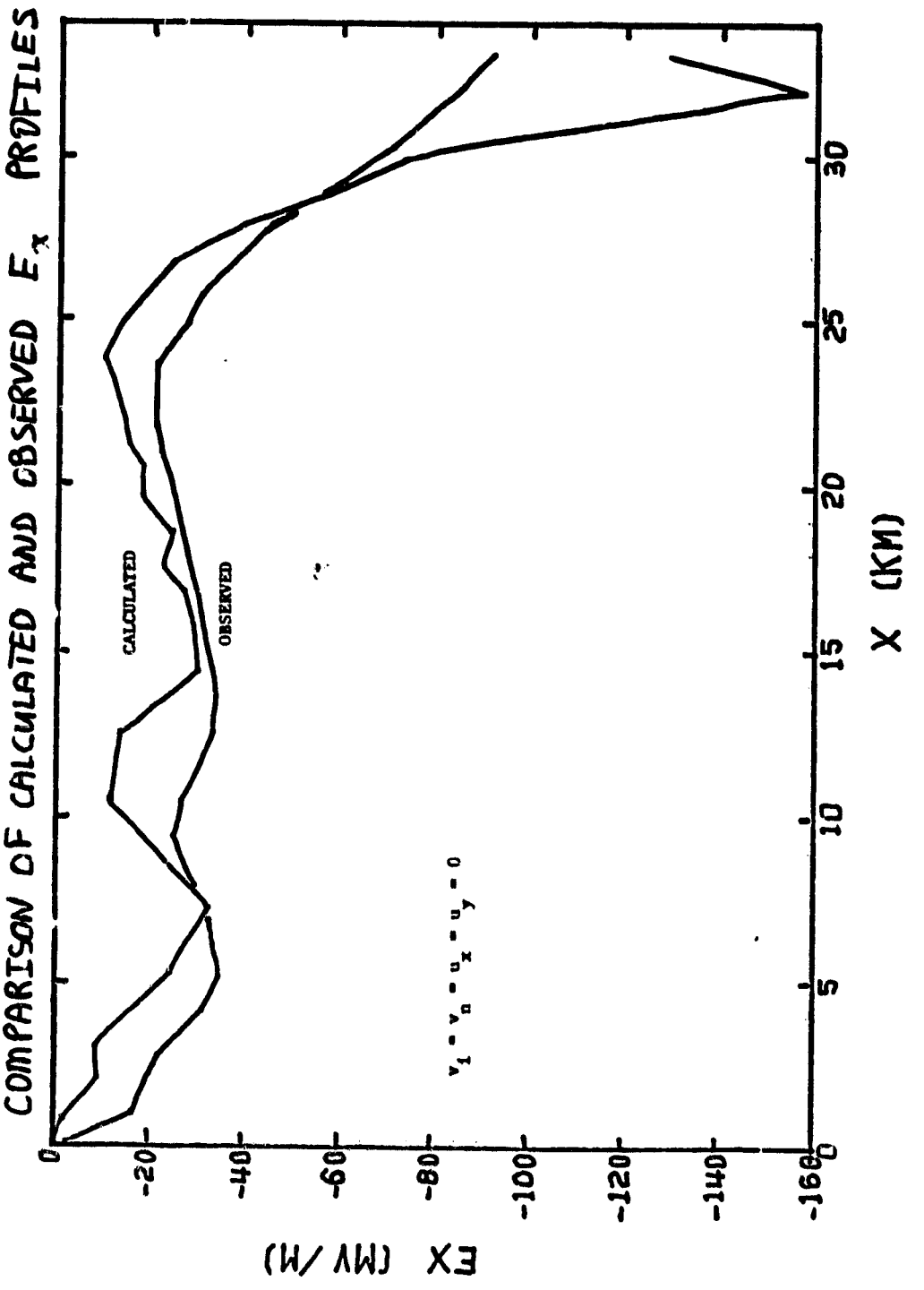
COMPARISON OF CALCULATED AND OBSERVED E_x PROFILES
CALCULATED
OBSERVED
$v_1 = v_2 = u_x = u_y = 0$
EX (MV/M)
X (KM)
0
-20
-40
-60
-80
-100
-120
-140
-160
5
10
15
20
25
30

Figure V.6

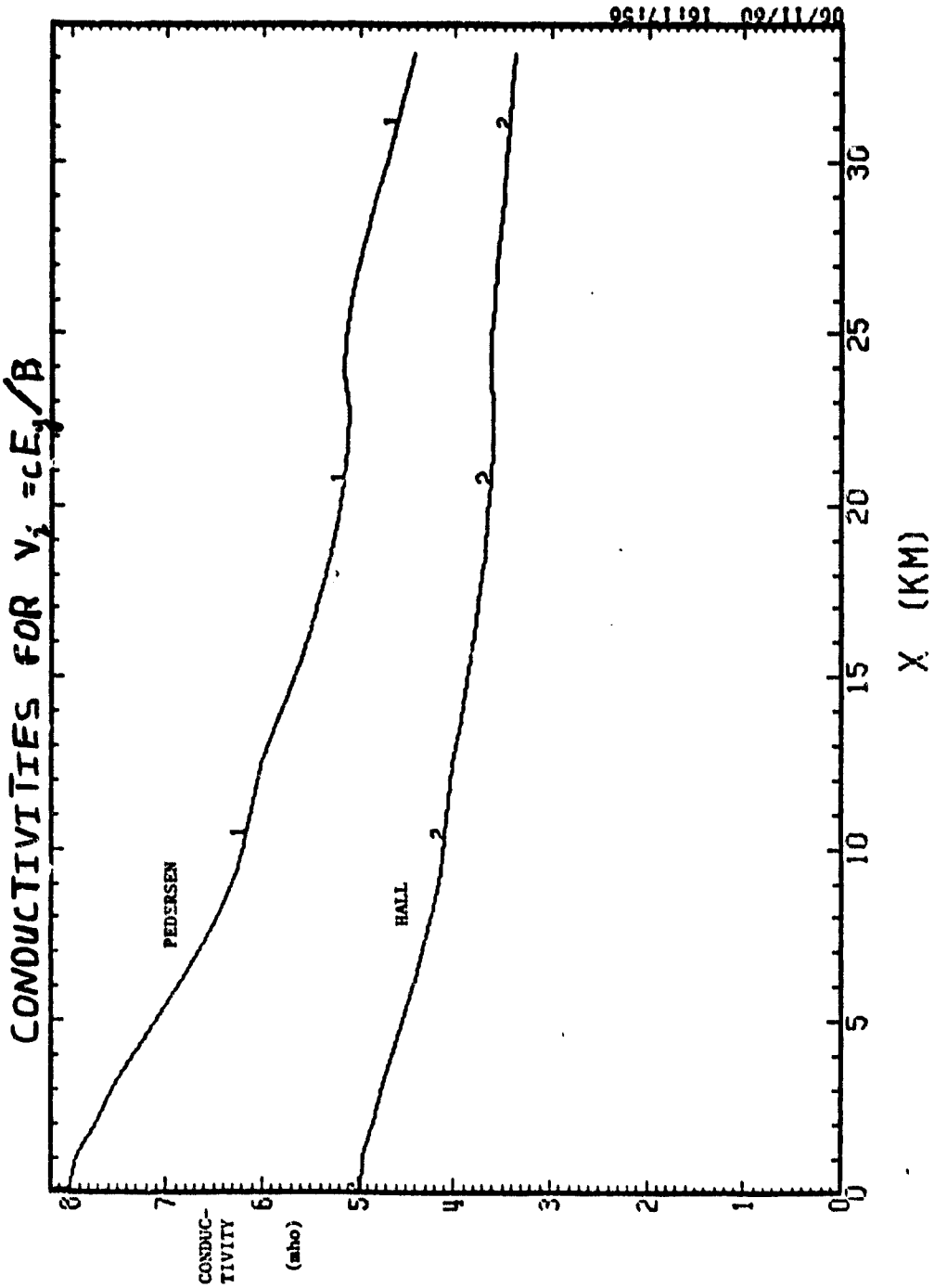
CONDUCTIVITIES FOR $V_i = cE_y/B$
PEDERSEN
HALL
1
2
CONDUC-
TIVITY
(mho)
X (KM)
0
1
2
3
4
5
6
7
0
5
10
15
20
25
30

Figure V.7

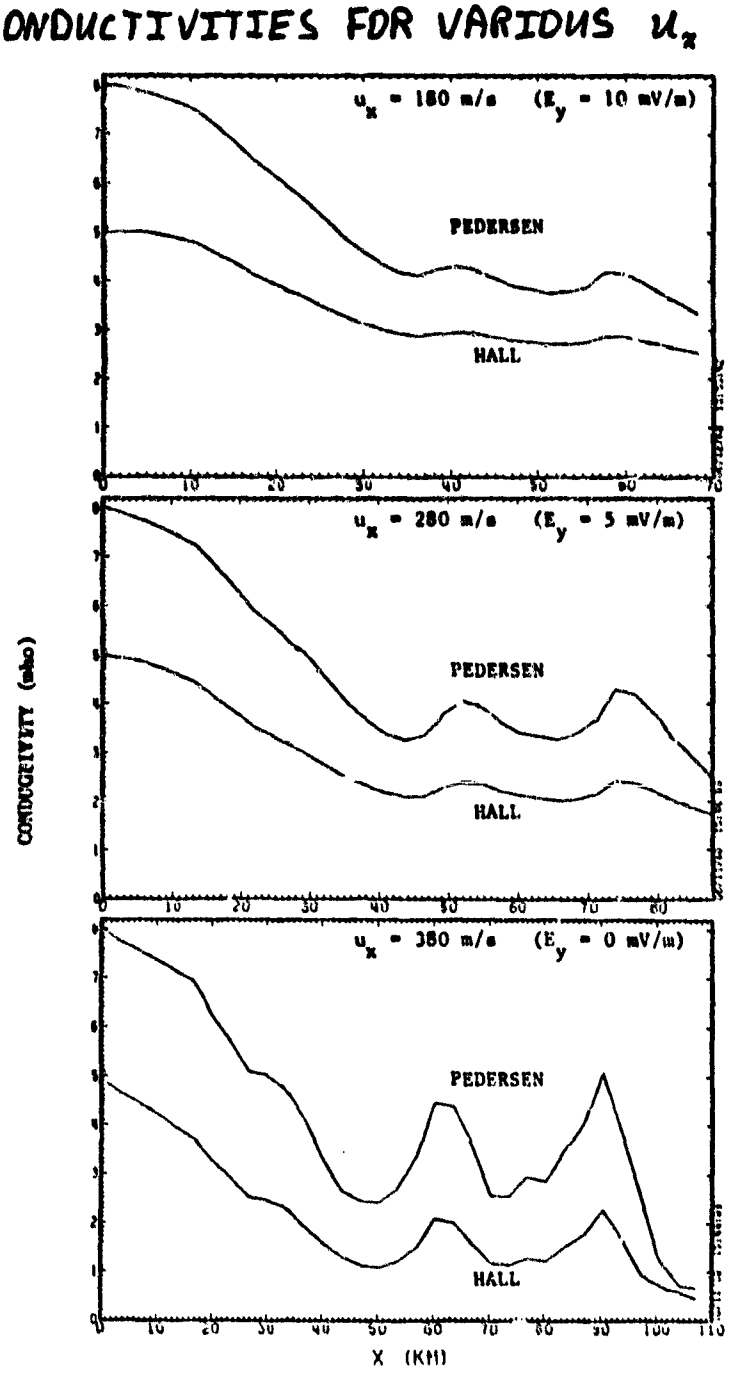
CONDUCTIVITIES FOR VARIOUS u_x
u_x = 180 m/s (E_y = 10 mV/m)
PEDERSEN
HALL
u_x = 280 m/s (E_y = 5 mV/m)
PEDERSEN
HALL
u_x = 380 m/s (E_y = 0 mV/m)
PEDERSEN
HALL
CONDUCTIVITY (mho)
X (KM)

Figure V.8

E_x PROFILES FOR VARIOUS u_y AND v_n

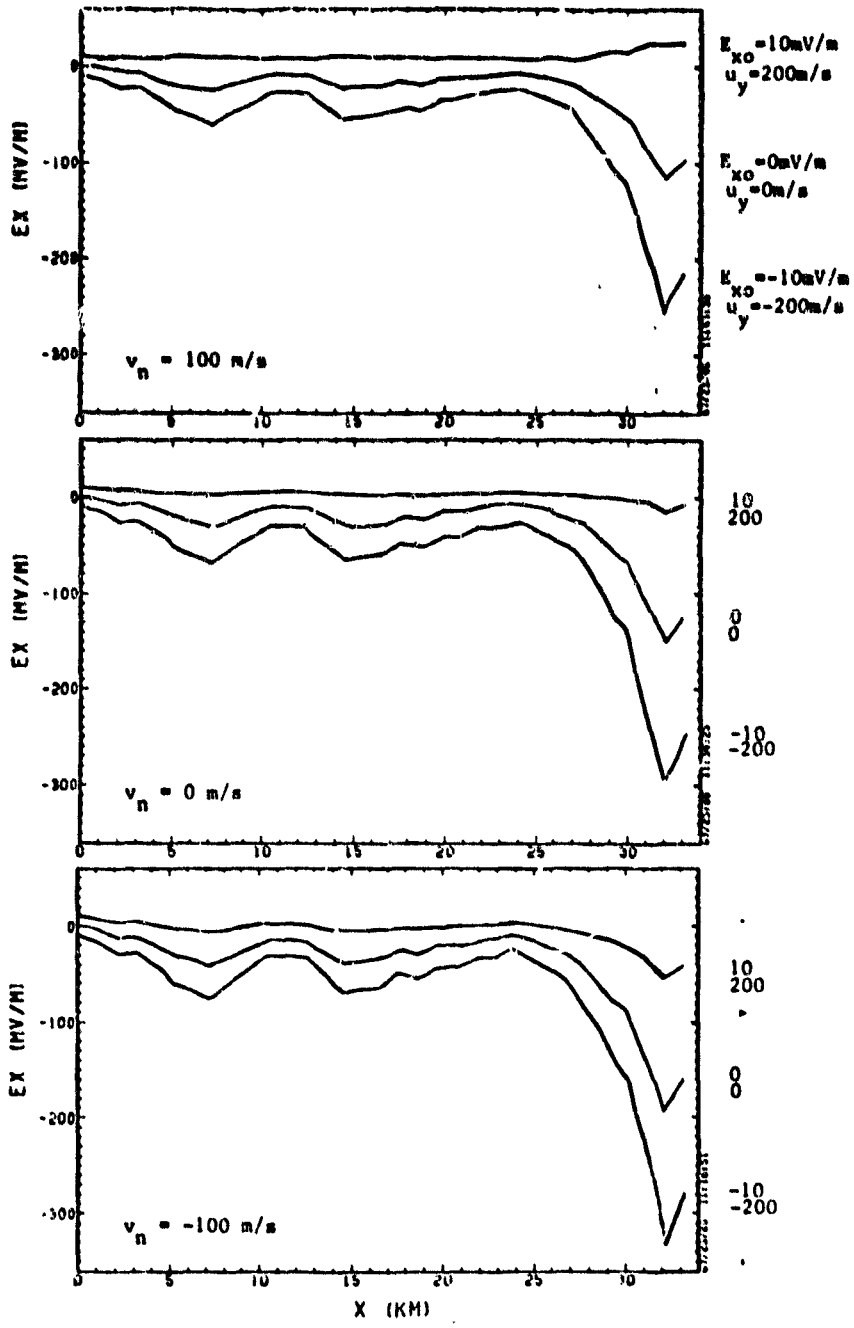

Figure V.9

CONDUCTIVITIES AS A FUNCTION OF PEAK ENERGY

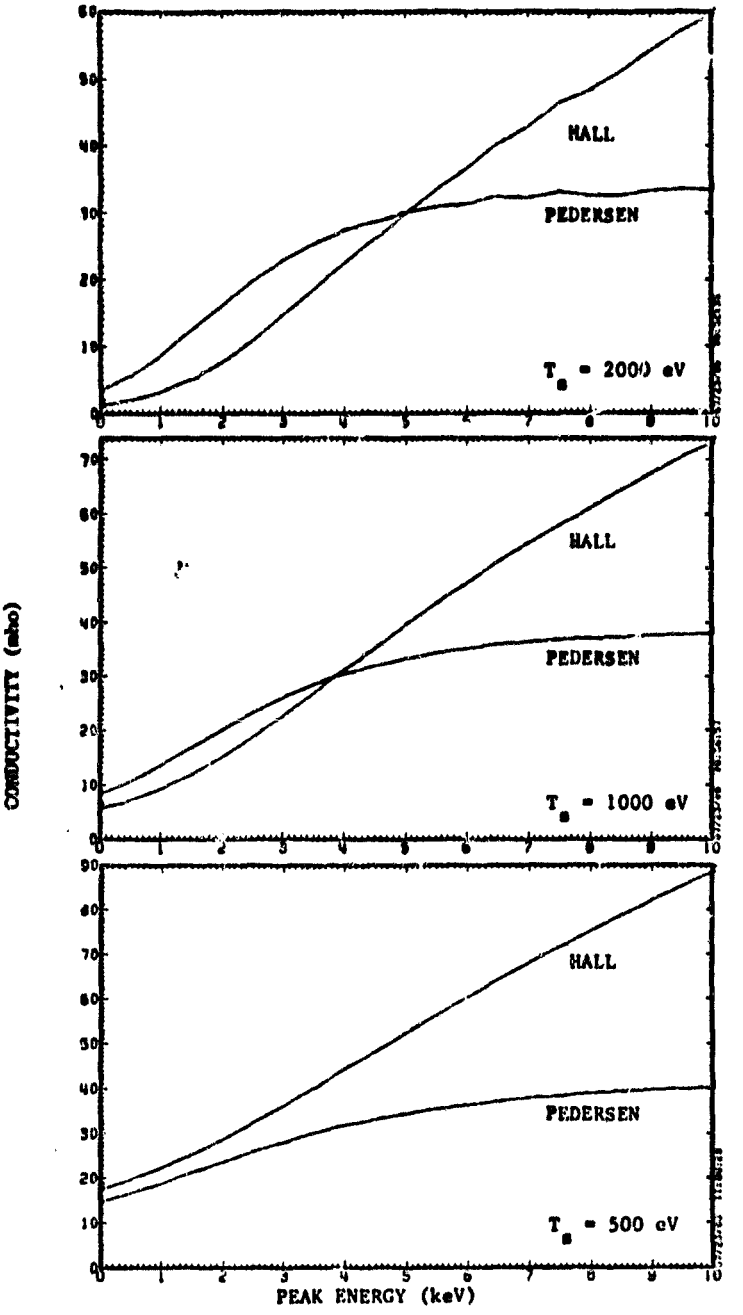

Figure V.10

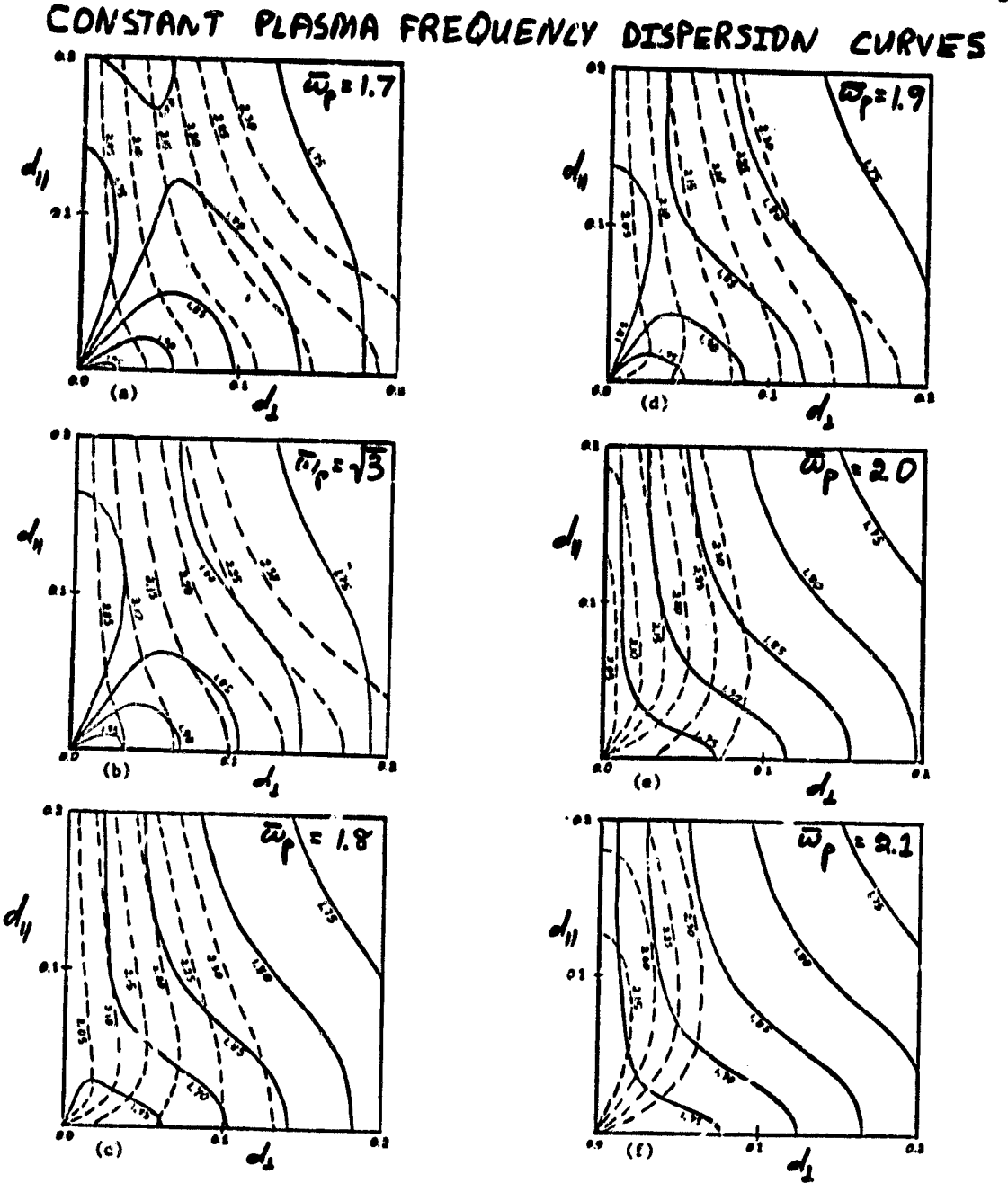
CONSTANT PLASMA FREQUENCY DISPERSION CURVES
$\bar{\omega}_p = 1.7$
$\bar{\omega}_p = 1.9$
$\bar{\omega}_p = \sqrt{3}$
$\bar{\omega}_p = 2.0$
$\bar{\omega}_p = 1.8$
$\bar{\omega}_p = 2.1$
$d_{\parallel}$
$d_{\perp}$
(a)
(b)
(c)
(d)
(e)
(f)

Figure V.11

CONSTANT WAVE FREQUENCY DISPERSION CURVES

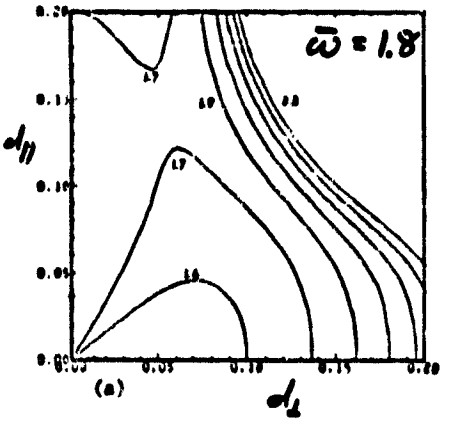

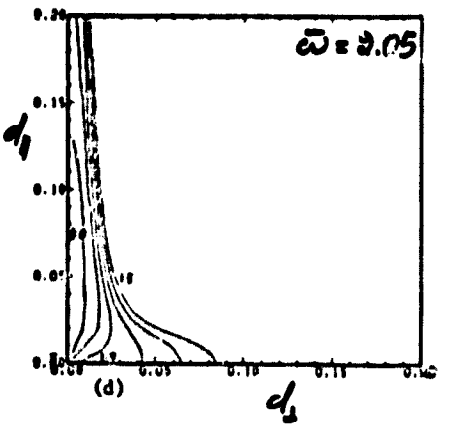

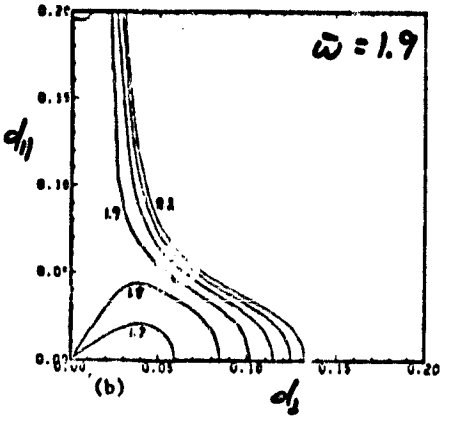

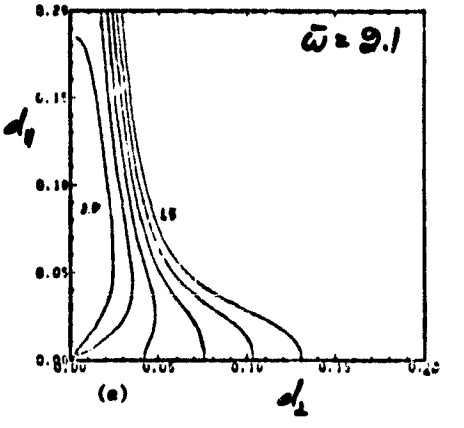

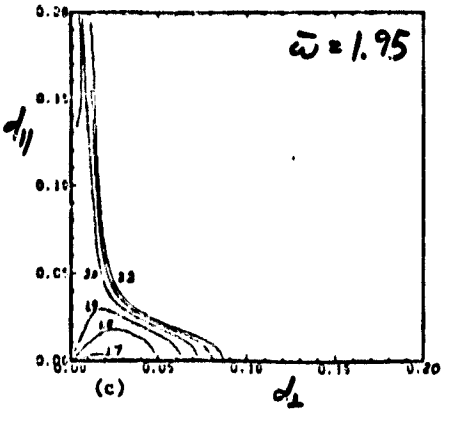

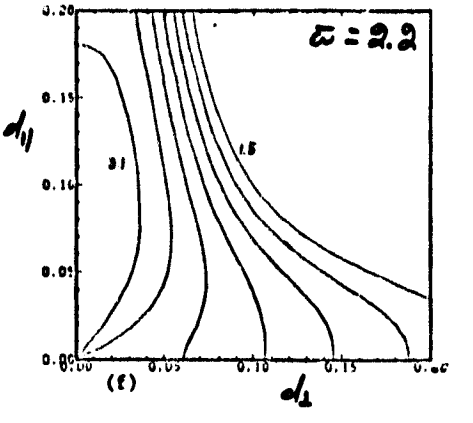

Figure V.12

DETAIL OF DISPERSION CURVES

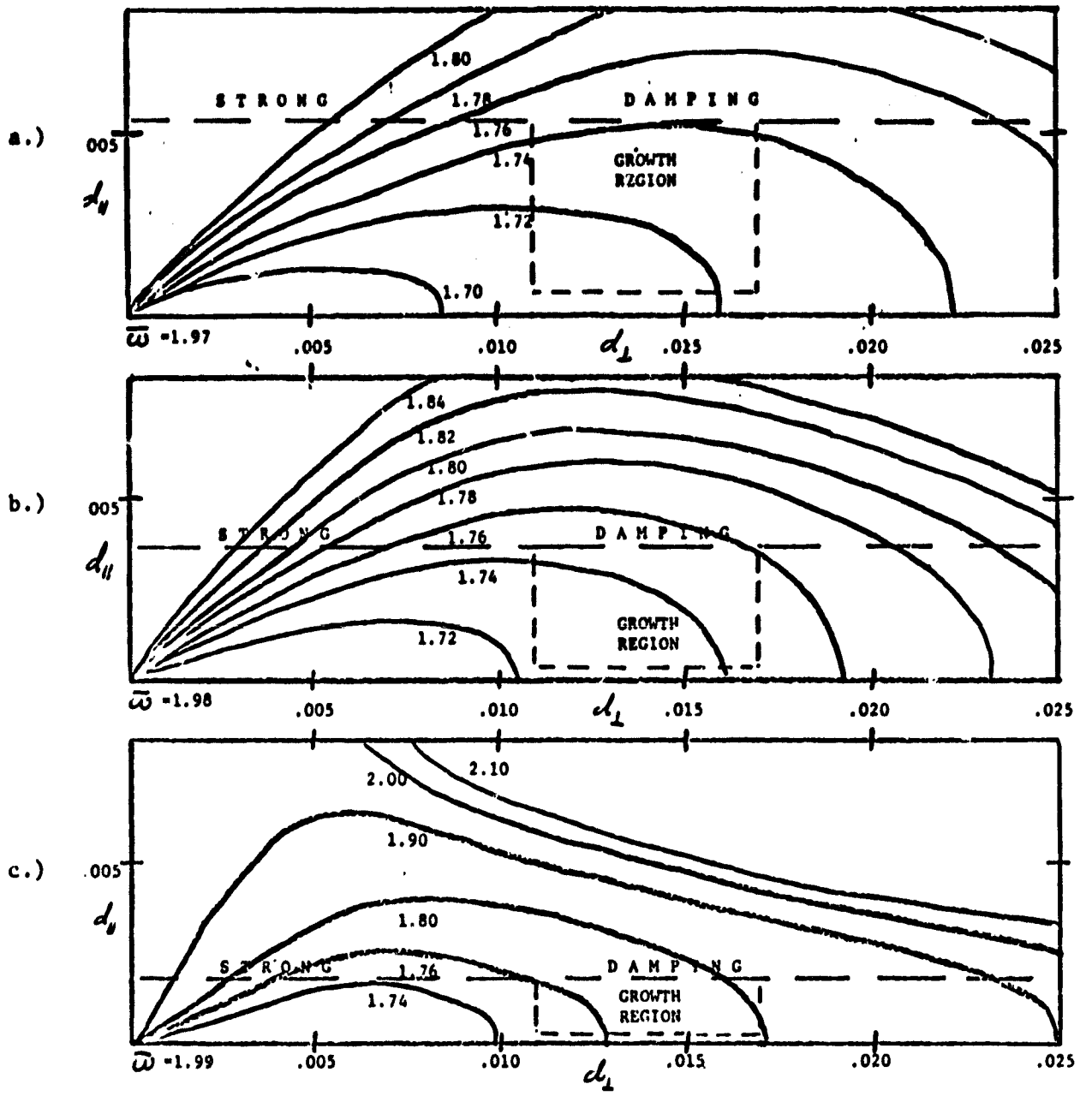

Figure V.13

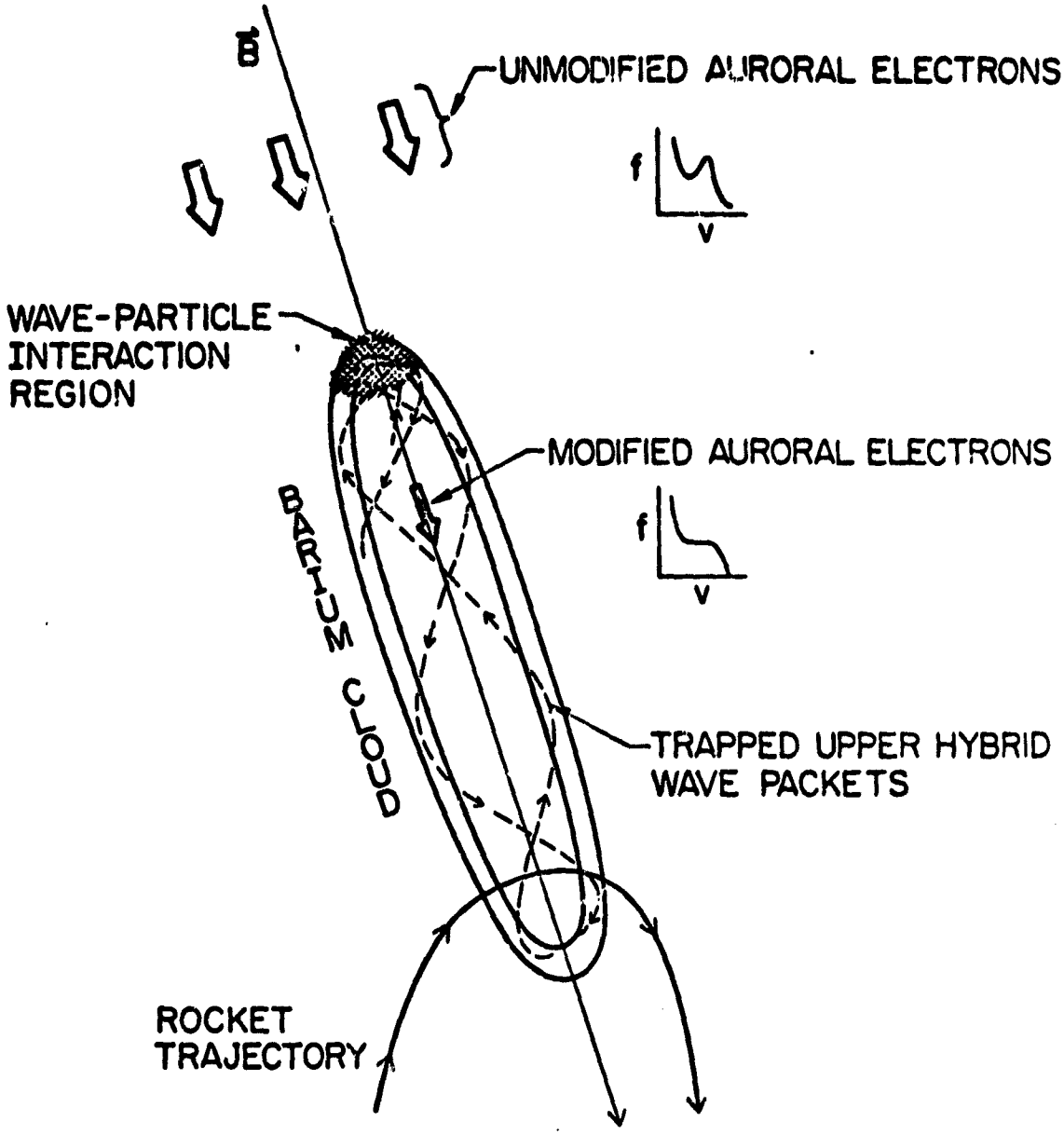
B
UNMODIFIED AURORAL ELECTRONS
f
v
WAVE-PARTICLE
INTERACTION
REGION
MODIFIED AURORAL ELECTRONS
f
v
BARIUM CLOUD
TRAPPED UPPER HYBRID
WAVE PACKETS
ROCKET
TRAJECTORY

Figure V.14

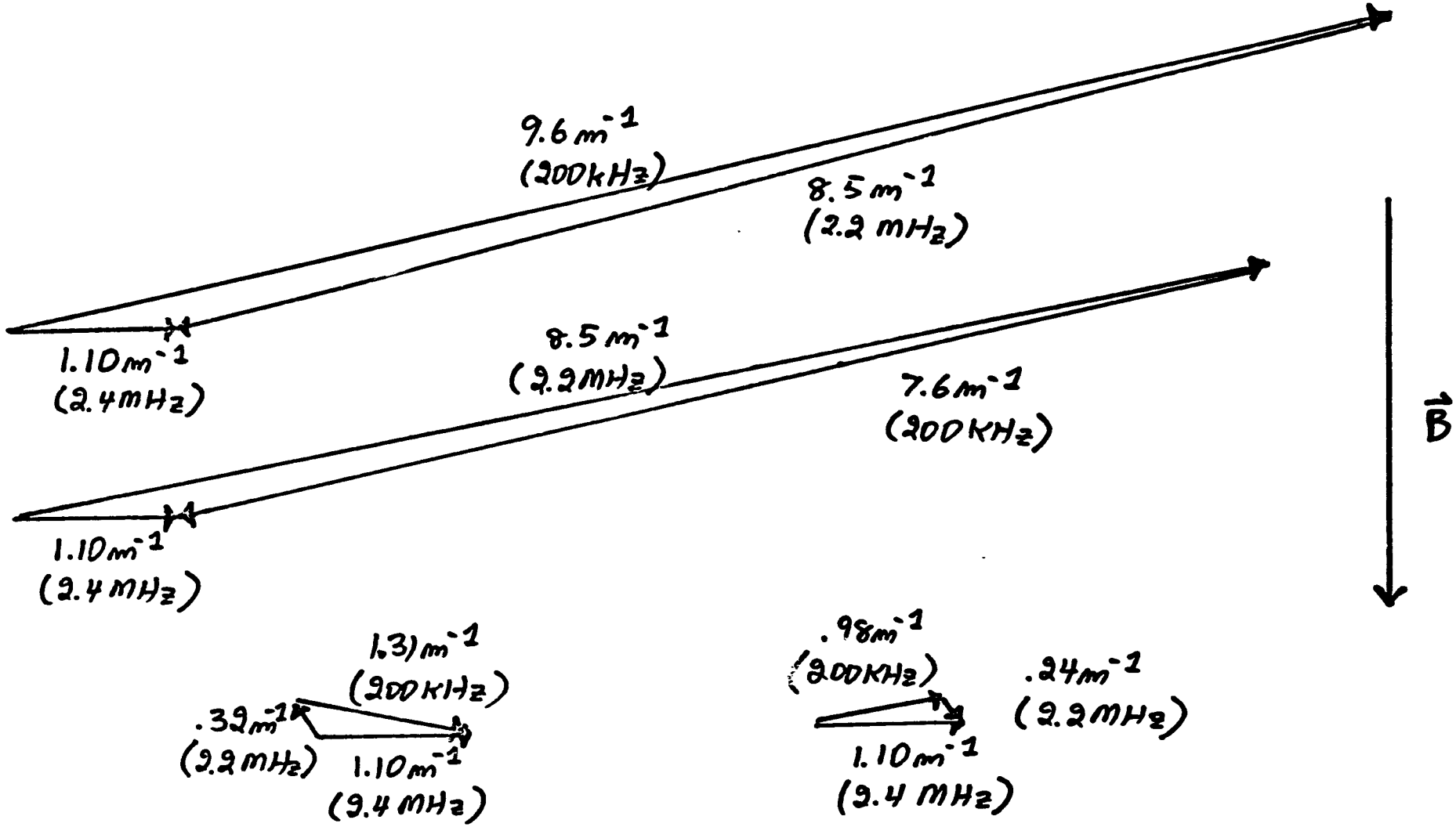

Figure V.15

WAVE VECTOR MATCHING SCHEMES